CANADIAN THESES ON MICROFICHE

I.S.B.N.

THESES CANADIENNES SUR MICROFICHE

National Library of Canada
Collections Development Branch

Canadian Theses on
Microfiche Service

Ottawa, Canada
K1A 0N4

Bibliothèque nationale du Canada
Direction du développement des collections

Service des thèses canadiennes
sur microfiche

NOTICE

The quality of this microfiche is heavily dependent upon the quality of the original thesis submitted for microfilming. Every effort has been made to ensure the highest quality of reproduction possible.

If pages are missing, contact the university which granted the degree.

Some pages may have indistinct print especially if the original pages were typed with a poor typewriter ribbon or if the university sent us a poor photocopy.

Previously copyrighted materials (journal articles, published tests, etc.) are not filmed.

Reproduction in full or in part of this film is governed by the Canadian Copyright Act, R.S.C. 1970, c. C-30. Please read the authorization forms which accompany this thesis.

AVIS

La qualité de cette microfiche dépend grandement de la qualité de la thèse soumise au microfilmage. Nous avons tout fait pour assurer une qualité supérieure de reproduction.

S'il manque des pages, veuillez communiquer avec l'université qui a conféré le grade.

La qualité d'impression de certaines pages peut laisser à désirer, surtout si les pages originales ont été dactylographiées à l'aide d'un ruban usé ou si l'université nous a fait parvenir une photocopie de mauvaise qualité.

Les documents qui font déjà l'objet d'un droit d'auteur (articles de revue, examens publiés, etc.) ne sont pas microfilmés.

La reproduction, même partielle, de ce microfilm est soumise à la Loi canadienne sur le droit d'auteur, SRC 1970, c. C-30. Veuillez prendre connaissance des formules d'autorisation qui accompagnent cette thèse.

THIS DISSERTATION
HAS BEEN MICROFILMED
EXACTLY AS RECEIVED

LA THÈSE A ÉTÉ
MICROFILMÉE TELLE QUE
NOUS L'AVONS REÇUE

NL-339 (r. 82/08)

Canada

National Library of Canada | Bibliothèque nationale du Canada

Canadian Theses Division | Division des thèses canadiennes

Ottawa, Canada
K1A 0N4

0-315-06144-8

54064

PERMISSION TO MICROFILM — AUTORISATION DE MICROFILMER

• Please print or type — Écrire en lettres moulées ou dactylographier

Full Name of Author — Nom complet de l'auteur

UNGSHANG, FELINO WOO

Date of Birth — Date de naissance	Country of Birth — Lieu de naissance
7 FEB. 1953	PHILIPPINES

Permanent Address — Résidence fixe

325 WOODSWORTH RD.
WILLOWDALE, ONT. M2L 2T7

Title of Thesis — Titre de la thèse

ELECTRICAL PROPERTIES OF NICKEL AND MANGANESE ALUMINATE

University — Université

UNIV. OF ALBERTA

Degree for which thesis was presented — Grade pour lequel cette thèse fut présentée

M.S. METALLURGICAL ENG.

Year this degree conferred — Année d'obtention de ce grade	Name of Supervisor — Nom du directeur de thèse
1981	DR. THOMAS H. ETSELL

Permission is hereby granted to the NATIONAL LIBRARY OF CANADA to microfilm this thesis and to lend or sell copies of the film.

The author reserves other publication rights, and neither the thesis nor extensive extracts from it may be printed or otherwise reproduced without the author's written permission.

L'autorisation est, par la présente, accordée à la BIBLIOTHÈQUE NATIONALE DU CANADA de microfilmer cette thèse et de prêter ou de vendre des exemplaires du film.

L'auteur se réserve les autres droits de publication; ni la thèse ni de longs extraits de celle-ci ne doivent être imprimés ou autrement reproduits sans l'autorisation écrite de l'auteur.

Date	Signature
28 AUG. 1981	

NL-91 (4/77)

THE UNIVERSITY OF ALBERTA

ELECTRICAL PROPERTIES OF NICKEL AND MANGANESE ALUMINATES

by

© FELINO WOO UNGSHANG

A THESIS

SUBMITTED TO THE FACULTY OF GRADUATE STUDIES AND RESEARCH

IN PARTIAL FULFILMENT OF THE REQUIREMENTS FOR THE DEGREE

OF MASTER OF SCIENCE

IN

METALLURGICAL ENGINEERING

DEPARTMENT OF MINERAL ENGINEERING

EDMONTON, ALBERTA

FALL 1981

THE UNIVERSITY OF ALBERTA

RELEASE FORM

NAME OF AUTHOR FELINO WOO UNGSHANG

TITLE OF THESIS ELECTRICAL PROPERTIES OF NICKEL AND MANGANESE ALUMINATES

DEGREE FOR WHICH THESIS WAS PRESENTED MASTER OF SCIENCE

YEAR THIS DEGREE GRANTED FALL 1981

Permission is hereby granted to THE UNIVERSITY OF ALBERTA LIBRARY to reproduce single copies of this thesis and to lend or sell such copies for private, scholarly or scientific research purposes only.

The author reserves other publication rights, and neither the thesis nor extensive extracts from it may be printed or otherwise reproduced without the author's written permission.

(SIGNED) .....

PERMANENT ADDRESS:

325 Woodsworth Road

Willowdale, Ontario

M2L 2T7

DATED 28 August 1981

THE UNIVERSITY OF ALBERTA

FACULTY OF GRADUATE STUDIES AND RESEARCH

The undersigned certify that they have read, and recommend to the Faculty of Graduate Studies and Research, for acceptance, a thesis entitled ELECTRICAL PROPERTIES OF NICKEL AND MANGANESE ALUMINATES submitted by FELINO WOO UNGSHANG in partial fulfilment of the requirements for the degree of MASTER OF SCIENCE in METALLURGICAL ENGINEERING.

T. H. Etsell

.....

Supervisor

Samuel G. Bradford

.....

Date: August 24, 1981

Abstract

Electrical conductivity in polycrystalline $NiAl_2O_4$ and $MnAl_2O_4$ was studied at temperatures of 800° to 1400°C and oxygen partial pressures of 1 to 10^{-34} atm O_2. Both aluminates were prepared from equimolar mixtures of component oxides and sintered at 1400°C for 48 hr and at 1700°C for 5 hr. The $NiAl_2O_4$ was sintered in air; $MnAl_2O_4$ in purified argon.

The conductivity in both aluminates was investigated using the two-probe ac conductivity method with the oxygen partial pressures achieved with preanalyzed Ar-O_2 and CO-CO_2 mixtures and reversible metal-metal oxide electrodes. $NiAl_2O_4$ exhibits conductivity independent of oxygen partial pressure. The conductivity of $NiAl_2O_4$ increases from 1.5 x 10^{-4} at 800°C to 1.3 x 10^{-3} ohm^{-1}-cm^{-1} at 1400°C. The activation energy for ionic conduction in $NiAl_2O_4$ is 41.2 kcal/mole.

$MnAl_2O_4$ exhibits p- and n-type conductivities which are proportional to $P(O_2)^{1/4}$ and $P(O_2)^{-1/4}$, respectively. Ionic conduction at intermediate oxygen partial pressures is evident. The ionic conductivity of $MnAl_2O_4$ increases from 1.0 x 10^{-3} at 800°C to 1.8 x 10^{-3} ohm^{-1}-cm^{-1} at 1400°C. The activation energies for p-type, ionic and n-type conduction are 12.6, 31.1, and 52.4 kcal/mole, respectively.

The ionic transport number t_i was determined by the dc polarization technique. For $NiAl_2O_4$, t_i decreases from 0.97 at 800°C (10^{-4} atm O_2) to 0.63 at 1400°C (10^{-4} atm O_2); for

$MnAl_2O_4$, t_i decreases from 0.99 at 800°C (10^{-19} atm O_2) to 0.89 at 1400°C (10^{-12} atm O_2).

The relative transport numbers of the cations, Ni^{2+} and Mn^{2+}, were measured with the emf method. For $NiAl_2O_4$, the average transport number $3t_{Ni}^{2+}$ is greater than t_{Al}^{3+} at temperatures of 800° to 1400°C; for $MnAl_2O_4$, $3t_{Mn}^{2+} < t_{Al}^{3+}$ at 800° to 1050°C and $3t_{Mn}^{2+} > t_{Al}^{3+}$ at 1050° to 1400°C.

Acknowledgements

I would like to express my sincere thanks to Dr. T. H. Etsell for his guidance and encouragement throughout the course of this research.

Special thanks to the technical staff of the Department of Mineral Engineering, in particular, Messrs. B. Snider, B. Konzuk, T. Forman, B. Smith and Ms. C. Barker for their assistance.

Special mention to Dr. A. Block-Bolten for his advice and suggestions, and to my fellow graduate students, G. Cameron and P. Griffin, for their help and constructive criticisms in the duration of this work.

Table of Contents

Chapter		Page
I.	Introduction	1
II.	Literature Survey	3
	A. Cation Distribution In Spinels	3
	B. Ionic Transport In Spinels (Aluminates)	14
	C. Thermodynamics of Spinels (Aluminates)	22
	D. Electrical Conductivity of Spinels	27
III.	Theory	34
	A. Crystal Structure of Spinel	34
	B. Electrical Conductivity of Solid Electrolytes	34
	C. DC Polarization Measurements	37
	D. Transport Numbers By Emf Measurements	39
IV.	Experimental	42
	A. Material Preparation	42
	Chemicals	44
	Gas Mixtures	44
	B. Two-Probe AC Conductivity Measurements	46
	C. DC Polarization Measurements	51
	D. Emf Measurements	53
V.	Results and Discussion	56
	A. Nickel Aluminate	56
	Conductivity Measurements	58
	DC Polarization Measurements	67
	Emf Measurements	69
	B. Manganese Aluminate	71
	Conductivity Measurements	72

DC Polarization Measurements 78

Emf Measurements 79

Conclusions 81

Figures 82

Tables 147

Plate 166

Bibliography 168

List of Figures

Figure		Page
1.	Spinel Structure	83
2.	Projection of occupied spinel sites on the (001) plane.	84
3.	Schematic representation of partial ionic and electronic conductivities.	85
4.	Schematic representation of the electrolytic region where $t_{ion} > 0.99$.	86
5.	Partial conductivities as a function of oxygen partial pressure.	87
6.	$NiO-Al_2O_3$ system.	88
7.	$MnO-Al_2O_3$ system.	89
8.	Circuit used to measure the two-probe ac electrical conductivity.	90
9.	Conductivity isotherms for $NiAl_2O_4$ (Sample B4).	91
10.	P-type conductivity isotherms for $NiAl_2O_4$ (Sample B4).	92
11.	Determination of the ionic conductivity of $NiAl_2O_4$ (Sample B4).	93
12.	Conductivity isotherms for $NiAl_2O_4$ (Sample B2).	94
13.	Conductivity isotherms for $NiAl_2O_4$ (Sample B6).	95
14.	Conductivity isotherms for $NiAl_2O_4$ (Reversible Electrodes).	96
15.	Arrhenius plot of the ionic conductivity of $NiAl_2O_4$ (Sample B4).	97
16.	Arrhenius plot of the ionic conductivity of $NiAl_2O_4$ (Sample B2).	98
17.	Arrhenius plot of the ionic conductivity of $NiAl_2O_4$ (Sample B6).	99
18.	Arrhenius plot of the ionic conductivity of $NiAl_2O_4$ (Reversible Electrodes).	100

Figure Page

19. Current - applied potential curves for $NiAl_2O_4$ at 800°C. 101

20. Current - applied potential curves for $NiAl_2O_4$ at 900°C. 102

21. Current - applied potential curves for $NiAl_2O_4$ at 1000°C. 103

22. Current - applied potential curves for $NiAl_2O_4$ at 1100°C. 104

23. Current - applied potential curves for $NiAl_2O_4$ at 1200°C. 105

24. Current - applied potential curves for $NiAl_2O_4$ at 1300°C. 106

25. Current - applied potential curves for $NiAl_2O_4$ at 1400°C. 107

26. Logarithmic current - potential plots for $NiAl_2O_4$ ($Ar-O_2$: 1.3 ppm O_2). 108

27. Logarithmic current - potential plots for $NiAl_2O_4$ ($CO-CO_2$: 1.99% CO). 109

28. Ionic transport number - temperature plots for $NiAl_2O_4$ (DC Polarization Measurements). 110

29. Arrhenius plot of the p-type conductivity of $NiAl_2O_4$ ($Ar-O_2$: 1.3 ppm O_2, DC Polarization Measurements). 111

30. Arrhenius plot of the p-type conductivity of $NiAl_2O_4$ ($CO-CO_2$: 1.99% CO, DC Polarization Measurements). 112

31. Emf - temperature plots for $NiAl_2O_4$ (Emf Measurements). 113

32. Conductivity isotherms for $MnAl_2O_4$ (Sample D10). 114

33. P-type conductivity isotherms for $MnAl_2O_4$ (Sample D10). 115

34. N-type conductivity isotherms for $MnAl_2O_4$ (Sample D10). 116

Figure Page

35. Determination of the ionic conductivity of $MnAl_2O_4$ (Sample D10). 117

36. Conductivity isotherms for $MnAl_2O_4$ (Sample D2). 118

37. P-type conductivity isotherms for $MnAl_2O_4$ (Sample D2). 119

38. N-type conductivity isotherms for $MnAl_2O_4$ (Sample D2). 120

39. Determination of the ionic conductivity of $MnAl_2O_4$ (Sample D2). 121

40. Conductivity isotherms for $MnAl_2O_4$ (Reversible Electrodes). 122

41. P-type conductivity isotherms for $MnAl_2O_4$ (Reversible Electrodes). 123

42. P-type conductivity isotherms for $MnAl_2O_4$ (Reversible Electrodes). 124

43. N-type conductivity isotherms for $MnAl_2O_4$ (Reversible Electrodes). 125

44. Determination of the ionic conductivity of $MnAl_2O_4$ at 800°-900°C (Reversible Electrodes). 126

45. Determination of the ionic conductivity of $MnAl_2O_4$ at 1000°-1400°C (Reversible Electrodes). 127

46. Arrhenius plot of the ionic conductivity of $MnAl_2O_4$ (Sample D10). 128

47. Arrhenius plot of the ionic conductivity of $MnAl_2O_4$ (Sample D2). 129

48. Arrhenius plot of the ionic conductivity of $MnAl_2O_4$ (Reversible Electrodes). 130

49. Arrhenius plots of the p-type conductivity of $MnAl_2O_4$ (Sample D10). 131

50. Arrhenius plots of the p-type conductivity of $MnAl_2O_4$ (Sample D2). 132

Figure Page

51. Arrhenius plots of the p-type conductivity of $MnAl_2O_4$ (Reversible Electrodes). 133

52. Arrhenius plots of the n-type conductivity of $MnAl_2O_4$ (Sample D2). 134

53. Arrhenius plots of the n-type conductivity of $MnAl_2O_4$ (Reversible Electrodes). 135

54. Current - applied potential curves for $MnAl_2O_4$ at 800°C. 136

55. Current - applied potential curves for $MnAl_2O_4$ at 900°C. 137

56. Current - applied potential curves for $MnAl_2O_4$ at 1000°C. 138

57. Current - applied potential curves for $MnAl_2O_4$ at 1100°C. 139

58. Current - applied potential curves for $MnAl_2O_4$ at 1200°C. 140

59. Logarithmic current - potential plots for $MnAl_2O_4$ ($CO-CO_2$: 54.6% CO). 141

60. Logarithmic current - potential plots for $MnAl_2O_4$ ($CO-CO_2$: 2.02% CO_2). 142

61. Ionic transport number - temperature plots for $MnAl_2O_4$ (DC Polarization Measurements). 143

62. Arrhenius plot of the p-type conductivity of $MnAl_2O_4$ ($CO-CO_2$: 54.6% CO, DC Polarization Measurements). 144

63. Arrhenius plot of the p-type conductivity of $MnAl_2O_4$ ($CO-CO_2$: 2.02% CO_2, DC Polarization Measurements). 145

64. Emf - temperature plots for $MnAl_2O_4$ (Emf Measurements). 146

List of Tables

Table		Page
1.	Self-diffusion in Oxide Systems	148
2.	Equilibrium Oxygen Partial Pressures of Reversible Electrodes at 1000°C [158]	149
3.	Thermodynamic Stability Limit of $NiAl_2O_4$	150
4.	Thermodynamic Stability Limits of $MnAl_2O_4$	151
5.	Conductivity Data For $NiAl_2O_4$ (Sample B4)	152
6.	Conductivity Data For $NiAl_2O_4$ (Sample B6)	154
7.	Conductivity Data For $NiAl_2O_4$ (Reversible Electrodes)	156
8.	P-type Conductivity Data For $NiAl_2O_4$ (DC Polarization Measurements)	158
9.	Emf - Temperature Data For $NiAl_2O_4$ (Emf Measurements, $P(O_2)$=0.21 atm)	159
10.	Conductivity Data For $MnAl_2O_4$ (Sample D10)	160
11.	Conductivity Data For $MnAl_2O_4$ (Sample D2)	161
12.	Conductivity Data For $MnAl_2O_4$ (Reversible Electrodes)	162
13.	P-type Conductivity Data For $MnAl_2O_4$ (DC Polarization Measurements)	164
14.	Emf - Temperature Data For $MnAl_2O_4$ (Emf Measurements)	165

List of Plates

Plate		Page
1.	Two-probe conductivity cell holder	167

I. Introduction

Although ionic conduction was recognized to exist in solid compounds such ZrO_2-Y_2O_3 at the turn of the century [1-3], it was the publications in 1957 by Kiukkola and Wagner [4,5] that led to the upsurge in the study of ionic conduction in the solid state. The solid electrolyte studied by Kiukkola and Wagner was stabilized ZrO_2, but other compounds such as silver halides[6,7], thoria [8],yttria [9],ceria [10],rutile [11], alumina [12], and beta-alumina [13] were later established as solid electrolytes. Since then, these solid electrolytes have been used extensively in high temperature investigations.

Recently, spinels have been considered for use in high temperature studies, especially in the power generation field. Iron magnesium spinels [14] and spinel solid solutions of hercynite ($FeAl_2O_4$) and magnetite [15] have been considered for use as electrical conductors and magnesium aluminate spinel ($MgAl_2O_4$) [16] as refractory in open-cycle, coal-fired magnetohydrodynamic electric generators. More basic physical property data of spinels are required before their use in high temperature studies can be undertaken.

The spinels are a class of binary oxides whose structure is related to that of the mineral spinel, $MgAl_2O_4$. The general formula of a spinel is AB_2O_4.

The spinel structure is cubic with a large unit cell containing 8A, 16B and 32 oxygen atoms or ions. The

positions of the oxygen atoms are more or less fixed but the arrangement of the cations varies considerably within certain limits.

In most oxide structures, the oxygen ions are appreciably larger than the cations and the spinel structure can be approximated by a cubic close packing of O^{2-} ions in which the A^{2+} and B^{3+} ions occupy certain interstices. Each unit cell contains $8(AB_2O_4)$ subcells, and therefore, 32 O^{2-} ions. This close packing, as shown in Fig. 1, contains 64 interstices surrounded by 4 O^{2-} ions (coordination number of 4, tetrahedral) and 32 interstices surrounded by 6 O^{2-} ions (coordination number of 6, octahedral). In the spinel structure, 8 of the tetrahedral interstices or sites and 16 of the octahedral interstices or sites are occupied by cations.

In all spinel-like oxides, the arrangement of the O^{2-} ions is represented by the parameter u. For u=0.375, the arrangement of the O^{2-} ions equals exactly a cubic close packing. In actual spinel lattices, u is often larger; this implies larger A or tetrahedral sites and smaller B or octahedral sites.

Two types of spinel occur. In the normal spinel, the A^{2+} ions are on the tetrahedral sites and the B^{3+} ions are on the octahedral sites. In the inverse or inverted spinel, the A^{2+} ions and half the B^{3+} ions are on the octahedral sites; the other half of the B^{3+} ions are on the tetrahedral sites as represented by the formula $B(AB)O_4$.

II. Literature Survey

This literature survey will cover briefly some of the physical property data on spinels, particulary the aluminates. Topics will include cation distribution , ionic transport, thermodynamics and electrical conductivity in spinels.

A. Cation Distribution In Spinels

The crystal structure of spinels was analyzed by Bragg [17] and independently by Nishikawa [18] in 1915. In both cases, the work was based on the study of spinel ($MgAl_2O_4$) and magnetite (Fe_3O_4). At that time a large number of compounds of the general formula AB_2O_4, both natural and synthetic products, were examined and accepted as having the spinel structure. It was also assumed at that time that in the spinels AB_2O_4, the A atoms or ions occupied the tetrahedral sites and the B atoms or ions were in the octahedral sites - the normal spinel arrangement.

However, the x-ray diffraction intensities of a number of the compounds, $MgFe_2O_4$ and $MgGa_2O_4$, could not be reconciled with the accepted atomic arrangement of the spinel. In order to account correctly for the observed intensities of $MgFe_2O_4$ and $MgGa_2O_4$, Barth and Posnjak [19] proposed a second spinel arrangement - the inverse spinel - in which the tetrahedral sites are occupied by half of the B ions, the octahedral sites by the A ions, and the other half of the B ions are distributed at these lattice sites. Barth

and Posnjak [19] examined the spinel arrangement of ferrites, gallates, indiates, titanates and aluminates by comparing the observed intensities of x-ray reflections with those calculated for normal and inverse spinel arrangement based on the ideal oxygen ion arrangement parameter u of 0.375. In this technique, it is possible to decide between the normal and inverse arrangements when the scattering powers for x-rays of the cations are sufficiently different; when the scattering powers of the cations are too small or weak, the results are suspect. Using this method, Barth and Posnjak [19] concluded that all aluminates (Mg, Mn, Ni, Zn and Co) and chromites are normal, all ferrites except Zn and Cd ferrites are inverse and all divalent-tetravalent (2-4) spinels such as the titanates and stannates are inverse.

Verwey and Heilmann [20] modified the x-ray diffraction technique used by Barth and Posnjak [19] to determine the cation arrangement in spinels. The intensities of a great number of diffraction lines were measured and the observed values were compared with the calculated reflection intensities for different spinel arrangements and for different values of u. To enhance the scattering power of the constituent metal ions, selective wavelengths of x-ray radiation were adopted. From this study, Verwey and Heilmann [20] formulated a set of rules for predicting whether a spinel has a normal or inverse arrangement. These rules state that for a divalent-trivalent (2-3) spinel, the normal structure or arrangement is more stable with the following

exception: if the trivalent ion is Fe, Ga, or In, then the inverse structure is more stable; however, Zn and Cd spinels are normal, regardless of the trivalent ion. In addition, all aluminates have the normal structure.

It had never been clearly established whether the aluminates of Mn, Co, Ni, Zn and Fe are normal or inverted; the evidence on which Barth and Posnjak [19], and Verwey and Heilmann [20] used to conclude that the aluminates are normal was rather weak. From the x-ray diffraction analysis of simple and complex spinels (aluminates, germanates, titanates and ferrites), Romeijn [21] observed that the intensity of the 220 reflection - I(220) - is only determined by the ions at the tetrahedral sites and this reflection is a simple indicator for the change in cation distribution in the spinel. Analyzing the I(220) reflections of the aluminates, Romeijn [21] concluded that the aluminates of Mn, Fe, Co and Zn are normal but Ni aluminate is partly inverted. In Ni aluminate, the fraction of Ni^{2+} ions at tetrahedral sites was observed to be 0.24, giving an approximate formula of $Ni_{0.24}Al_{0.76}(Al_{1.24}Ni_{0.76})O_4$. The degree of inversion of about 0.76 in Ni aluminate indicates a strong preference of Ni^{2+} ions for the octahedral sites.

Further improvement in the determination of cation distribution in spinels by the x-ray diffraction technique was initially made by Bertaut [22] who reported that the x-ray intensity ratios I(400)/I(220) and I(400)/I(224) are very sensitive to the distribution of the cations and

relatively insensitive to the oxygen parameter u. Other intensity ratios I(220)/I(311) [23], I(400)/I(220) [24,25], I(400)/I(422) [22,24] and I(400)/I(224) [26] were proposed for use in the study of cation distribution in spinels.

Using x-ray diffraction (I(400)/I(200) and I(400)/I(224) ratios) and magnetic susceptibility techniques, Greenwald et al. [24] reported that Co and Mn aluminates have a normal cation arrangement while Ni aluminate is partly inverted. The degree of inversion for slowly cooled and quenched (from 1400°C) samples was 0.85 and 0.80, respectively for Ni aluminate; 0.19 and 0.31 for Co aluminate; and 0.34 and 0.29 for Mn aluminate. These authors suggested that the Ni^{2+} ions have strong preference for octahedral sites, Co^{2+} ions for tetrahedral sites, and Mn^{2+} ions no site preference. In addition, these authors pointed out that annealing $MnAl_2O_4$ in air resulted in the formation of Mn_3O_4 and a compound which is a tetragonal distortion in spinel.

Magnetic susceptibility measurements conducted by Richardson and Milligan [27] on a series of $NiO-Al_2O_3$ samples (0-100 mol% NiO) heated at 700° and 1000°C revealed that the degree of inversion of $NiAl_2O_4$ was 0.85 at 700°C and 0.95 at 1000°C. For the composition range of 60 to 100 mol% NiO, the degree of inversion was calculated to be close to 1.00 for samples annealed at 700° and 1000°C, indicating that Ni^{2+} ions occupy octahedral sites in this range.

Combining magnetic susceptibility and x-ray diffraction measurements on the $CoO-Al_2O_3$ system prepared from Co_3O_4 and Al_2O_3, Richardson and Vernon [28] reported the presence of Co^{3+} ions in the $CoO-Al_2O_3$ samples containing 40 to 80 wt% Co. They suggested that Co^{2+} and Co^{3+} ions occupy the tetrahedral and octahedral sites, respectively. Following the reasoning of Sinha et al. [29], who proposed the formula $Al(V_{0.33}Al_{1.67})O_4$ (V stands for vacancies) as the best structure of γAl_2O_3, Richardson and Vernon [28] indicated that, as the $CoO-Al_2O_3$ series approach low Co concentrations (<45 wt% Co), the Co exists only as Co^{2+} ions on the tetrahedral sites and lattice vacancies appear on the octahedral sites only - the latter conclusion being subtantiated by their x-ray measurements.

Edwards [30], using the x-ray diffraction method, cited that the mixed crystal spinel series $MnCr_{2-t}Al_tO_4$ ($0 \leq t \leq 2$) has a normal spinel arrangement with the tetrahedral sites occupied by Mn^{2+} ions and about 5% of the Al^{3+} ions.

Paramagnetic resonance spectra analysis of Cr^{3+} ions in $MgAl_2O_4$ and Mn^{2+} ions in $ZnAl_2O_4$ by Stahl-Brada and Low [31] revealed that Cr^{3+} ions reside on the octahedral sites while Mn^{2+} ions occupy the tetrahedral sites of the spinel. In the case of $MnAl_2O_4$, the authors suggested the possibilities that a fraction of the Mn^{2+} ions occupies the octahedral sites and a fraction of the manganese ions may exist as Mn^{4+} or Mn^{3+} in the spinel.

Nuclear magnetic resonance spectra of Al^{3+} ions in natural and synthetic crystals of $MgAl_2O_4$ (annealed at 800° and 900°C) [32] revealed that about 1% of the Al^{3+} ions occupy the tetrahedral sites of the natural crystal while Mg^{2+} and Al^{3+} ions are randomly distributed among the tetrahedral and octahedral sites of the synthetic crystal of $MgAl_2O_4$.

Schmalzried [25,33], using the x-ray diffraction technique, studied the temperature dependence of cation distribution in the spinels $NiAl_2O_4$, $CoAl_2O_4$ and $MgGa_2O_4$ at temperatures of 800° to 1500°C. He reported a decrease in the degree of inversion from 0.815 at 800°C to 0.74 at 1500°C for $NiAl_2O_4$; an increase from 0.055 at 850°C to 0.15 at 1400°C for $CoAl_2O_4$; and a decrease from 0.90 at 900°C to 0.83 at 1400°C for $MgGa_2O_4$.

Correlating four properties (i.e., unit cell dimension, x-ray intensities, reflectance spectra in the visible region, and infrared absorption spectra from 11 to 25 μm) of spinels prepared and equilibrated at temperatures of 400° to 800°C and pressures of 1 to 100,000 atm, Datta and Roy [26,34,35] showed that in the majority of spinels, including the common ones (e.g., $MgAl_2O_4$, $NiAl_2O_4$ and others), the cation distribution is a function of the temperature and pressure of formation. Using the x-ray diffraction technique, Datta and Roy [26] reported that several titanates (Zn_2TiO_4, Mg_2TiO_4), chromites ($MgCr_2O_4$, $NiCr_2O_4$, $ZnCr_2O_4$) and $ZnAl_2O_4$ do not have any appreciable temperature

dependence of cation distribution between 600° and 1300°C (at constant pressure of 351 kg/cm²). However, in the case of $NiAl_2O_4$ and Ni_2GeO_4, an increased tendency of Ni^{2+} ions to move from the octahedral sites to the tetrahedral sites with increase in temperature was observed. $NiAl_2O_4$ was observed to be completely inverted at 600°C with the cation arrangement $(Al)(NiAl)O_4$; at 1550°C, $NiAl_2O_4$ was 75% inverted with the arrangement $(Ni_{0.25}Al_{0.75})(Ni_{0.75}Al_{1.25})O_4$.

Using the x-ray diffraction method, Cooley and Reed [36] determined the cation distribution in $NiAl_2O_4$, $CuAl_2O_4$ and $ZnAl_2O_4$. The oxygen parameter u and the fraction of divalent cations on tetrahedral sites X were calculated by the least-residual technique using the measured x-ray intensities of two reflections which are independent of X and the ideal value of u (0.375). The temperature of the sample during irradiation was taken into account in the computation of X and u.

Cooley and Reed [36] reported that in $NiAl_2O_4$, X increases from 0.07 at 595°C to 0.26 at 1391°C; for for $CuAl_2O_4$, X decreases from 0.68 at 613°C to 0.64 at 1195°C; and for $ZnAl_2O_4$, X decreases from 0.96 at 905°C to 0.94 at 1197°C. For $NiAl_2O_4$, Schmalzried's [24,32] high values of X were attributed to nonequilibrium samples. On the other hand, results of Datta and Roy [26] were lower by approximately 0.06 at all temperatures; these values were calculated using the single ratio I(220)/I(440) and the

ideal oxygen parameter u (0.250). The work of Grimes et al. [37] suggests that the use of the I(220)/I(440) ratio will lead to negative errors in X.

Using a modified x-ray diffraction technique, Furuhashi et al. [38] determined the cation distribution of $NiAl_2O_4$, $CoAl_2O_4$ and $GeCo_2O_4$. The temperature of the sample was taken into consideration in the computation of the degree of inversion and oxygen parameter u by the least-residual method. They reported that the degree of inversion was 0.17 at 1000° and 1400°C and 0.18 at 1200°C for $CoAl_2O_4$; 0.00 at 1000° to 1400°C for $GeCo_2O_4$; and 0.84 at 1400°C for $NiAl_2O_4$.

A spectrophotometrical investigation of the system Ni in $Mg_{1-x}Al_2O_4$ ($0 \leq x \leq 1$) by Schmitz-DuMont et al. [39] indicated that Ni^{2+} ions occupy octahedral as well as tetrahedral sites even at low concentration of Ni_x , i.e., x=0.01.

Stone [40], using the IR spectroscopic method, measured the cation distribution in $CuAl_2O_4$ and $NiAl_2O_4$. From the absorption spectra of the spinels annealed at 970°C, Stone [40] calculated the degree of inversion to be 0.75 for $NiAl_2O_4$ and 0.40 for $CuAl_2O_4$.

By using the neutron diffraction technique which minimizes errors due to scattering (a common limitation of the x-ray diffraction method), Roth [41] determined the degree of inversion in $MnAl_2O_4$, $FeAl_2O_4$ and $CoAl_2O_4$ samples slowly cooled from 1200°C. The degree of inversion obtained was 0.042 for $MnAl_2O_4$; 0.077 for $FeAl_2O_4$; and 0.025 for

$CoAl_2O_4$. These results reveal that Mn, Fe and Co aluminates have normal spinel arrangements.

Cationic distribution measurements on $CoAl_2O_4$ by Richardson [23] by the x-ray diffraction method show that $CoAl_2O_4$ has a normal spinel arrangement with a degree of inversion of 0.07 at room temperature.

The normal spinel structure of $CoAl_2O_4$ was further confirmed by Cossee and van Arkel [42] who used magnetic susceptibility and absorption spectra measurements on $CoAl_2O_4$ and on the mixed crystals, $CoAl_2O_4$-$MgAl_2O_4$ and $CoAl_2O_4$-$ZnAl_2O_4$, annealed at 300° to 1200°K. Their results indicate that Co^{2+} ions reside in the tetrahedral sites in the temperature range studied.

Although Greenwald et al. [24] suggested the presence of Co^{3+} ions in $CoAl_2O_4$, nuclear magnetic resonance measurements made by Miyatani et al. [43-44] and Kamimura [45] on $CoAl_2O_4$ indicated that all cobalt ions are in the divalent state and occupy only the tetrahedral sites.

From the Mossbauer spectra of Fe in $FeNiAlO_4$, $FeNiCrO_4$ and $FeAl_2O_4$, Mizoguchi and Tanaka [46] observed that in $FeAl_2O_4$, all the octahedral sites are occupied only by trivalent Al^{3+} ions. However, thermal conductivity, optical absorption coefficient and magnetic susceptibility measurements on $FeAl_2O_4$ and $FeAl_2O_4$-$MgAl_2O_4$ by Slack [47] indicate the presence of a low concentration of Fe^{3+} on the tetrahedral sites and Fe^{2+} on the octahedral sites at temperatures of 1000° to 1500°C.

Early attempts to provide a theoretical explanation for the cation distribution in spinels was made by De Boer et al. [48,49] on the basis of the lattice energy resulting from the consideration of the Madelung constant, oxygen parameter u and the size of the unit cell. De Boer [48,49] suggested that for a fixed value of the lattice constant, a normal spinel structure is stable for $u > 0.379$ in the case of divalent-trivalent (2-3) spinels, and $u < 0.385$ for divalent-tetravalent (2-4) spinels; otherwise, inverse spinels are stable.

Miller [50] introduced the concept of octahedral site preference energy in spinels which includes the Madelung potential and short-range order. A set of site preference energies was formulated and used to predict the probable cation distribution in spinels.

A theoretical explanation of the cation distribution was proposed by McClure [51] and by Dunitz and Orgel [52] using crystal (ligand) field theory and symmetry considerations. From the optical (visible and infrared) absorption data with the aid of crystal field theory, thermodynamic stabilization energies for a transition metal ion on octahedral and tetrahedral sites in the spinel lattice were calculated. The difference between the octahedral and tetrahedral stabilization energies - the site preference energy - was used to predict the cation distribution. Accuracy of the prediction, in particular for the aluminates was limited by the lack of a more exact

estimate of the site preference energy for Al^{3+} ion.

Another approach was adopted by Navrotsky and Kleppa [53] to predict the cation distribution in spinels. The cation distribution in spinels was treated as a simple chemical equilibrium and molar interchange enthalpies, ΔH, of ions on tetrahedral sites with ions on the octahedral sites were calculated from cation distribution data at a single temperature for each spinel. From the interchange enthalpies, empirical site preference energies for a series of divalent and trivalent ions in the spinel structure were obtained. Negative values of ΔH were obtained for spinels with distribution between random and inverse while positive values were obtained for distribution between normal and random. From the set of site preference energies obtained, Navrotsky and Kleppa [53] concluded :

1. ions with large tetrahedral site preference: Zn^{2+}, Cd^{2+} and In^{3+};
2. ions with small to zero tetrahedral site preference: Fe^{3+}, Ga^{3+}, Co^{2+}, Mn^{2+}, Mg^{2+}, Fe^{2+}; and
3. ions with large octahedral site preference: Cu^{2+}, Ni^{2+}, Al^{3+}, Mn^{3+} and Cr^{3+}.

On the basis of the site preference energies, it is recognized that the only divalent ions which are able to compete with Al^{3+} for octahedral sites are Cu^{2+} and Ni^{2+}. $CuAl_2O_4$ and $NiAl_2O_4$ are the only known inverse aluminates.

Comprehensive reviews on crystal structure, cation distribution and magnetic properties of spinels have been

written by Gorter [54] and Blasse [55].

B. Ionic Transport In Spinels (Aluminates)

Extensive investigation on self-diffusion of cations in oxides, silicates and spinels and solid-state reactions with the use of radioactive tracers were made by Lindner et al. [56-64]. In the formation of silicates and spinels by solid-state reactions, Lindner and Akerstrom [62] indicated that the concept of counter-diffusion of cations as proposed by Wagner [65] seems to be the probable mechanism. The self-diffusion results are summarized in Table 1. Other self-diffusion results discussed below are given in the form of $D=D_o\exp(-Q/RT)$ with Q in cal/mole.

Belokurova and Ignatov [66] measured the diffusion of ^{59}Fe and ^{51}Cr in sintered samples of $NiCr_2O_4$ and $NiAl_2O_4$ heated at temperatures of 900° to 1200°C. Radioactive iron and chromium were deposited on the samples by evaporation and condensation of metals in vacuum; diffusion was investigated by serial sectioning. For the diffusion of Cr in $NiCr_2O_4$ and $NiAl_2O_4$, the results are $D(Cr)=(2.03 \times 10^{-5})\exp(-44{,}000/RT)$ and $D(Cr)=(1.17 \times 10^{-3})\exp(-50{,}000/RT)$ cm^2/sec, respectively. For the diffusion of Fe in $NiCr_2O_4$, $D(Fe)=(1.35 \times 10^{-3})\exp(-61{,}000/RT)$ cm^2/sec. Belokurova and Ignatov [66] pointed out that the relatively large value of the activation energy for iron diffusion in $NiCr_2O_4$ in comparison to the activation energy for chromium diffusion could be due to the difference in the ionic radii of Fe^{2+}

and Cr^{3+}.

The diffusion of ^{60}Co and ^{51}Cr in sintered samples of $CoCr_2O_4$ was measured by Sun [67] in the temperature region of 1400° to 1600°C where bulk diffusion predominates. The diffusion results for Co and Cr are $D=(10^{-3})\exp(-51{,}000/RT)$ and $D=(2)\exp(-70{,}000/RT)$ cm^2/sec, respectively. Sun [67] proposed that the diffusion of cations involves the jump of a cation from an occupied site (tetrahedral or octahedral site) to several unoccupied sites, the path being influenced by the cation's electronic configuration and ionic radius. For the diffusion of Cr, the proposed path involves a jump from an octahedral site to a neighboring unfilled tetrahedral site and then to an unfilled octahedral site; for the Co^{2+} ion, the path involves a jump from a tetrahedral site to an empty octahedral site and then to an empty tetrahedral site.

Morkel and Schmalzried [68] investigated the diffusion of Co^{2+} and Cr^{3+} ions in the normal spinels $CoAl_2O_4$, $CoCr_2O_4$ and $NiCr_2O_4$ and in the inverse spinel Co_2TiO_4. The results are: for Co_2TiO_4, $D(Co)=(5 \times 10^4)\exp(-9500/RT)$; for $CoAl_2O_4$, $D(Co)=(8)\exp(-85{,}000/RT)$; for $CoCr_2O_4$, $D(Co)=(80)\exp(-90{,}000/RT)$ and $D(Cr)=(300)\exp(-85{,}000/RT)$; and for $NiCr_2O_4$, $D(Cr)=(2)\exp(-100{,}000/RT)$ cm^2/sec. From the ratios of self-diffusion coefficients, the disorder (defect) structure in the spinel was estimated. For $CoAl_2O_4$, which exists with a deficiency of cations, Co^{2+} vacancies and Al^{3+} ions on interstitial sites or on regular sites of Co^{2+} ions

are the most probable major defects; for $CoCr_2O_4$, excess Co^{2+} ions on interstitial sites and Cr^{3+} vacancies; and for $NiCr_2O_4$, Ni^{2+} ions on interstitial sites and Cr^{3+} vacancies [69].

The diffusion of ^{59}Fe in the iron-aluminate spinel system (Fe_3O_4-$FeAl_2O_4$) was studied by Halloran and Bowen [70] and the results were analyzed in terms of a defect model, assuming that the predominant defects are cation vacancies and interstitials. Halloran and Bowen [70] pointed out that iron diffusion in Fe_3O_4 at 1380°C occurs by an interstitial mechanism at $P < 10^{-4}$ atm O_2 and by a vacancy mechanism at $P > 10^{-4}$ atm O_2. These authors proposed that iron diffuses in $Fe(Fe_{1.8},Al_{0.4})O_4$ at 1380°C by an interstitial mechanism at $P(O_2) < 10^{-5}$ atm and by a vacancy mechanism at $P(O_2) > 10^{-5}$ atm. Iron diffusion in single crystal and polycrystalline (alumina-rich) $FeAl_2O_4$ is by an interstitial and vacancy mechanism, respectively, at 1400°C.

The effects of cation vacancies on the diffusion of Ni^{2+} ions in defective or nonstoichiometric spinel $MgO\text{-}xAl_2O_3$ ($1.1 \leq x \leq 1.5$) and in perfect or stoichiometric spinel $MgAl_2O_4$ were investigated by Yamaguchi et al. [71] using an electron probe analyzer. According to their findings, the diffusion coefficients of Ni^{2+} ions vary linearly with the concentration of composition-dependent vacancies. The activation energies for Ni^{2+} ion diffusion in defective and perfect spinels are 70 and 106 kcal/mole, respectively. Yamaguchi et al. [71] stated that

composition-dependent vacancies govern the diffusion of cations in the defective or nonstoichiometric spinel while temperature-dependent vacancies contribute to cation diffusion in the perfect or stoichiometric spinel.

Paladino and Kingery [72] measured the self-diffusion of ^{26}Al in polycrystalline aluminum oxide at temperatures of 1670° to 1905°C. In the temperature range studied, the diffusion results are represented as $D(Al)=(28)\exp(-114{,}000/RT)$ cm²/sec. Paladino and Kingery [72] proposed that the diffusion mechanism involves either diffusion via lattice vacancies or migration of Al^{3+} ions via normally unoccupied octahedral sites.

The determination of diffusion coefficients is not limited only to cations; the transport behavior of anions, particularly oxygen, has received great attentions from scientists. Radioactive oxygen, ^{18}O, was used to measure by the gas exchange technique the oxygen diffusion coefficients in oxides such as Cu_2O [73], NiO [74], CdO [75], TiO_2 [76], and calcia-stabilized zirconia [77]. A vacancy mechanism was proposed to explain the movement of oxygen in these oxides [73-77].

Kingery et al. [78] studied the diffusion of ^{18}O in the spinel $NiCr_2O_4$ at temperatures of 1200° to 1600°C and obtained the results $D(O)=(0.017)\exp(-65{,}400/RT)$ cm²/sec. The activation energy for oxygen mobility in $NiCr_2O_4$ is about twice that for oxygen diffusion in cubic fluorite structure calcia-stabilized zirconia, where

$D(O)=(0.018)\exp(-31,200/RT)$ cm^2/sec [77]. The oxygen diffusion coefficient is smaller than that of either cation, Ni^{2+} or Cr^{3+}, in $NiCr_2O_4$ [57-59,65,67].

O'Bryan and DiMarcello [79] measured the diffusion coefficients of oxygen in single crystals of nickel ferrous ferrite as a function of oxygen stoichiometry at temperatures between 1140° and 1340°C. At higher oxygen contents, the diffusion coefficient is independent of oxygen stoichiometry and can be represented as $D(O)=(5 \times 10^{-3})\exp(-61,000/RT)$ cm^2/sec. At low oxygen partial pressures, the diffusion rate depends strongly on oxygen stoichiometry and is smaller in magnitude. O'Bryan and DiMarcello [79] cited that a vacancy mechanism contributes to the diffusion of oxygen in the ferrite.

The self-diffusion of oxygen in single crystal and polycrystalline aluminum oxide was investigated by Oishi and Kingery [80]. They reported that in single crystals of Al_2O_3, intrinsic diffusion occurs between 1650° and 1780°C as $D(O)=(1.9 \times 10^3)\exp(-152,000/RT)$. Below 1650°C, variable results were obtained depending on the impurity content and heat treatment; the experimental results, however, can be represented as $D(O)=(6.3 \times 10^{-8})\exp(-57,600/RT)$ cm^2/sec. The diffusion coefficient of oxygen in polycrystalline samples was reported to be about two orders of magnitude larger than that for single crystal due to enhanced diffusion in the grain boundary regions.

Using the serial sectioning method instead of the commonly employed gas exchange technique [73-80], Reed and Wuensch [81], with the use of an ion probe, measured the mobility of oxygen in single crystals of Al_2O_3 at temperatures of 1585° to 1840°C. Tracer ^{18}O was supplied from an $Al_2{}^{18}O_3$ layer produced by oxidation of a vapor-deposited Al metal film in an $^{18}O_2$ atmosphere. Their results are represented as $D(O)=6.4 \times 10^{5}\exp(-188{,}000/RT)$ cm^2/sec. Compared with the results of Oishi and Kingery [80], the diffusion coefficients obtained by Reed and Wuensch [81] are smaller by a factor of 40 to 70 and are likely to represent extrinsic impurity-controlled transport.

Aside from the measurement of diffusion coefficients of cations and anions in simple and complex oxides, extensive works were carried out on the kinetics of formation of spinels such as $CoAl_2O_4$ [82,86], $ZnAl_2O_4$ [83,98], $NiAl_2O_4$ [83,99-108], $NiCr_2O_4$ [83,88,89,109], $ZnCr_2O_4$ [83], $FeAl_2O_4$ [84,85], Co_2TiO_4 [86], $CoCr_2O_4$ [86], $MnAl_2O_4$ [87,110] and $MgAl_2O_4$ [90-97]. All the results from these studies substantiated Wagner's mechanism of cation counterdiffusion during solid-state formation of spinels [65].

Ivanov and Koroleva [110], studying the interaction of manganese oxide MnO and alumina by infrared spectroscopy, reported that $MnAl_2O_4$ begins to form at 1350°C in pure hydrogen and weakly oxidizing atmospheres. $MnAl_2O_4$ heated in dry hydrogen atmosphere was observed to undergo decomposition at 1600°C. In oxidizing and weakly oxidizing

atmospheres, $MnAl_2O_4$ converts into the spinel $MnMn_2O_4$ and αAl_2O_3.

$NiAl_2O_4$ was observed to form from NiO and Al_2O_3 mixtures heated at temperatures between 700° to 1050°C [111,112]. Its formation was reported to be complete at 1300° to 1400°C [112,113].

Iida et al. [101] reported that the rate of formation of $NiAl_2O_4$ by solid-state reaction increases with an increase in the oxygen partial pressure in the heating atmosphere. The rate of formation increases also with an increase in the heating temperature. Iida et al. [101] suggested that the spinel is formed by counterdiffusion of Ni^{2+} and Al^{3+} ions with the mobility of the Al^{3+} as rate-controlling.

Pettit et al. [103] examined the rate of formation of $NiAl_2O_4$ in argon and in air, and reported that both rates are identical. They cited that the rate of $NiAl_2O_4$ formation is controlled by the diffusion of Al^{3+} ions over the temperature range of 1200° to 1500°C.

Stone and Tilley [108] studied the spinel systems which can be formed from the oxides MgO, NiO, ZnO, CuO, Al_2O_3, Ga_2O_3 and In_2O_3 from the standpoint of reactivity. Their results show that the ease of formation can be represented by the sequence:

1. $CuB_2^{3+}O_4 > ZnB_2^{3+}O_4 \cong MgB_2^{3+}O_4 > NiB_2^{3+}O_4$ (B^{3+}=Al^{3+}, Ga^{3+}, In^{3+})
2. $A^{2+}Al_2O_4 > A^{2+}Ga_2O_4 > A^{2+}In_2O_4$ (A^{2+}= Mg^{2+}, Zn^{2+}, Ni^{2+},

Cu^{2+}).

The formation of $ZnAl_2O_4$ and $NiAl_2O_4$, for example, conforms to the kinetics of diffusion controlled processes with activation energies of 88 and 103 kcal/mole, respectively. The Wagner [65] mechanism of counterdiffusing cations was considered in the spinel formation and the authors pointed out that during spinel formation, cations diffuse predominantly via tetrahedral sites. In the case of $NiAl_2O_4$, Stone and Tilley [108] suggested that the rate of formation is controlled by diffusion of Ni^{2+} ions.

Grimes [114] proposed a theoretical model to systematically analyze the activation energies for self-diffusion of cations and anions in spinels. The model is used to estimate the formation and migration energies for both cation and anion vacancies in the spinel.

Stone and Tilley [115] presented a discussion on diffusion paths available to cations in simple and complex oxides such as spinels. For spinels in particular, the elementary step for a cation in an octahedral site is to move to an unoccupied or empty tetrahedral site Diffusion from an octahedral site is represented by the paths :

1. oct. site - tet. site - oct. site - tet. site - ...
2. oct. site - tet. site - oct. site
3. oct. site - tet. site - oct. site - tet. site - oct. site

Diffusion from a tetrahedral site follows the paths :

4. tet. site - oct. site - tet. site

5. tet. site - oct. site - tet. site - oct. site - tet. site
6. tet. site - oct. site - tet. site - oct. site
7. tet. site - oct. site - tet. site - oct. site

Path 1 is interstitial diffusion via normally unoccupied sites, after an initial step from an occupied position. Path 2 is diffusion between nearest neighboring octahedral sites, and Path 3 is diffusion from an octahedral site to the next nearest octahedral sites, two of which are available.

Path 4 is diffusion to the nearest tetrahedral site, Path 5 to the next nearest tetrahedral site and Path 6 to the nearest octahedral site. Path 7 is the interstitial diffusion analogue of Path 1 . Path 4 affords the minimum repulsion from other cations and movement from one tetrahedral site to another is across an open part of the crystal structure. There are clear cation-free channels along this path and if vacancies exist in the sublattice of tetrahedral cations (or if an interstitialcy mechanism operates) these channels provide the best diffusion path through the structure from the point of view of cation repulsion.

C. Thermodynamics of Spinels (Aluminates)

The thermodynamic properties of spinel system have been studied by equilibrium methods such as the gas equilibration and solid electrolyte emf techniques. Another technique that

has been used successfully to obtain thermodynamic data of spinels involves solution calorimetry in molten oxide solvents.

Using the equilibria of $CO-CO_2$ gas with Ni-NiO and $(Ni+\alpha Al_2O_3)-NiAl_2O_4$ mixtures at temperatures of 682° to 1000°C, Fricke and Weitbrecht [118] calculated the free energy of formation of the spinel $NiAl_2O_4$ from the individual oxides - the reaction being represented as

$$NiO + \alpha Al_2O_3 = NiAl_2O_4 \qquad (1)$$

and obtained a $\Delta G°(1000°C)= -5.0$ kcal/mole.

The thermodynamics of hercynite $FeAl_2O_4$ reduction with CO was studied by Lebedev [119], Novokhatskii and Lenev [120], and Rezukhina et al. [121] in order to determine the free energy of formation of the spinel in the reaction,

$$FeO + \alpha Al_2O_3 = FeAl_2O_4 \qquad (2)$$

Lebedev [119] obtained a $\Delta G°(1273°K)$ for reaction (2) of -10.4 ± 0.6 kcal/mole. Novokhatskii and Lenev [120] reported a $\Delta G°(298°K)= -9.6\pm0.5$ and $\Delta G°(1273°K)= -7.1\pm0.5$ kcal/mole. Rezukhina et al. [121] arrived at the values of $\Delta G°(298°K)= -9.6\pm0.6$ and $\Delta G°(1273°K)= -5.6\pm0.5$ kcal/mole.

The gas equilibration technique was used extensively by Lenev and Novokhatskii [122-124] to measure the thermodynamic properties of the spinel systems $NiAl_2O_4$, $CoAl_2O_4$ and $MnAl_2O_4$. $NiAl_2O_4$ and $CoAl_2O_4$ were equilibrated with CO; $MnAl_2O_4$ with H_2. For the formation of $NiAl_2O_4$ as represented by equation (1), Lenev and Novokhatskii [122-124] reported the thermodynamic values as (in

kcal/mole):

$$\Delta H°(298°K) = -5.9 \pm 0.6$$

$$\Delta H°(1273°K) = -1.6 \pm 0.5$$

$$\Delta G°(T) = -1560 - 2.44T\ (\pm 400)\ \text{cal/mole} \qquad (3)$$

For $CoAl_2O_4$,

$$\Delta H°(298°K) = -9.3 \pm 0.6$$

$$\Delta H°(1273°K) = -6.0 \pm 0.4$$

For $MnAl_2O_4$,

$$\Delta H°(298°K) = -9.0 \pm 1.1$$

$$\Delta G°(298°K) = -10.3 \pm 1.4$$

$$\Delta H°(1273°K) = -11.5 \pm 0.8$$

$$\Delta G°(1293°K) = -9.3 \pm 0.8$$

$$\Delta H°(1873°K) = -12.2 \pm 0.7$$

$$\Delta G°(1873°K) = -7.8 \pm 0.7$$

With regards to the free energy of formation of $NiAl_2O_4$, Lenev and Novokhatskii [122] pointed out that the absolute value of $\Delta G°(T)$, equation (3), increases with temperature. This trend does not agree with usual behavior of $\Delta G°(T)$ for the formation of other spinels, which decreases with increase in temperature. The deviation was attributed by these authors to the inverted cation distribution of $NiAl_2O_4$ [21]. The increase in the absolute value of $\Delta G°(T)$ with temperature of formation of complex oxides can be considered a property of inverted spinels.

The more reliable emf method involving stabilized zirconia was employed extensively by Schmalzried et al [125,126] to calculate the free energy, enthalpy and entropy

of formation of the spinel reaction,

$$AO + B_2O_3 = AB_2O_4 \quad (4)$$

The solid electrolyte cell,

$$Pt|A,B_2O_3,AB_2O_4|CSZ|A,AO|Pt \quad (I)$$

was used in the measurement of the thermodynamic data of spinels (aluminates, chromites and ferrites) at temperatures of 1000° to 1500°K. For the aluminates of Fe, Co, Ni and Mg, Schmalzried [125] obtained the free energy of formation $\Delta G°(1273°K)$= -5.7±0.2, -7.3±0.4, -4.4±0.4 and -8.4±0.4 kcal/mole, respectively; for $CoAl_2O_4$, $\Delta G°(T)$= -10,700+2.67T (±500) cal/mole (1000°-1500°K). A tabulation of the thermodynamic data $\Delta S°$, $\Delta H°$ and $\Delta G°$ for aluminates, chromites and ferrites was given.

A modification of galvanic cell (I) was made by Rezukhina et al. [127-129] in their investigation of the thermodynamics of aluminates and chromites. The electrolyte ThO_2-La_2O_3 was used in place of ZrO_2-CaO. For the aluminates of Fe, Co and Ni, the free energies of formation obtained are: for the formation of $FeAl_2O_4$ at 1235°-1323°K,

$$FeO + \alpha Al_2O_3 = FeAl_2O_4 \quad (5)$$

$$\Delta G°(T)= -10,800+4.085T\ (\pm 35)\ \text{cal/mole} \quad (6)$$

For the formation of saturated solutions of Al_2O_3 in aluminates,

$$NiO + 1.136Al_2O_3 = NiAl_{2.273}O_{4.409} \quad (7)$$

$$\Delta G°(1273°-1673°K)= -5553-0.42T\ (\pm 300)\ \text{cal/mole} \quad (8)$$

$$CoO + 1.235Al_2O_3 = CoAl_{2.47}O_{4.705} \quad (9)$$

ΔG°(1273°-1673°K)= -12,118+3.46T (±300) cal/mole (10)

Using the solid electrolyte emf method, Jacob [135,136] determined the thermodynamics of $CuAl_2O_4$, $CuAlO_2$, Al_2O_3-saturated $NiAl_2O_4$ and $MnAl_2O_4$. For the reactions,

$$Cu_2O + Al_2O_3 = 2CuAlO_2 \quad (11)$$

ΔG°(700°-1100°)= -5670+2.49T (±300) cal/mole (12)

$$CuO + Al_2O_3 = CuAl_2O_4 \quad (13)$$

ΔG°(700°-1100°)= -4403-4.97T (±350) cal/mole (14)

For the formation of Al_2O_3-saturated $NiAl_2O_4$ and $MnAl_2O_4$,

$$NiO + (1+x)Al_2O_3 = NiAl_{2+2x}O_{4+3x} \quad (15)$$

ΔG°= -1499-2.31T (±350) cal/mole (16)

$$MnO + (1+x)Al_2O_3 = MnAl_{2+2x}O_{4+3x} \quad (17)$$

ΔG°= -9025+1.50T (±350) cal/mole (18)

Using the gas equilibration technique, Aukrust and Muan [137] measured the thermodynamics of the phases $CoO-Al_2O_3$, $CoO-Cr_2O_3$ and $2CoO-SiO_2$ at temperatures of 1000° to 1350°C. For the $CoO-Al_2O_3$ phase, the free energy of formation ΔG° at 1000° and 1350°C is -6.9±0.4 and -6.3±0.4 kcal/mole, respectively. These values are more negative than that (-4.9 kcal/mole at 1000°C) reported by Schmalzried [125]. Aukrust and Muan [137] suggested that the large negative value is related to possible nonstoichiometry of the $CoO-Al_2O_3$ phase coexisting in equilibrium with Al_2O_3.

The gas equilibration and solid electrolyte emf methods have provided reliable free energy data for simple spinel systems at elevated temperatures. However, the enthalpies and entropies of formation calculated in conjunction with

the free energy data are less reliable. The entropy and enthalpy data of the component oxides used in the calculation were taken from the works of Kelley [130-132] and Kubaschewski and Evans [133].

Using oxide melt calorimetry with a precision of ±0.1 to 0.5 kcal/mole, Navrotsky and Kleppa [134] measured the enthalpies of formation of aluminates, ferrites, gallates and germanates. The entropies of formation were then calculated from available free energy and measured enthalpy data. Using the oxide melts $9PbO:3CdO:4B_2O_3$ and $3Na_2O:4MoO_3$, Navrotsky and Kleppa [134] obtained for Mg, Co, Ni, Cu, Zn and Cd aluminates the enthalpies of formation $\Delta H°(970°K)$ of -8.72±0.29, -8.90±0.23, -0.74±0.25, 5.17±0.19, -10.56±0.30 and 4.49±0.20 kcal/mole, respectively. For divalent-trivalent (2-3) spinels, the enthalpies of formation were observed to fall in the range of -7 to -11 kcal/mole. Inverted (2-3) spinels, such as $NiAl_2O_4$ and $CuAl_2O_4$, were found to have enthalpies of formation near zero or positive values.

An extensive review of available thermodynamics of ternary oxides has been presented by Kubaschewski [138].

D. Electrical Conductivity of Spinels

The earliest report on electrical conductivity of spinel $MgAl_2O_4$ was published by Jander and Stamm [139]. Using dc measurements, they stated that the electrical conductivity of $MgAl_2O_4$ in air varied from 1.19×10^{-4} at

900°C to 5.32×10^{-4} $ohm^{-1}\text{-}cm^{-1}$ at 1100°C; an activation energy of 28.3 kcal/mole was obtained. For $ZnAl_2O_4$ and $MgCr_2O_4$, activation energies of conduction of 24.6 and 19.8 kcal/mole, respectively, were obtained. From the results, Jander and Stamm [139] stated that $ZnAl_2O_4$ and $MgAl_2O_4$ behave as ionic conductors while $MgCr_2O_4$ is an electronic conductor.

The initial study on the effects of temperature and equilibrium oxygen partial pressure on the electrical conductivity of sintered spinels was undertaken by Bevan et al. [140]. Spinels such as $ZnFe_2O_4$, $ZnCr_2O_4$, $MgFe_2O_4$, $MgCr_2O_4$ and $NiAl_2O_4$ were made by pressing at 1406 kg/cm^2 analytical grade component oxides into plates and sintering the resulting plates at 1000° to 1050°C for 4 to 12 hr. Using dc measurements, Bevan et al. [140] reported that $ZnFe_2O_4$ and $MgFe_2O_4$ exhibit n-type conduction while $ZnCr_2O_4$ and $MgCr_2O_4$, p-type conduction. $NiAl_2O_4$, considered by these authors as a normal spinel, exhibits very poor p-type conduction. $NiAl_2O_4$ which was sintered in air at 1000°C shows low electrical conductivity at temperatures below 735°C; the conductivity of this spinel is smaller in vacuum than in air. The low conductivity values obtained can be attributed to the high percentage of porosity present in the samples which were sintered at low temperatures.

Bradburn and Rigby [141] examined the effects of cation distribution on the electrical conductivity of sintered spinels. The mechanism of conduction in the spinels was

evaluated in terms of crystal and defect chemistry. Although the component oxides were sintered at 1600°C, the resulting spinel samples contained high porosity. Bradburn and Rigby [141] reported that there is no striking difference in the conductivities of normal and inverted spinels. Mg and Zn aluminates and ferrites were found to be n-type conductors; Co and Ni aluminates and chromites, p-type conductors. Like Bevan et al. [140], Bradburn and Rigby [141] assumed $NiAl_2O_4$ to be a normal spinel. Activation energies of conduction for Co, Mg, Ni and Zn aluminates are 35.7, 26.3, 41.9 and 19.8 kcal/mole, respectively. The inconclusive results on the difference in conduction between normal and inverse spinel can be due to the presence of high porosity in the samples tested.

The effects of heating atmosphere on the rate of formation and electrical conductivity of $NiAl_2O_4$ were investigated by Iida et al. [101]. $NiAl_2O_4$ was observed to exhibit p-type conduction at temperatures of 800° to 1300°C and activation energies of conduction of the spinel in (10^{-4} atm O_2) , in air and in pure oxygen are 36.2, 30.8 and 28.9 kcal/mole, respectively.

Nicolescu et al. [142] determined the correlation between catalytic activity and electrical conductivity of the $xNiO-Al_2O_3$ system ($3.0 \leq x \leq 36.6$ wt%) in air and in pure hydrogen at temperatures of 200° to 380°C. The $NiO-Al_2O_3$ system displayed p-type conduction and Nicolescu et al. [142] attributed the conductivity to the concentration of

Ni^{3+} ions in the spinel.

Tkach and Samoilenko [143] measured the electrical conductivity of the $NiO-Al_2O_3$ system containing 1 to 33.3 at% of Al as a function of temperature (20° to 300°C) and oxygen partial pressure (15 to 10^{-5} atm O_2). Experimental results indicate p-type conduction for the $NiO-Al_2O_3$ system; electrical conductivity decreases as the concentration of Al increases, and it increases with increase in oxygen partial pressure. Tkach and Samoilenko [143] proposed that in oxidizing atmospheres, the electrical conduction is due to the formation of holes as Ni^{2+} is converted to Ni^{3+}.

Extensive work on the electrical conductivity of $NiAl_2O_4$ was recently made by Snider [144], using two-probe ac measurements. Results taken at temperatures of 650° to 1200°C and at oxygen partial pressures of 10^{-24} to 10^{-3} atm indicate conductivity independent of oxygen partial pressure. Activation energies of conduction vary from 20.0 to 40.0 kcal/mole, with an average value of 28.5 kcal/mole. Ionic conductivity at 1200°C varies from 5.7×10^{-5} to 8.5×10^{-4} (average of 2.8×10^{-4}) $ohm^{-1}\text{-}cm^{-1}$.

The electrical properties of other spinels such as $MnAl_2O_4$ were studied by Coath and Dailly [145] as a function of temperature (25° to 1200°C) and oxygen partial pressure. The spinel was prepared by a coprecipitation method and sintered in air at 1500°C. X-ray diffraction analysis of the sintered sample revealed, aside from the spinel lines, lines of an oxidation product - probably the presence of $MnMn_2O_4$

[24]. Their report, an extended abstract, indicates that at intermediate and low oxygen partial pressures, plots of log conductivity against reciprocal of temperature show evidence of two linear portions with a definite breakpoint at high oxygen partial pressures. Such plots were complicated by oxidation of the spinel, leading to marked changes in electrical conductivity over small temperature differences. Plots of log conductivity against log oxygen partial pressures are generally linear except at high oxygen partial pressures where oxidation of the spinel was reported. The spinel conductivity increases with temperature at constant oxygen partial pressure and it increases with oxygen partial pressure at constant temperature - an indication of p-type conduction.

Weeks and Sonder [146] determined the electrical conductivity of pure and Fe-doped (1000 ppm) $MgAl_2O_4$ in air and in purified argon at temperatures of 700° to 2000°K. The temperature dependence of conductivity for pure $MgAl_2O_4$ gave activation energies of conduction of 49.8 (high temperature range of 1300°-2000°K), 34.5 (middle temperature range of 950°-1300°K) and 63.1 kcal/mole (low temperature range of 700°950°K). The three activation energies were interpreted as being due to intrinsic carriers at the high temperature range, extrinsic carriers at the intermediate temperature range and extrinsic carriers that are precipitating or aggregating in the lower temperature range. Weeks and Sonder [146] proposed that in the intermediate and low temperature

ranges, conductivity data reflects extrinsic process, possibly cation vacancy motion caused by nonstoichiometry. Conductivity of Fe-doped $MgAl_2O_4$ was greater by a factor of two as a result of Fe^{2+} ions changing to Fe^{3+} ions.

Chaplin et al. [147] investigated the electrical conductivity of coprecipitated chromium oxide-alumina, Cr_2O_3-Al_2O_3, catalysts in air, hydrogen and in vacuum. Results for the conductivity of Cr_2O_3-Al_2O_3 (70:30 wt%) in the temperature range of 200°-500°C indicate p-type conduction. The Cr_2O_3-Al_2O_3 system, after reduction in pure hydrogen at 500°C for 50 hr, exhibits n-type conduction. An activation energy of conduction in air of 18.3 kcal/mole was obtained.

Weisz et al. [148] studied further the electrical conductivity of the chromia-alumina (30:70 wt%) catalyst as a function of oxygen partial pressure (1 to 10^{-6} atm O_2). Conductivity of the catalyst was also measured in pure butane and hydrogen. At 480°C and 1 atm O_2, an electrical conductivity of about 3×10^{-6} ohm^{-1}-cm^{-1} and an activation energy of 41.5 kcal/mole were reported. P-type conduction was observed at oxygen partial pressures of 10^{-6} to 1 atm. N-type conduction was evident when the Cr_2O_3-Al_2O_3 catalyst was exposed to hydrogen and butane. Weisz et al. [148] suggested that the conductivity was influenced by a finite concentration of Cr in the Cr^{4+} state.

Schmalzried [69,149] measured the electrical conductivity of $CoCr_2O_4$ and $CoAl_2O_4$ between 900° and 1100°C

and in oxygen partial pressures of 10^{-16} to 1 atm. $CoCr_2O_4$ was observed to exhibit p- and n-type conduction with a conductivity minimum at about 10^{-8} atm O_2. At $P < 10^{-8}$ atm O_2, $CoAl_2O_4$ exhibited ionic conductivity independent of oxygen partial pressure. Schmalzried stated that the conductivity of $CoCr_2O_4$ was due to excess of cations, with Co^{2+} ions on interstitial sites and Cr vacancies. A deficit of cations with Al^{3+} ions on interstitial sites and Co vacancies contributed to the conductivity in $CoAl_2O_4$ [69].

III. Theory

A. Crystal Structure of Spinel

Following the approach of Sun [67], it should be noted that each occupied octahedral site in a spinel is surrounded by 12 nearest similar sites ($\sqrt{2}/4$)a_o away, of which 6 are occupied (see Fig. 2). Each occupied octahedral site is also surrounded by 8 nearest tetrahedral sites ($\sqrt{3}/4$)a_o away, all unoccupied. On the other hand, each occupied tetrahedral site is surrounded by 6 nearest similar sites (1/4)a_o away, all unoccupied. Each of the tetrahedral sites is also surrounded by 4 nearest octahedral sites ($\sqrt{3}/8$)a_o away, all unoccupied.

Comprehensive reviews of the spinel structure and the crystal chemistry of compounds crystallizing in this structure are available in the literature [54,55].

B. Electrical Conductivity of Solid Electrolytes

The electrical conductivity of an oxide MO is given by the equation,

$$\sigma = \Sigma_i \ (n_i \ z_i \ \mu_i) \qquad (19)$$

where n_i is the concentration of charge carrier i, z_i is its charge, and μ_i its mobility (drift velocity in unit potential gradient). The charge carriers i will generally be point defects. In an oxide MO, the point defects include M

and O vacancies and M and O interstitial atoms or ions. Other charge carriers include electrons and electronic holes.

For oxides with more than one charge carrier, the total conductivity is given by,

$$\sigma = \sigma_1 + \sigma_2 + \sigma_3 + \ldots + \sigma_i \qquad (20)$$

The fraction of the total conductivity contributed by each charge carrier is,

$$t_i = \sigma_i / \sigma \qquad (21)$$

where t_i is the transport number.

Consider an oxide MO to contain as defects doubly ionized M vacancies V_M'', doubly ionized O vacancies $V_O^{\cdot\cdot}$, electrons e' and holes h°. There are four unknown defect concentrations: n, p, $[V_M'']$ and $[V_O^{\cdot\cdot}]$. These defect concentrations are related in several ways:

1. In the formation of ionic disorder (e.g.,Schottky defects),

$$nil = [V_M''] + [V_O^{\cdot\cdot}] \qquad (22)$$

$$\text{or } K_S = [V_M''][V_O^{\cdot\cdot}] \qquad (23)$$

2. In the formation of electronic disorder,

$$nil = e' + h^\circ \qquad (24)$$

3. In the reaction of oxygen with the oxide,

$$1/2O_2(g) = O_O + V_M'' + 2h^\circ \qquad (26)$$

$$[V_M'']p^2 = K_A P(O_2)^{1/2} \qquad (27)$$

4. In the transfer of an oxygen atom in the solid to the

gaseous state,

$$O_O = V_O^{\cdot\cdot} + 1/2O_2(g) + 2e' \quad (28)$$

$$[V_O^{\cdot\cdot}]n^2 = K_B \; P(O_2)^{-1/2} \quad (29)$$

5. In the condition for electrical neutrality,

$$2[V_M^{''}] + n = 2[V_O^{\cdot\cdot}] + p \quad (30)$$

For the situations where the concentrations of defects are such that $2[V_M^{''}] \gg n$ and $p \gg 2[V_O^{\cdot\cdot}]$, equation (30) becomes

$$2[V_M^{''}] = p \quad (31)$$

The dependence of the concentrations of defects on oxygen pressure can be worked directly from the given equations. For instance, $[V_M^{''}]p^2 = K_A \; P(O_2)^{1/2}$ but $2[V_M^{''}] = p$. Substituting equation (31) into equation (27) gives

$$4[V_M^{''}]^3 = p^3/2 = K_A \; P(O_2)^{1/2} \quad (32)$$

$$2[V_M^{''}] = p = K_A' \; P(O_2)^{1/4} \quad (33)$$

$$p \propto P(O_2)^{1/4} \quad (34)$$

Since $np = K_i$,

$$n = [K_i/K_A']P(O_2)^{-1/4} \quad (35)$$

$$n \propto P(O_2)^{-1/4} \quad (36)$$

and since $K_S = [V_O^{\cdot\cdot}][V_M^{''}]$,

$$[V_O^{\cdot\cdot}] = [2K_S/K_A']P(O_2)^{-1/4} \quad (37)$$

The electron hole concentration or the p-type conductivity is proportional to $P(O_2)^{1/4}$ in the region of high oxygen pressure. On the other hand, the electron concentration or n-type conductivity is proportional to $P(O_2)^{-1/4}$ in the region of low oxygen pressure. The variation of conductivity and electrolytic region with

oxygen partial pressure are illustrated in Fig. 3 and 4, respectively.

For an ionic crystal, Schmalzried [151] introduced the parameters $P_{\oplus}$, where $\sigma_{\oplus} = \sigma_i$ and $P_{\ominus}$, where $\sigma_{\ominus} = \sigma_i$ .As shown in Fig. 5, the transference number for electronic charge carriers becomes 0.5 at $P_{\oplus}$ and $P_{\ominus}$. Generally, $P_{\oplus}$ and $P_{\ominus}$ represent the ultimate limiting values for the use of the compound as a solid electrolyte.

For a comprehensive discussion of electrical conductivity and defect chemistry of solid electrolytes, the reader is referred to the works of Kroger [152], Kofstad [153] and Brooks [154]. A complete review of the electrical properties of a number of solid oxide electrolytes has been presented by Etsell and Flengas [155]. Other reviews on the electrochemistry of solid electrolytes are available in the literature [5-10,156-158].

C. DC Polarization Measurements

The dc polarization measurement was introduced by Hebb [159] in 1952; it was improved by Wagner [160-162]. The dc polarization method has been used to study the partial ionic and electronic conductivities in electrolytes such as AgBr [160-164], AgI [163], CuCl, CuBr and CuI [165], $PbCl_2$ and $PbBr_2$ [166], TlBr [167], calcia-zirconia and yttria-thoria [168] and β-alumina [11]. Generally, cells with one reversible electrode and one electrode blocking either ions or electrons are used in the dc polarization

measurements.The polarization cell (II),

rev. electrode|electrolyte|nonrev. electrode (II)

is subjected to a dc emf below the decomposition voltage of the specimen. When a dc voltage is applied to the cell with the reversible electrode negative and the positive positive, cationic current flows from the inert to the reversible electrode. After an initial transient transport of ions through the electrolyte, the ionic current decreases to zero due to the blocking action of the nonreversible electrode. At steady state, ionic current is blocked and current consists only of the excess electron and positive hole conductivity contributions.

As proposed by Wagner [160-162], local equilibrium is assumed between the ions, electrons, holes and neutral species at every location within the electrolyte. Using the assumption of concentration-independent electronic mobilities, the partial electronic conductivities are related to the steady-state current densities I_∞ by the eq.,

$$I_\infty = (RT/FL)\{ \sigma_n [1-\exp(-v)] + \sigma_h [\exp(v)-1] \} \quad (38)$$

when cations are the mobile species, and

$$I_\infty = (RT/FL)\{ \sigma_h [1-\exp(-v)] + \sigma_n [\exp(v)-1] \} \quad (39)$$

when anions are the mobile species. In the eq. (38) and (39), $v = |E|F/RT$ and σ_n and σ_h are the partial conductivi of electrons and positive holes, respectively. In addition, L= thickness of the specimen, R= gas constant, F= Faraday constant and E= applied emf.

The variation of I_∞ with E depends on the values of σ_n and σ_h .If $\sigma_n >> \sigma_h$, according to equation (38), I_∞ should increase at a decreasing rate with increasing E until a plateau is reached where

$$I_\infty \cong \sigma_n (RT/FL) \quad (40)$$

; and σ_n can be obtained from the plateau of a log I_∞ vs E plot.

At higher applied voltages, the hole conductivity becomes more important and equation (38) may be approximated by the following relations:

$$\text{Log } I_\infty = \text{Log}(\sigma_h RT/FL) + (EF/2.3RT) \quad (41)$$

$$\text{Log } I_\infty (FL/RT) = \text{Log } \sigma_h + (EF/2.3RT) \quad (42)$$

if $E >> RT/F$ and $E >> (RT/F)\ln(\sigma_n/\sigma_h)$. σ_h may be obtained from the intercept of a log I_∞ vs. E plot.

Reviews of this technique are available in the literature [152,169,170].

D. Transport Numbers By Emf Measurements

The emf of concentration cells in which diffusion may occur can be obtained using the principles of irreversible thermodynamics. Indirectly, the estimation of transport numbers of the conducting species can be made from such cells. These concentration cells, particularly those involving phases of locally variable composition, have been fully discussed by Wagner [171] and reviewed by Rossotti [172].

The emf E of a galvanic cell may be calculated from the equation,

$$E = -dG/dq \tag{43}$$

in which the change dG in the Gibbs free energy upon passing the electrical charge dq across the cell is equal to the reversible electrical work $\int -E dq$ done on the cell. The alternative form of equation (43) is given as,

$$\Delta G = -EF \tag{44}$$

For the cell, each section remains electrically neutral since the net transport of charge across each cross section is the same. The changes in the amounts of the individual ions in the cell may be represented in terms of changes in the amounts of electrically neutral combinations (α,β) where α is a cation and β is an anionic component, including the electrically neutral component represented by γ. For multicomponent systems, the chemical potentials $\tilde{\mu}_{\alpha,\beta}$ are not independent of each other, and any component of a given phase may be selected as the reference component with A as the master cation and B as the master anion.

Thus, the emf E of a concentration cell with phases locally variable composition has been derived by Wagner [171] for the following cases:

1. If both cell electrodes are reversible for the same cation,

$$E = (-1/F)(\Sigma_\beta \int t_\beta \, d\tilde{\mu}_{A,\beta}) \tag{45}$$

where t_β is the transference number of the component involved,

2. If both cell electrodes are reversible for the same anion,

$$E = (-1/F)(\Sigma_\alpha \int t_\alpha \, d\tilde{\mu}_{\alpha,B}) \qquad (46)$$

Equation (46) was used by Fischer and Hoffmann [173] in the study of the solid spinel cell,

(-)Pt,O_2|MgO+$MgAl_2O_4$|$MgAl_2O_4$|Al_2O_3+$MgAl_2O_4$|O_2,Pt(+) (III)

with equal partial pressures at both electrodes. Oxygen ions were taken as the reference component and electronic conduction was considered negligible, i.e., $t_e = 0$. From the Gibbs-Duhem equation, the emf of the cell was found to be

$$E = (-1/6F) \int_{\tilde{\mu}'_{Al_2O_3}}^{\tilde{\mu}^{O}_{Al_2O_3}} (t_{Al^{3+}} - 3t_{Mg^{2+}}) d\tilde{\mu}_{Al_2O_3} \qquad (47)$$

where $\tilde{\mu}'_{Al_2O_3}$ is the chemical potential of Al_2O_3 in $MgAl_2O_4$ coexisting with MgO. From eq. (47), it follows that $E < 0$ if $t_{Al^{3+}} > 3t_{Mg^{2+}}$ and $E > 0$ if $t_{Al^{3+}} < 3t_{Mg^{2+}}$. Measurements by Fischer and Hoffmann [173] indicated that E was negative, i.e., the average value of $t_{Al^{3+}}$ is greater than the average value of $3t_{Mg^{2+}}$.

IV. Experimental

A. Material Preparation

The spinels - $NiAl_2O_4$ and $MnAl_2O_4$ - were prepared by directly mixing the component oxides at equimolar ratio with the use of a vibrating Spex Mixer (Spex Industries, Inc., Scotch Plains, NJ) for 10 min. Each oxide mixture - $NiO-Al_2O_3$ and $MnO-Al_2O_3$ - was further mixed using an agate mortar and pestle in order to break up any lumps formed in the initial stage of mixing. Each mixture was compacted at 1406.2 kg/cm^2 in a steel die into pellets about 1.27 cm in diameter and about 1.905 cm thick. Each mixture was allowed to react by sintering the pellets on high-alumina boats for 24 hr at 1400°C in a Sentry Electric Tube Furnace with SiC heating elements (The Sentry Co.,Foxboro,Mass.). The $NiO-Al_2O_3$ pellets were sintered in air; $MnO-Al_2O_3$ pellets in purified argon. The phase diagrams of $NiO-Al_2O_3$ and $MnO-Al_2O_3$ are shown in Fig. 6 and 7, respectively.

After sintering, the pellets of each spinel were milled for 24 hr at 65 rpm with a 1 liter polyethylene jar filled to 1/3 with 1.27 cm high-density, high-alumina grinding balls and 1 ml ethanol:1 gm pellets. The slurry was filtered and dried at 100°C for 24 hr. The dried $NiAl_2O_4$ cake was heated for 24 hr at 1000°C in air ($MnAl_2O_4$ cake in purified argon) to drive off any plastic residues accumulated during grinding. X-ray diffraction analyses of each spinel powder revealed only lines of the respective spinel - an indication

of complete reaction. The particle size distribution of each spinel powder was determined with a Coulter Counter Model TA II (Coulter Electronics Inc.,Hialeah, Fl); the mean particle size of the $NiAl_2O_4$ and $MnAl_2O_4$ powders were 10.38 and 5.39 μm , respectively (100% passing 50.8 μm for both spinel powders).

Each spinel powder was pressed at 1406 kg/cm^2 in a steel die into disks or pellets 1.27 cm. in diameter and about 0.63 cm thick. The pellets were initially sintered on high-alumina boats at 1400°C for 48 hr ($NiAl_2O_4$ pellets in air and $MnAl_2O_4$ pellets in purified argon) using the Sentry Electric Tube Furnace. This was followed by another sintering at 1700°C for 5 hr in a LeMont oxygen natural gas fired furnace (LeMont Scientific, Inc.,State College, PA). The color of the $NiAl_2O_4$ pellets was azure blue; $MnAl_2O_4$ pellets, brown.

Flat faces of each sintered pellet were ground and polished parallel. Each pellet was weighed and its dimensions, diameter and thickness measured with a vernier caliper. From the weight and external dimensions, the bulk density of each pellet was calculated. The average weight, diameter, thickness and bulk density of each set of pellets were 1.32±0.06 gm, 1.058±0.004 cm, 0.345±0.017 cm and 4.36±0.05 gm/cm^3, respectively for $NiAl_2O_4$; 1.24±0.05 gm, 1.075 cm, 0.350±0.012 cm and 3.88±0.03 gm/cm^3, respectively, for $MnAl_2O_4$.

The theoretical density of each spinel was calculated with the use of lattice constants available in the literature and the spinel crystal structure. $NiAl_2O_4$ with a lattice constant a_o=8.046 Å [174,175] has a theoretical density of 4.506 gm/cm³; $MnAl_2O_4$ with a_o=8.258 Å [174,175] has a theoretical density of 4.078 gm/cm³. Average theoretical densities of 96.83 and 95.23 % were obtained for the sintered $NiAl_2O_4$ and $MnAl_2O_4$ pellets, respectively. The $NiAl_2O_4$ pellets were designated as B1 to B40; $MnAl_2O_4$, D1 to D42.

Chemicals

In the preparation of the pellets, all reagents in the purest form were purchased primarily from Cerac/Pure Inc. (Menomonee Falls, Wisc.). The purity of each reagent is listed below.

1. Nickel Oxide, NiO
   -325 mesh, typically 99.995% pure
2. Manganese Oxide, MnO
   -100 mesh, typically 99.9% pure
3. Aluminum Oxide, Al_2O_3
   -325 mesh (calcined), typically 99.99% pure

Gas Mixtures

To provide the oxygen partial pressures required for each test run, preanalyzed gas mixtures, $Ar-O_2$ and $CO-CO_2$, were used. The preanalyzed gases were purchased from Matheson of Canada (Whitby, Ontario). The analysis of each gas mixture is listed below:

1. Oxygen
   extra dry, 99.6% minimum

2. Argon
   ultra-high purity, typically 99.999% pure
   oxygen=1-2 ppm
   nitrogen=3-4 ppm
   carbon dioxide < 1 ppm
   total hydrocarbons (THC) < 1 ppm

3. Argon-Oxygen

   a. O_2=1.3 ppm
      Ar=balance

   b. O_2=0.0092%
      Ar=balance

   c. O_2=0.107%
      Ar=balance

   d. O_2=1.02%
      Ar=balance

4. CO-CO_2

   a. CO=0.102%
      O_2=0.0014%
      N_2=0.0070%
      THC=0.00123%
      CO_2=balance

   b. CO=1.99%
      O_2=0.01%
      N_2=0.0023%
      THC=0.00138%
      CO_2=balance

   c. CO=54.6%
      O_2=0.0052%
      N_2=0.0177%
      THC=0.00052%
      CO_2=balance

   d. CO_2=2.02%
      O_2=0.0157%
      N_2=0.0248%
      THC=0.0021%
      CO=balance

   e. CO_2=0.120%
      O_2=0.0105%
      N_2=0.0324%
      THC=4.2 ppm

CO=balance

B. Two-Probe AC Conductivity Measurements

Prior to any conductivity measurement, both faces of each pellet were platinized with a platinum paste (Englehard No.6082) which was then fired ($NiAl_2O_4$ in air; $MnAl_2O_4$ in purified argon) at 800°C for 3 hr to drive off the organic binder.

The conductivity measurements were conducted inside an alumina tube (4.44 cm O.D., 50.80 cm long with one end closed) which was closely fitted inside a Harrop resistance wire-wound tube furnace (Harrop Laboratories, Columbus, Ohio). The spinel pellets of about 1.06 cm in diameter and 0.35 cm thick were assembled into a conductivity cell,

Pt|electrolyte(spinel pellet)|Pt (IV)

in an alumina cell holder (1.90 cm O.D., 45.72 cm long) shown in Plate 1 . The alumina holder was attached to a water-cooled brass head which was tightly attached on the enclosing alumina tube by means of an O-ring assembly. The brass head contained 5 ports for gas inlet and outlet, the Pt lead wires and the Pt thermocouple.

In the assembled cell, the pellets were separated by Pt foils (0.01 cm thick) which were welded into Pt lead wires (0.05 cm in diameter). The cell was held suspended in the cell holder in the surrounding atmosphere by the compressive force of a spring on an alumina pushrod.

To reduce thermal gradients during test runs, the cell holder was centered in the 5-cm working zone of the tube furnace. To eliminate any electrical pickup, a grounded tube of Pt foil was attached to the alumina tube.

The cell temperature was monitored with a Pt-Pt+13% Rh thermocouple which was connected to a digital thermometer (Fluke Model 2100A). The tube furnace was controlled to within ±1°C by means of a solid-state PID controller (Barber-Colman Model 520).

Resistance of the cell was measured as a function of oxygen partial pressure at constant temperature. Readings were taken at temperatures of 800° to 1400°C at 100°C intervals. The conductivity was then calculated using the equation,

$$\sigma = L/RA \qquad (48)$$

where R= measured resistance, L= thickness of the pellet, and A= effective area of the Pt electrode, which in this case was the facial area of the pellet.

Oxygen partial pressures or activities were established with preanalyzed gas mixtures and reversible or coexistence electrodes. In test runs employing gas mixtures, oxygen partial pressures were achieved using preanalyzed $Ar-O_2$ and $CO-CO_2$ gases. The appropriate gases were dried with $Mg(ClO_4)_2$ and P_2O_5 and the flow rates controlled by calibrated flowmeters (Matheson Flowmeter Tubes No. 600 and 601). The gases entered the alumina tube via the cell holder and exited through one of the ports in the brass head. For

each conductivity measurement, the enclosing chamber was initially purged with the desired gas mixture at 150 ml/min for 30 min; the gas flow rate was then reduced to 50 ml/min to allow the cell to equilibrate with the surrounding gas phase. Prior to every test run, the newly assembled cell was heated at 1000°C for 12 hr in order to allow the Pt foil electrodes to sinter on the platinized surfaces of each pellet and thus ensure good contacts between the pellet and the Pt electrodes. Throughout the series of conductivity measurements, the cell responded instantaneously to the surrounding oxygen partial pressures.

For the $CO-CO_2$ gas mixtures, the theoretical oxygen partial pressures were calculated using the reaction,

$$2CO + O_2 = 2CO_2 \qquad (49)$$

and the standard free energy for reaction (49) as given by Kubaschewski et al. [133],

$$\Delta G^\circ = -135{,}000+41.50T \qquad (50)$$

From this equation [177],

$$\log P(O_2)=2\log[P(CO_2)/P(CO)]-[29{,}502.8/T]+9.0694 \qquad (51)$$

In the conductivity measurements involving coexistence or reversible electrodes, oxygen partial pressures or activities were achieved with metal-metal oxide mixtures (5:1 weight ratio) - $Cu-Cu_2O$, Co-CoO, Ni-NiO, Fe-FeO, $Mo-MoO_2$, $Cr-Cr_2O_3$, Mn-MnO, V-VO, Nb-NbO - and metal oxide-metal oxide mixtures (1:1 weight ratio) - Cu_2O-CuO and $Fe_2O_3-Fe_3O_4$ - in the form of the cell,

Pt|rev. electrode|electrolyte|rev. electrode|Pt (V)

with a new pellet used with each set of reversible electrodes. The reversible electrodes were prepared with Fisher Certified Grade reagents. Each electrode mixture was compacted at 1406 kg/cm² in a steel die into pellets 1.27 cm in diameter and 0.63 cm thick. The pellets were then sintered on alumina boats at 1000°C under vacuum for 5 hr to improve their "green" strength. Flat faces of each electrode were ground parallel. The oxygen activity of each reversible electrode was determined from the general reaction,

$$M + O = MO \qquad (52)$$

and the standard free energies for each electrode as given in the literature [133,158,178]. (Data for reversible electrodes are given in Table 2).

For cell (V) employing reversible electrodes, an inert atmosphere was maintained by flowing 50 ml/min ultra-high purity argon that was initially passed through Ti getter chips heated at 800°C.

Frequency dependence of the electrolyte was first studied for both $NiAl_2O_4$ and $MnAl_2O_4$. Conductivity measurements on galvanic cell (IV) containing one pellet per cell were made using a General Radio GR 1608-A Impedance Bridge with a Type 1310 Oscillator in the frequency range of 200 to 10,000 Hz (experimental set-up shown in Fig. 8). Resistance readings were taken as a function of imposed frequency at temperatures of 676°C (10^{-4} and 10^{-14} atm O_2) and 911°C (10^{-4} and 10^{-14} atm O_2). For both spinels,

conductivity was observed to be independent of frequency in the range of 600 to 10,000 Hz. All subsequent resistance or conductivity readings were made at 1000 Hz with an impedance bridge having a built-in microprocessor - General Radio Model 1658 Digibridge with a five-digit LED display and an accuracy of ±0.1%.

The upper and lower limits of thermodynamic stability of both spinels were determined. $NiAl_2O_4$ is highly stable in air and its lower limit of thermodynamic stability as represented by the reaction,

$$NiAl_2O_4 = Ni + 1/2O_2 + Al_2O_3 \quad (53)$$

was calculated using the equations,

$$Ni + 1/2O_2 = NiO \quad (54)$$

$$NiO + Al_2O_3 = NiAl_2O_4 \quad (1)$$

and the standard free energies given by Kubaschewski et al. [133] for equation (54) and by Jacob [136] for eq.(1).

For $MnAl_2O_4$, its lower limit of thermodynamic stability,

$$MnAl_2O_4 = Mn + 1/2O_2 + Al_2O_3 \quad (55)$$

was determined from the equations,

$$Mn + 1/2O_2 = MnO \quad (56)$$

$$MnO + Al_2O_3 = MnAl_2O_4 \quad (57)$$

and the standard free energies given by Kubaschewski et al. [133] for equation (56) and by Jacob [136] for equation (57). The upper limit of thermodynamic stability of $MnAl_2O_4$,

$$3MnAl_2O_4 + 1/2O_2 = Mn_3O_4 + 3Al_2O_3 \quad (58)$$

was calculated from the reactions,

$$3MnO + 1/2O_2 = Mn_3O_4 \quad (59)$$

$$MnO + Al_2O_3 = MnAl_2O_4 \quad (60)$$

with the standard free energies for reaction (59) supplied by Charette and Flengas [178] and for reaction (60) by Jacob [136]. A tabulation of the upper and lower limits of thermodynamic stability of $NiAl_2O_4$ and $MnAl_2O_4$ is given in Tables 3 and 4.

Conductivity measurements in gas mixtures were conducted for $NiAl_2O_4$ and $MnAl_2O_4$ at oxygen partial pressures beyond their limits of thermodynamic stability. Similarly, measurements were also made for both spinels at oxygen activities or partial pressures within their limits of thermodynamic stability. After completing the measurements, the pellets of each cell were analyzed by x-ray diffraction . For the conductivity measurements with oxygen activities being established with preanalyzed gas mixtures or reversible electrodes, two spinel pellets or samples per galvanic cell were used.

C. DC Polarization Measurements

Dc polarization cells similar to cell (II)

$$(-)Pt\left|\begin{matrix}\text{Reversible}\\\text{Electrode}\end{matrix}\right|\begin{matrix}\text{Electrolyte}\\\text{Specimen}\end{matrix}\left|\begin{matrix}\text{Nonreversible}\\\text{Electrode}\end{matrix}\right|Pt(+) \quad (VI)$$

were used to directly estimate the values of the partial

conductivities in $NiAl_2O_4$ and $MnAl_2O_4$ and indirectly determine the transport numbers of the conducting carriers.

For the polarization cell containing $NiAl_2O_4$ as the electrolyte (one pellet per cell), a 0.01 cm thick nickel foil (Sherritt Gordon Stamping Grade Nickel Strip) was used as the reversible electrode. A porous Pt coating on one face of the pellet served as the nonreversible electrode. The Pt layer was formed by coating one face of the pellet with Pt paste (Englehard No.6082) which was fired at 800°C for 3 hr. Pt foils (0.01 cm thick) welded to Pt lead wires (0.05 cm in diameter) served as common conductors for the cell.

For the cell containing $MnAl_2O_4$ pellet, a Mn disk about 1.27 cm. in diameter and about 0.30 cm thick (Alfa Products, Danvers, MA) was used as the reversible electrode and a Pt coating or layer was used as the nonreversible electrode. 0.01 cm thick Pt foils welded to Pt lead wires 0.05 cm in diameter were used as conductors for both cells.

The dc polarization cell was suspended in the cell holder by the compressive force of a spring on the alumina push rod. In the dc polarization measurements, current was measured as a function of impressed voltage. A dc voltage of 30 to 600 mv was impressed on each cell at 25 mv increments with the use of a potentiostat/galvanostat (Princeton Applied Research Model 371) and current was monitored with the use of a Keithley 171 Digital Electrometer (with input impedance of 10 megohms). Prior to any polarization measurement, a voltage of 200 mv was applied on the cell

heated at 1000°C for 12 hr in order to reduce all the ionic currents to zero. After every incremental change in the impressed voltage, steady-state current readings were obtained within 1 minute. There was good agreement between currents obtained with ascending and descending voltages.

Current readings for the $NiAl_2O_4$ cell were taken at temperatures of 800° to 1400°C (800° to 1200°C for the $MnAl_2O_4$ cell) at 100°C intervals. For the cell containing the $NiAl_2O_4$ pellet, measurements were made in 1.3×10^{-4} atm O_2 with an Ar-O_2 mixture and at oxygen partial pressures of 9.25×10^{-16} (800°C) to 6.72×10^{-4} atm (1400°C) with a CO-CO_2 mixture.

For the cell containing $MnAl_2O_4$, current readings were taken at oxygen partial pressures of 2.59×10^{-19} (at 800°C) to 7.58×10^{-12} atm (at 1200°C), and from 1.57×10^{-23} (at 800°C) to 4.61×10^{-15} atm (at 1200°C).

D. Emf Measurements

The concentration cells similar to the one used by Fischer and Hoffmann [173],

$(-)Pt,O_2|MgO+MgAl_2O_4|MgAl_2O_4|Al_2O_3+MgAl_2O_4|O_2,Pt(+)$ (III)

were used to determine qualitatively the conducting ion or ions in $NiAl_2O_4$ and $MnAl_2O_4$. The concentration cells used are represented by,

$(-)Pt,O_2|NiO+NiAl_2O_4|NiAl_2O_4|Al_2O_3+NiAl_2O_4|O_2,Pt(+)$ (VII)

$(-)Pt,O_2|MnO+MnAl_2O_4|MnAl_2O_4|Al_2O_3+MnAl_2O_4|O_2,Pt(+)$ (VIII)

In cell (VII) containing $NiAl_2O_4$, the left electrode, $NiAl_2O_4$+NiO, was prepared by mixing NiO and Al_2O_3 powders at a 2:1 molar ratio; for the electrode on the right, $NiAl_2O_4$+Al_2O_3, NiO and Al_2O_3 were mixed at a 1:2 molar ratio. For cell (VIII) containing $MnAl_2O_4$, MnO and Al_2O_3 were mixed at 2:1 molar ratio for the left electrode, $MnAl_2O_4$+MnO; 1:2 molar ratio for the right electrode, $MnAl_2O_4$+Al_2O_3.

Each electrode mixture was mixed for 10 min with a Spex Mixer; this was followed by additional mixing in an agate mortar and pestle to break up any lumps formed in the initial stage of mixing. Each electrode mixture was then compacted at 1406 kg/cm² in a steel die into pellets 1.27 cm. in diameter and 1.90 cm thick. The 2NiO:1Al_2O_3 and 1NiO:2Al_2O_3 pellets were sintered in air at 1400°C for 24 hr; the 2MnO:1Al_2O_3 and 1MnO:2Al_2O_3 pellets in purified argon. The resulting sintered pellets were further ground into powder (100% passing 74 μm) in an agate mortar and pestle, and subsequently compacted at 1406 kg/cm² in a steel die into disks or pellets about 1.27 cm. in diameter and about 0.63 cm thick. These pellets were given further sintering at 1400°C for 48 hr (electrodes for the $NiAl_2O_4$ cell in air; electrodes for the $MnAl_2O_4$ cell in purified argon).

The emf of the each cell was measured as a function of temperature. Steady-state emf readings were taken at temperatures of 800° to 1400°C at 100°C intervals. The emf

readings were measured with the use of a Keithley Model 171 Electrometer connected to a Simpson Dual Channel Potentiometric Recorder (Model 2742 A-B).

To minimize any electronic conduction during measurement, the emf of each cell was measured at oxygen partial pressures within the ionic conduction region of each spinel as determined by the ac conductivity method. The emf of the $NiAl_2O_4$ cell was measured in air. For the $MnAl_2O_4$ cell, the emf was measured in oxygen partial pressures of 1.57×10^{-23} (800°C) to 1.14×10^{-12} atm (1400°C), with a CO-CO_2 mixture containing 54.6% CO.

V. Results and Discussion

A. Nickel Aluminate

A brief description of some of the physical properties of the component oxides will be given before analyzing the experimental results.

One of the component oxides of the spinel $NiAl_2O_4$ is NiO. NiO has a halite crystal structure where the anions are cubic close-packed and the smaller cations occupy the octahedral interstices [153]. At higher partial pressures of oxygen, the oxide is metal deficient ($Ni_{1-y}O$). The predominant point defects in the pure oxide are nickel vacancy type defects. Deviations from stoichiometry in NiO as a function of oxygen partial pressure have been studied by Mitoff [179], Sockel and Schmalzried [180], Tretyakov and Rapp [181], Tripp and Tallan [182], and by Zintl [183]. From these studies, it was concluded that $y \propto P(O_2)^{1/4}$ and the nickel vacancies are doubly charged. Zintl [183] determined the fraction of vacancies in NiO specimens quenched in air from 1000°C and obtained a value of 1.25×10^{-4}. In addition, electrical conductivity measurements on NiO [179,192-198] indicate that conduction in the oxide is by a vacancy mechanism.

The other component oxide is Al_2O_3, which has a corundum or rhombohedral structure. The corundum structure can be regarded as a hexagonal close-packing of oxygen ions with the trivalent Al^{3+} ions occupying 2/3 of the octahedral

sites. As the metal ions occupy the octahedral sites, each metal ion is octahedrally coordinated and surrounded by six oxygen ions, while each oxygen ion is surrounded by four metal ions.

αAl_2O_3 is generally the stable form of alumina at all temperatures but a cubic form, γAl_2O_3 can also be formed [184].

Using electron and x-ray diffraction techniques, Finch and Sinha [184] studied the spinel reaction,

$$AO + B_2O_3 = AB_2O_4 \qquad (4)$$

and reported that the B_2O_3 components such as αAl_2O_3, αFe_2O_3, and αCr_2O_3 undergo transformation to their γ-forms before reacting in the solid state with the AO component. On conversion from α to γ, the hexagonal close-packed arrangement of oxygen ions transforms into a cubic close-packing. The γ-form of these components has a defect spinel structure and γ-alumina has a formula represented as $Al[V_{\frac{1}{3}}Al_{\frac{2}{3}}]O_4$ where V stands for lattice vacancies; these vacancies were observed to reside mainly in the octahedral sites [27-29,184].

Electrical conductivity [185,186] and thermoelectric power [187-189] measurements on Al_2O_3 suggest that conduction in Al_2O_3 is by aluminum vacancies V'''_{Al}. However, two studies [190,191] on the electrical conductivity of Al_2O_3 propose Al interstitials as the predominant defect in the oxide.

The inverse structure of $NiAl_2O_4$ can be considered as a specific defect structure since all the crystallographically identical sites within the cell unit are not occupied by the same cation [174]; this suggests that the most probable defects in the spinel are either cation vacancies or interstitials. Frenkel defects such as oxygen interstitials are not probable in $NiAl_2O_4$. Frenkel defects are probable in crystals with a lattice structure which is sufficiently open to accommodate interstitial ions without much distortion, i.e., in crystals of low coordination number. Structures of higher coordination number such as spinels have little room for interstitial ions [174]. The oxygen lattice of the spinel structure is close-packed cubic with the tetrahedral and octahedral sites having radii of 0.6-1.0 Å [174]. To form or move an interstitial oxygen ion with a radius of 1.40 Å [199] in a spinel structure would require an activation energy which is far greater than that for vacancy formation or movement.

Conductivity Measurements

As for the experimental results obtained using the two-probe ac method, Fig. 9 , 12 and 13 show the conductivity isotherms of tests conducted using preanalyzed gas mixtures to fix the required oxygen partial pressures. Fig. 14 gives the results of the measurements employing reversible electrodes to establish the oxygen activities of the conductivity cell. Broken lines in the conductivity isotherms of Fig. 9 and 14 indicate the lower thermodynamic

stability limits of $NiAl_2O_4$ as tabulated in Table 3. Fig. 12 and 13 represent results taken within the limit of thermodynamic stability of $NiAl_2O_4$.

In Fig. 9, results only up to 1100°C were obtained in the measurements covering the oxygen partial pressure range (including the metastable region) that can be established by the preanalyzed gas mixtures. Breakdown of the conductivity cell was observed when measurements were made at temperatures higher than 1100°C; this breakdown was exhibited by a dramatic increase in the cell resistance readings. After completing the measurements at 1100°C, repeated readings at lower temperatures were not reproducible. Visual analysis of the pellet revealed the presence of cracks and a change in the color of the pellet from the original azure blue to black. X-ray diffraction analysis of the pellet indicated lines of Ni, Al_2O_3, NiO and $NiAl_2O_4$. The x-ray diffraction results suggest that partial reduction of the spinel pellet as represented by the reaction,

$$NiAl_2O_4 = Ni + 1/2O_2 + Al_2O_3 \qquad (53)$$

occurred during measurements in the metastable region with the reduced Ni and Al_2O_3 randomly distributed in the spinel matrix. Reoxidation of the reduced Ni into NiO and reaction of the NiO with Al_2O_3 may not be complete since a high temperature of about 1300° to 1400°C is required for complete formation of $NiAl_2O_4$ [112,113] from the component oxides; the remaining unreduced spinel matrix can provide

mechanical hindrance to the reaction of NiO with Al_2O_3 [111]. As shown in Fig. 9 and 14, resistance readings were obtained even in the metastable region - this undoubtedly is due to the slow decomposition of $NiAl_2O_4$.

In tests conducted with reversible electrodes to fix the oxygen activity of the cell, color change from the original azure blue to black was observed in the spinel pellets measured in the metastable region. In the tests conducted within the thermodynamic stability region of $NiAl_2O_4$, no color change in the pellets was observed. Repeated measurements in the stable region gave reproducible results.

The conductivity isotherms shown in Fig. 9, 12, 13 and 14 can be analyzed in terms of defect reactions that occur in the spinel as given by eq. 20 to 37 (pp. 34 and 35). For the cations Ni^{2+} and Al^{3+}, the probable defect reactions at high oxygen partial pressures are,

$$1/2O_2(g) = O_O + V''_{Ni} + 2h^\circ \qquad (61)$$

$$[V''_{Ni}]p^2 = K_1P(O_2)^{1/2} \qquad (62)$$

$$3/4O_2(g) = 3/2O_O + V'''_{Al} + 3h^\circ \qquad (63)$$

$$[V'''_{Al}]p^3 = K_2P(O_2)^{3/4} \qquad (64)$$

At low oxygen partial pressures, the defect reaction is,

$$O_O = V_O^{\cdot\cdot} + 1/2O_2(g) + 2e' \qquad (28)$$

$$[V_O^{\cdot\cdot}]n^2 = K_B\ P(O_2)^{-1/2} \qquad (29)$$

The electroneutrality conditions are,

$$2[V''_{Ni}] + n = 2[V_O^{\cdot\cdot}] + p \quad (65)$$

$$3[V'''_{Al}] + n = 2[V_O^{\cdot\cdot}] + p \quad (66)$$

For situations where $2[V''_{Ni}] >> n$, $3[V'''_{Al}] >> n$ and $p >> 2[V_O^{\cdot\cdot}]$,

$$2[V''_{Ni}] = p_1 \quad (67)$$

$$3[V'''_{Al}] = p_2 \quad (68)$$

Eq. 62 and 64 become,

$$4[V''_{Ni}]^3 = p_1^3/2 = K_1 P(O_2)^{1/2} \quad (69)$$

$$2[V''_{Ni}] = p_1 = K'_1 P(O_2)^{1/4} \quad (70)$$

$$p_1 \propto P(O_2)^{1/4} \quad (71)$$

$$27[V'''_{Al}]^4 = p_2^4/3 = K_2 P(O_2)^{3/4} \quad (72)$$

$$3[V'''_{Al}] = p_2 = K'_2 P(O_2)^{3/16} \quad (73)$$

$$p_2 \propto P(O_2)^{3/16} \quad (74)$$

Since $np = K_i$,

$$n_1 \propto P(O_2)^{-1/4} \quad (75)$$

$$n_2 \propto P(O_2)^{-3/16} \quad (76)$$

For Ni vacancies, $K_S = [V_O^{\cdot\cdot}][V''_{Ni}]$,

$$[V_O^{\cdot\cdot}] \propto P(O_2)^{-1/4} \quad (77)$$

For Al vacancies, $K'_S = [V_O^{\cdot\cdot}]^3[V'''_{Al}]^2$,

$$[V_O^{\cdot\cdot}] \propto P(O_2)^{-1/4} \quad (78)$$

For conditions where $[V''_{Ni}]$ and $[V'''_{Al}]$ are large, eq. 71 and 74 become,

$$p_1 \propto P(O_2)^{1/4} \quad (79)$$

$$p_2 \propto P(O_2)^{1/4} \quad (80)$$

$$n_1 \propto P(O_2)^{-1/4} \quad (81)$$

$$n_2 \propto P(O_2)^{-1/4} \quad (82)$$

Applying the above defect reactions to the experimental results, it can be seen that in Fig. 9, the conductivity isotherms at 800° and 900°C indicate conductivities that are independent of oxygen partial pressure - this could be due to the presence of a significant concentration of defects such as cation vacancies. However, at 1000° and 1100°C, p-type conductivities are present at $P(O_2) > 10^{-4}$ atm. A plot of the p-type conductivity vs log $P(O_2)$ in Fig. 10 reveals slopes of 1/6.3 at 1000°C and 1/6.7 at 1100°C; these results suggest a p-type conductivity that is proportional to $P(O_2)'^{/4}$ as given by eq. 71. Verification of the $P(O_2)'^{/4}$ dependence was made by plotting σ vs $P(O_2)'^{/4}$ (Fig.11) and with the use of linear regression analysis, the calculated intercepts at $P(O_2)'^{/4}=0$ are in good agreement with the ionic conductivities at 1000° and 1100°C (Fig. 9). The p-type conductivity at $P(O_2) > 10^{-4}$ atm may be attributed to the presence of NiO in the spinel matrix. NiO has been found to exhibit a p-type conductivity that is proportional to $P(O_2)'^{/4}$ [179,197,198,200].

Conductivity isotherms shown in Fig. 9 and 12 to 14 indicate conductivities which are independent of oxygen partial pressure. Arrhenius plots of the ionic conductivity data of Fig. 9 and 12 - 14 give activation energies of 28.7, 41.0, 41.8 and 40.9 kcal/mole, respectively (Fig. 15 - 18). Due to fewer experimental points (Fig. 15), a lower activation energy value was obtained from the data of Fig. 9. The last three activation energies (with an average

value of 41.2) can be considered as representative values for the $NiAl_2O_4$ material studied.

The activation energies for ionic conduction are close in magnitude to the activation energies for self-diffusion of Ni in $NiAl_2O_4$ - 53.3 [63] and 55 [61] kcal/mole. A difference of about 13 kcal/mole exists between the activation energies of self-diffusion and ionic conductivity; this difference can be attributed to the nature of the two processes. In the tracer self-diffusion process, there is a correlation between successive jumps of the "tagged" ion ; in electrical conduction process, there is no correlation between jump vector directions and movement of lattice defects is along the direction of the imposed electric field [201]. The closeness in magnitude of the two activation energies - tracer self-diffusion and electrical conduction - suggests that a common diffusion mechanism operates in the two processes. A single activation energy for ionic conduction over the the temperature range studied indicates that a single diffusion mechanism contributes to the conductivity values obtained. In addition, the experimental activation energies of conduction are close in magnitude to the activation energies - 20 to 40 kcal/mole - obtained by Snider [144] for ionic conduction in $NiAl_2O_4$.

The exact defect structure in $NiAl_2O_4$ cannot be ascertained due to the lack of self-diffusion data of Al^{3+} and O^{2-} ions in $NiAl_2O_4$. However, the type of defects

present in $NiAl_2O_4$ may be inferred from a comparative analysis of the experimental results and physical property data of $NiAl_2O_4$ with the available physical property data of other spinels and oxides.

The activation energies for Ni diffusion in $NiAl_2O_4$ - 53.3 and 55 kcal/mole - are close in magnitude to the activation energies for Ni diffusion in NiO - 43.5 to 60.8 kcal/mole [61,62,116,202]. Although the ionic radii of Ni^{2+} (0.72 Å) [199] and Co^{2+} (0.74 Å) [199,203] are very close, the activation energies for Ni diffusion in $NiAl_2O_4$ are smaller than but close in magnitude to the activation energy for self-diffusion of Co in the normal spinel $CoAl_2O_4$ - 85 kcal/mole [67].

Schmalzried [68,69] estimated the defect structure in $CoAl_2O_4$ from the self-diffusion coefficients of Co in CoO and Al_2O_3 and concluded that $CoAl_2O_4$ is a metal deficient oxide with Co^{2+} vacancies and Al^{3+} ions on interstitial sites or on regular sites of Co^{2+} ions as the major defects. CoO ,one of the component oxides of $CoAl_2O_4$, is also a metal deficient oxide like NiO with doubly charged vacancies as the predominant defects [180,204-206].

Greskovich and Schmalzried [207] measured the number of vacancies in $CoAl_2O_4$ (with 10 mole% excess of Al_2O_3) at 1100°-1150°C and in oxygen partial pressures of 2×10^{-1} to 10^{-4} atm; the concentration of cobalt vacancies at 1 atm O_2 is about 1.5×10^{-3}. Their results were consistent with the concept of doubly ionized cobalt vacancies and an equivalent

number of electron holes as given by the reaction,

$$1/2O_2 = O_O + V''_{Co} + 2h^\circ \qquad (83)$$

Electrical conductivity measurements made on $CoAl_2O_4$ at 1085°C by Schmalzried[149] indicate that at $P(O_2) < 10^{-8}$ atm, conductivity is independent of oxygen partial pressure. $CoAl_2O_4$ was observed to exhibit p-type conductivity at $P(O_2) > 10^{-8}$ atm.

Pettit et al.[103] investigated the rate of formation of $NiAl_2O_4$ by solid-state reaction; from an electron microprobe analysis of the concentration gradients of Ni and Al in a $NiAl_2O_4$ layer, Pettit et al.[103] concluded that Ni diffuses in $NiAl_2O_4$ by a vacancy mechanism. In addition, Stubican and Roy [91] studied the precipitation phenomena in the crystalline solubility of Al_2O_3 in MgO and reported that solubility is brought about by a diffusion controlled process involving cation vacancies. Interdiffusion studies on $MgO-Al_2O_3$ by Whitney and Subican[226] indicate that in the solid-state formation of the spinel the diffusion of Al^{3+} ions proceeds by a vacancy mechanism.

In line with the above information, the most probable defects contributing to self-diffusion and electrical conduction in $NiAl_2O_4$ are cation vacancies, V''_{Ni} and V'''_{Al}. Diffusion and electrical conduction via oxygen vacancies, $V^{\cdot\cdot}_O$, in $NiAl_2O_4$ is less likely. In the solid-state formation of spinels [82-109,111-115], movement of the large oxygen ions is minimal and counterdiffusion of cations through a relatively rigid oxygen ion framework is the

predominant mechanism. In addition, the self-diffusion coefficient of oxygen is smaller than that of aluminum in Al_2O_3. The activation energy for oxygen diffusion in Al_2O_3 (152 kcal/mole [80]) is larger than that for aluminum diffusion in the same material (114 kcal/mole [72]). The activation energy of oxygen ion mobility in Al_2O_3 (152 kcal/mole [80]) is much larger than that for oxygen ion mobility in cubic fluorite structure calcia-stabilized zirconia (31.2 kcal/mole) where diffusion is by oxygen vacancies [77]. In addition, cation diffusion has been found to exceed oxygen diffusion [208] in both Cr_2O_3 and Fe_2O_3, which have the same crystal structure as Al_2O_3. The oxygen diffusion coefficient is about an order of magnitude smaller than that of either Ni^{+2} or Cr^{+3} ion in the normal spinel $NiCr_2O_4$ [78].

Aluminum vacancies instead of aluminum interstitials are most likely to be present with nickel vacancies in $NiAl_2O_4$. Most thermoelectric power experiments [187-189] on Al_2O_3 indicate that the sign of the current carrier is negative in the temperature region of 1150° to 1500°K; the negative sign suggests aluminum vacancies. In addition, aluminum diffusion in Al_2O_3 is by a vacancy mechanism as proposed by Paladino and Kingery [72] and by Lackey [185].

The low ionic conductivity (10^{-3} $ohm^{-1}cm^{-1}$ at 1000°C) when compared to that of the fluorite structure calcia-stabilized zirconia (3×10^{-2} $ohm^{-1}cm^{-1}$ at 1000°C) [209] is due to the crystal structure of $NiAl_2O_4$. As

reported by Cooley and Reed [36], $NiAl_2O_4$ is almost 100% inverted at 600°C and about 74% inverted at 1391°C. The oxygen parameter u of $NiAl_2O_4$ is in the range of 0.381 [21] to 0.384 [36] - this indicates larger tetrahedral sites and smaller octahedral sites. In the spinel structure, there are fairly open channels for the diffusion of cations along the tetrahedral sites; however, diffusion along the octahedral sites is difficult due to greater displacement of oxygen ions and also greater repulsion from cations [108,115].

DC Polarization Measurements

To determine the partial conductivities in $NiAl_2O_4$, the dc polarization method was used. To check for any variation in partial conductivities with oxygen partial pressure, tests were conducted at $P(O_2) = 1.3 \times 10^{-4}$ atm (800° to 1400°C) and at $P(O_2) = 9.2 \times 10^{-14}$ (800°C) to 6.7×10^{-4} atm (1400°C). Current-applied potential plots are given in Fig. 19-25 and these plots show almost linear relationship between current and applied potential at temperatures of 800°-1400°C. No plateaus are present in the plots - this indicates that only p-type conductivity is present in the temperature and pressure range studied. With the use of eq. 41 (p. 39), the partial conductivity was estimated from the log (IFL/RT) vs E plots shown in Fig. 26 and 27. Following the approach of Ilschner [163] and Wagner and Wagner [165], the p-type conductivities (Table 8) were obtained from the intercepts at E=0 . Using the conductivity isotherms given in Fig. 14, the ionic transport number was calculated with

the use of eq. 21,

$$t_i = \sigma_i / \sigma \qquad (21)$$

and the results are plotted in Fig. 28. The ionic transport number decreases from 0.97 at 800°C to 0.63 at 1400°C. At constant temperature, the p-type conductivities are slightly smaller at lower oxygen partial pressure. Arrhenius plots of the p-type conductivity data are given in Fig. 29 and 30, and activation energies of 55 and 60 kcal/mole were obtained. These p-type conduction activation energies are quite large when compared to those reported for ZrO_2 (44.4 kcal/mole at 2 x 10^{-3} atm O_2) [210], Y_2O_3 (44.7 kcal/mole at 10^{-3} and 10^{-7} atm O_2) [211] and ThO_2 (40.4 kcal/mole at 10^{-4} atm O_2 [212]) - oxides which have the cubic fluorite structure. When compared to the ionic conductivities given in Fig. 14, the p-type conductivities are quite large and, if actually present during conductivity measurements, should be reflected according to the defect equilibria (eq. 71 and 74) on the isotherms of Fig. 12-14; however, this is not the case as the conductivities are independent of oxygen partial pressure.

The large value of the p-type conductivities may be due to the presence of gas phase conduction during measurement [213-219]. Peters et al. [213] demonstrated that for high resistance materials at high temperatures (>1100°C) the conductivity of the gas phase around the sample can be comparable to or greater than that of the sample. Loup and Anthony [214] found the same effect to be important above

1500°C. The process presumably involves thermionic emission from the sample, the supporting structure, or the lead wires, and its extent is probably greatly influenced by details and geometry of the conducting or testing apparatus [158,215]. Moulson and Popper [216] and Ozkan and Moulson [217] have found gas phase conduction important at relatively low temperatures. Dutt et al. [218,219] reported that at high temperatures (≥1620°C) the true bulk conductivity is 0.7 times the conductivity measured without eliminating surface and gas phase conduction; at lower temperatures, the surface and gas conductivities were found to be larger than the bulk conductivity. However, for two-probe ac conductivity measurements, Rapp [158]reported that reliable results can be obtained at temperatures up to 1400°C. The presence of gas phase conduction may be evident in the increase in the ionic transport number (Fig. 28) from about 0.59 (1573°K) to 0.63 (1673°K) in both gas mixtures.

Emf Measurements

Concentration cells (VII) and (VIII) (p. 53), similar to the one used by Fischer and Hoffmann [173], were employed to measure qualitatively the transport number of the conducting ion or ions in both spinels. For the spinel $NiAl_2O_4$, the results of the emf measurements are shown in Fig. 31. In the temperature range studied (800°-1400°C), positive emf values were obtained for the $NiAl_2O_4$ cell; the positive emf values suggest that the average value of $3t_{Ni^{2+}}$ is greater than the average value of $t_{Al^{3+}}$.

As for the relative mobilities of Ni^{2+} and Al^{3+} ions in $NiAl_2O_4$, it should be noted that the activation energy for Al diffusion in Al_2O_3 is twice that for Ni diffusion in $NiAl_2O_4$ (see Table 1). The self-diffusion coefficient of Al^{3+} (0.50 Å) in Al_2O_3 is several orders of magnitude smaller than that for Ni^{2+} (0.72 Å) in $NiAl_2O_4$. In addition, Pettit et al. [103] reported an activation energy of 115 kcal/mole for the kinetics of formation of $NiAl_2O_4$; this activation energy is close to the activation energy of 114 kcal/mole for Al self-diffusion in Al_2O_3 [72]. Macak and Koutsky [104] obtained an activation energy for the kinetics of $NiAl_2O_4$ formation of about 126 kcal/mole. Stone and Tilley [108] quoted activation energies of 88 and 103 kcal/mole for the solid-state formation of $ZnAl_2O_4$ and $NiAl_2O_4$, respectively. Navias [95] reported an activation energy of 100 kcal/mole for the formation of $MgAl_2O_4$. These activation energies of formation of aluminates are close in magnitude to that for Al diffusion in Al_2O_3 and suggest that the mobility of Ni^{2+} ions is greater than that of Al^{3+} ions. Furthermore, Pettit et al. [103] pointed out that the similarity in the activation energies for diffusion of Al in $NiAl_2O_4$ and in Al_2O_3 is due to the fact that the diffusion paths of an Al^{3+} ion in the two materials are essentially the same. Interdiffusion studies on the $NiO-Al_2O_3$ system by Minford and Stubican [106] indicate that in the formation of $NiAl_2O_4$, the diffusion of Al^{3+} ions controls the reaction rate.

As shown in Fig. 31 there is a decrease in the cell emf with increase in temperature; this decrease is probably due to an increased tendency toward disorder of cations on the excess cation lattice sites as the temperature level is increased, leading to an increasing fraction of individual ions contributing to conduction or diffusion in the spinel [78]. In addition, Pettit et al. [103] cited that at higher temperatures (≥1400°C) the diffusion of both Ni^{2+} and Al^{3+} affects the reaction rate of formation of $NiAl_2O_4$, indicating that at higher temperatures the relative mobilities of Ni^{2+} and Al^{3+} ions are close.

B. Manganese Aluminate

Before discussing the experimental results, a brief description of the physical property data of the component oxides of $MnAl_2O_4$ will be given.

MnO has the halite structure like NiO. The oxide at high temperatures exhibits an appreciable metal deficit ($Mn_{1-y}O$) and y can have values up to 0.15. MnO will be oxidized to higher oxides at 1 atm O_2 [153]. Nonstoichiometry studies on MnO have been made by Davies and Richardson [220] and Hed and Tannhauser [221,222]. Hed and Tannhauser [221] reported that the predominant defects are unassociated manganese vacancies, which are doubly charged. For small deviation and at intermediate pressures ($<10^{-7}$ atm O_2), the nonstoichiometry is approximately proportional to $P(O_2)^{1/6}$ and at higher pressures, the pressure dependence

may vary between $P(O_2)'^{/4}$ to $P(O_2)'^{/2}$. Unlike other oxides such as NiO, MnO exhibits p- and n-type conduction [220-222].

Electrical conductivity of MnO has been studied by Hed and Tannhauser [221] and O'Keeffe and Valigi [223]. Hed and Tannhauser [221] reported that at intermediate oxygen partial pressures,the p-type conduction is proportional to $P(O_2)'^{/4}$ and suggested doubly charged manganese vacancies as the major defect; an activation energy of 8.5 kcal/mole for hole mobility in MnO was obtained. O'Keeffe and Valigi [223] concluded in agreement with Hed and Tannhauser [221] that doubly charged manganese vacancies predominate at small deviations from stoichiometry; an activation energy of 11.7 kcal/mole for p-type conduction was reported.

Conductivity Measurements

Like $NiAl_2O_4$, the defect equilibria given by eq. 61-82 are applicable to $MnAl_2O_4$. The probable defect reaction in $MnAl_2O_4$ at high oxygen partial pressures for the cation Mn^{2+} is,

$$1/2O_2(g) = O_O + V''_{Mn} + 2h^{\circ} \quad (84)$$

$$[V''_{Mn}]p^2 = K_3P(O_2)'^{/2} \quad (85)$$

$$p_3 \propto P(O_2)'^{/4} \quad (86)$$

The defect reactions described for Al^{3+} and O^{2-} ions (eq. 28 and 63) are the same for $MnAl_2O_4$.

As for the experimental results, Fig. 32 and 36 represent the results of tests conducted using preanalyzed gas mixtures to establish the required oxygen partial

pressures; Fig. 40 is the result of the measurements employing reversible electrodes to fix the oxygen activity of the conductivity cell.

In Fig. 32, conductivity measurements were made close to the upper limit of thermodynamic stability (oxidizing) region (Table 4) but within the lower stability limit of $MnAl_2O_4$. Broken lines at the lower oxygen partial pressures describe the lower stability region. Resistance readings were obtained only up to 1000°C and breakdown of the spinel pellet was observed when measurements were made beyond 1000°C. The breakdown was manifested by a large increase in the resistance readings of the cell. Visual examination of the tested pellet revealed the presence of cracks and a change in the color of the pellet from the original brown to black. X-ray diffraction analysis of the tested pellet indicated the lines of Mn_3O_4, Al_2O_3 and $MnAl_2O_4$. Greenwald et al. [24] and Ivanov and Koroleva [110] have reported that annealing $MnAl_2O_4$ in weakly oxidizing and oxidizing atmospheres results in its conversion into Mn_3O_4 and Al_2O_3. The crystal structure of Mn_3O_4 or $MnMn_2O_4$ (a p-type conductor) [21] can be described as a tetragonally deformed spinel with an axial ratio of about 1.14 (a_o=8.14 Å, c=9.42 Å).

The formation of Mn_3O_4 within the cubic spinel matrix at high oxygen partial pressures could account for the presence of cracks in the pellet. From the conductivity isotherms of Fig. 32, p- and n-type conductivity isotherms

were determined and are shown in Fig. 33 and 34, respectively. In Fig. 33, slopes of 1/5.3, 1/5.7 and 1/5.9 were obtained, indicating a 1/6 oxygen partial pressure dependence of p-type conduction as given by eq. 86. In Fig. 34, the n-type conductivity isotherms show slopes of -1/5.8 and -1/6.7, suggesting a -1/6 pressure dependence of n-type conductivity as given by eq. 65. As a check, the ionic conductivities were estimated using linear regression analysis from the σ vs $P(O_2)'/'$ plot in Fig. 35; ionic conductivity values at $P(O_2)'/'=0$ are in good agreement with those in Fig. 32.

Fig. 36 gives the conductivity isotherms for the test run conducted within the stability limits, well below the calculated upper stability limit. Broken lines in the reducing atmosphere region indicate the lower metastable region of the spinel; broken lines at higher partial pressures indicate extrapolation of conductivity values to $P(O_2)= 1$ atm.

In Fig. 36, measurements only up to 1100°C were obtained. Cell breakdown was observed when measurements were made at temperatures higher than 1100°C; this breakdown was manifested by large increases in the cell resistance readings - a condition similar to that encountered with Sample D10 (Fig. 32). X-ray diffraction analysis of the tested spinel pellet revealed trace lines of Mn_3O_4. The cell breakdown is probably due to the formation of Mn_3O_4 in the weakly oxidizing region ($\cong 10^{-4}$ atm O_2) - an anomaly reported

by Coath and Dailly [145].

Using the data in Fig. 36, p-type conductivity isotherms (Fig. 37) give slopes of 1/7.2, 1/6.4, 1/6.2 and 1/5.8, indicating a 1/6 pressure dependence of p-type conduction in $MnAl_2O_4$ samples tested. N-type conductivity isotherms in Fig. 38 have slopes of -1/6.6, -1/6.3 and -1/5.9 which suggests a -1/6 pressure dependence of n-type conduction. Ionic conductivities obtained from the σ vs $P(O_2)'/'$ plot in Fig. 39 are in good agreement with the ionic conductivities shown in Fig. 36.

Conductivity results of the test runs employing reversible electrodes are shown in Fig. 40. Broken lines in the lower pressure region indicate the lower thermodynamic stability limit of $MnAl_2O_4$. As in Fig. 32 and 36, the ionic conductivity region occupies only 2 to 3 decades of partial pressure. P-type conductivity isotherms in Fig. 41 and 42 have slopes of 1/6.6 to 1/6.3, indicating p-type conduction that is proportional to $P(O_2)'/'$. N-type conductivity isotherms (Fig. 43) have slopes of -1/5.4 to -1/6.0, indicating a -1/6 pressure dependence of electron conductivity. Confirmation of the 1/6 pressure dependence of p-type conduction was made by estimating the ionic conductivities from the σ vs $P(O_2)'/'$ plots of Fig. 44 and 45 and good agreement was obtained between calculated and the observed values shown in Fig. 40.

From Arrhenius plots of the ionic conductivity (Fig. 46-48), activation energies of ionic conduction of 16.5,

26.6 and 31.1 kcal/mole were obtained from the data in Fig. 32, 36 and 40, respectively. Arrhenius plots of p-type conduction data from Fig. 33, 37, 41 and 42 give activation energies of 10.9 to 32.4 kcal/mole (Fig. 49-51). Activation energies of 33.6 to 52.4 kcal/mole were obtained from Arrhenius plots of n-type conductivity (Fig. 52 and 53). Since the results of Samples D10 and D2 (Fig. 32 and 36, respectively) were affected by the presence of Mn_3O_4, only the results of the test conducted using reversible electrodes (Fig. 40) can be considered representative of the $MnAl_2O_4$ pellets tested.

To date no data are available on the self-diffusion coefficients of Mn^{2+}, Al^{3+} and O^{2-} ions in $MnAl_2O_4$ and the exact defect structure of $MnAl_2O_4$ cannot be ascertained. A comparative analysis approach similar to that used on $NiAl_2O_4$ will be undertaken to estimate the probable major defects responsible for the conductivity values obtained.

$MnAl_2O_4$, $NiAl_2O_4$ and other aluminates have a common component oxide, Al_2O_3 which has a defect spinel structure in the γ-form [27-29,184,185]. Mn belongs to the transition metal group [203] and its ionic radius of 0.80 Å is close in size to the ionic radii of Ni^{2+} (0.72 Å) and Co^{2+} (0.74 Å) [174,199].

From the results given in Fig. 32-45, the $\pm 1/6$ oxygen partial pressure dependence of the conductivity values suggests doubly charged manganese vacancies as given by eq. 84. Measurement of the self-diffusion coefficient of Mn in

MnO by Price and Wagner [224] gave a ±1/6 oxygen partial pressure dependence and they concluded that doubly charged manganese vacancies are the major defects in MnO.

From the results of the test run conducted with reversible electrodes, Fig. 40-45, 51 and 53, the activation energies of 10.9 and 12.6 kcal/mole for p-type conduction in $MnAl_2O_4$ are close in magnitude to the activation energy of 8.5 kcal/mole for hole mobility in MnO measured by Hed and Tannhauser [221,222]. The activation energies of 50.9 and 52.4 kcal/mole for n-type conduction in $MnAl_2O_4$ are also close in value with the activation energy of 51.7 kcal/mole for electron mobility in MnO determined by Price and Wagner [224].

From Fig. 48, the activation energy of 31.1 kcal/mole for ionic conductivity in $MnAl_2O_4$ is smaller than that (41.2 kcal/mole) for ionic conduction in $NiAl_2O_4$. In addition, the activation energy of ionic conductivity in $MnAl_2O_4$ is smaller than the activation energies of 53.3 and 55.0 kcal/mole [61,63] for Ni diffusion in $NiAl_2O_4$. Furthermore the ionic conductivity of $MnAl_2O_4$(6.3×10^{-5} $ohm^{-1}cm^{-1}$ at 1000°C) is larger than that (10^{-5} ohm^{-1} cm^{-1} at 1000°C) of $NiAl_2O_4$. The difference in the activation energies of ionic conduction between $MnAl_2O_4$ and $NiAl_2O_4$ is due to their different in cation arrangements. $MnAl_2O_4$ has a normal spinel cation arrangement [21,24,41] while $NiAl_2O_4$ has an inverse spinel arrangement [21,24-27,34-36]. As pointed out by Stone and Tilley [108,115], cation diffusion along

octahedral sites is relatively more difficult than cation mobility along tetrahedral sites.

The ionic conductivity of $MnAl_2O_4$ (6.3×10^{-3} $ohm^{-1}cm^{-1}$ at 1000°C) is several orders of magnitude smaller than the ionic conductivities of the cubic fluorite structure ZrO_2-15% CaO (1.9×10^{-2} $ohm^{-1}cm^{-1}$ at 1000°C) [228] and ThO_2- 8%Y_2O_3 (2.3×10^{-3} $ohm^{-1}cm^{-1}$ at 1000°C) [229].

Since $MnAl_2O_4$ is an aluminate like $NiAl_2O_4$, the most probable major defects are manganese vacancies, V''_{Mn} and aluminum vacancies, V'''_{Al}.

DC Polarization Measurements

Polarization measurements were conducted at temperatures of 800° to 1200°C and at oxygen partial pressures close to the ionic conductivity regions of $MnAl_2O_4$ as shown in Fig. 40. The required oxygen partial pressures were established with preanalyzed CO-CO_2 gas mixtures.

Current-applied potential plots in Fig. 54-58 show almost linear relationships similar to those observed for $NiAl_2O_4$, Fig. 19-25. The absence of plateaus in any of the current-applied potential curves indicate that only p-type conductivities are present.

P-type conductivities were calculated from the log (IFL/RT) vs E plots shown in Fig. 59 and 60. The intercepts at E=0 are the values of the p-type conductivities (Table 13). Using these p-type conductivities, the ionic transport number was calculated and the results are shown in Fig. 61. As expected the ionic transport numbers at lower oxygen

partial pressures are slightly smaller. The ionic transport number decreases from 0.99 at 1073°K to 0.89 at 1473°K. Compared with $NiAl_2O_4$, the incremental decrease in ionic transport number with increase in temperature of $MnAl_2O_4$ is smaller - this is due to its cation arrangement as stated earlier.

Arrhenius plots of the partial conductivities (Fig. 62 and 63) give activation energies of 59.0 and 56.9 kcal/mole;as with $NiAl_2O_4$, these large values suggest the possible presence of gas phase conduction during measurement.

Emf Measurements

A concentration cell similar to the one used by Fischer and Hoffmann [173] was employed to determine the relative transport numbers of the conducting ions in $MnAl_2O_4$. As shown in Fig. 64, negative emf values were observed at temperatures between 800° and 1050°C; positive emf values at temperatures between 1050° and 1400°C were obtained. Negative emf values at 800°C≤T≤1050°C suggest that the average value of $3t_{Mn}{}^{2+} < t_{Al}{}^{3+}$; positive emf values at 1050°C≤T≤1400°C indicate that the average value of $3t_{Mn}{}^{2+} > t_{Al}{}^{3+}$.

As for the relative mobilities of cations in $MnAl_2O_4$ at high temperatures, it is probable that Mn^{2+} ions diffuse faster than Al^{3+} ions due to their positions in the spinel structure. From interdiffusion studies on the $MgO-Al_2O_3$ system, Whitney and Stubican [226,227] reported that the

diffusion of Al^{3+} ions controls the rate of formation of $MgAl_2O_4$, a normal spinel and Al^{3+} ions diffuse via a vacancy mechanism. In the interdiffusion studies of other normal spinels, $MgCr_2O_4$ [225] and $NiCr_2O_4$ [88], diffusion of the trivalent ion Cr^{3+} is rate controlling.

Conclusions

There is a difference in the ionic conductivity of a normal spinel $MnAl_2O_4$ and an inverse spinel $NiAl_2O_4$. The ionic conductivity of $MnAl_2O_4$ has been found to be larger than that of $NiAl_2O_4$ in the temperature range studied. The activation energy of ionic conduction of $MnAl_2O_4$ is about 10 kcal/mole smaller than that of $NiAl_2O_4$ - a result reflecting the difference in the cation arrangement between the two spinels.

$NiAl_2O_4$ has been observed to exhibit conductivity independent of oxygen partial pressure (from 1 to 10^{-13} atm at 1000°C). Although it is highly stable in air, $NiAl_2O_4$ has been found to be unstable in reducing atmospheres. Compared to $MnAl_2O_4$, $NiAl_2O_4$ has a wider ionic conduction region in the temperature and oxygen partial pressure range studied.

$MnAl_2O_4$ has been found to exhibit p- and n-type conductivity and it has an ionic conduction region covering about 2 to 3 decades of oxygen partial pressure. Compared to $NiAl_2O_4$, $MnAl_2O_4$ is much more stable in reducing atmospheres but highly unstable in weakly oxidizing and oxidizing atmospheres.

For both spinels, cation vacancies are the most probable major defects responsible for ionic conduction.

Figures

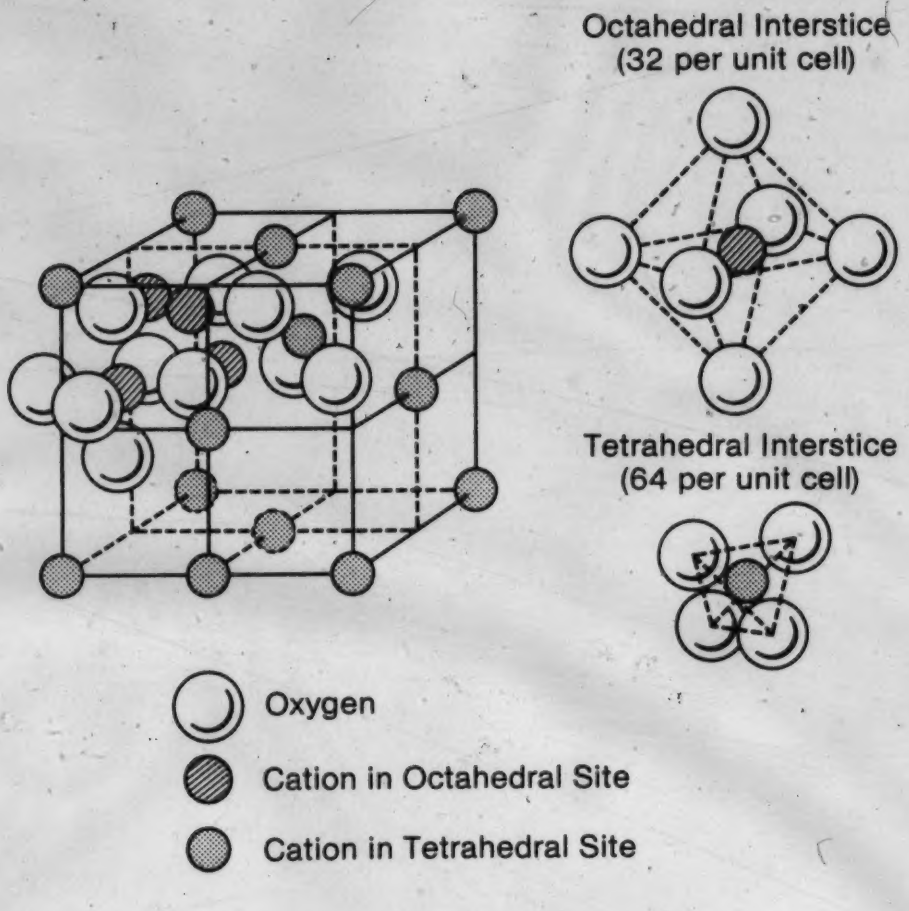

Figure 1. Spinel Structure

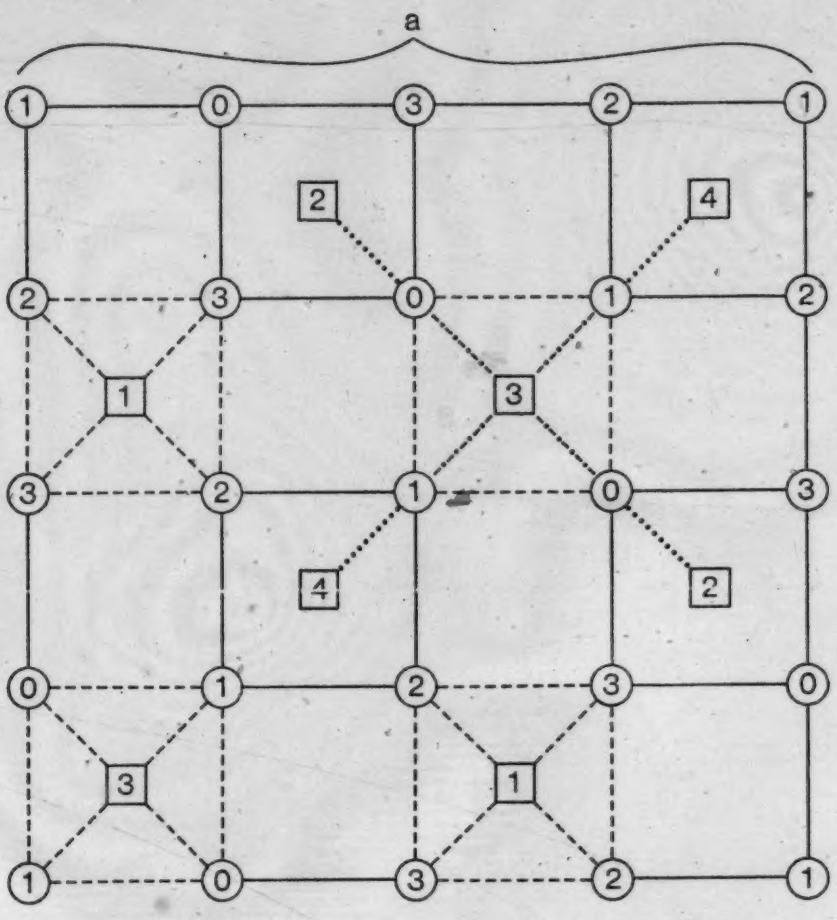

Figure 2. Projection of occupied spinel sites on the (001) plane.

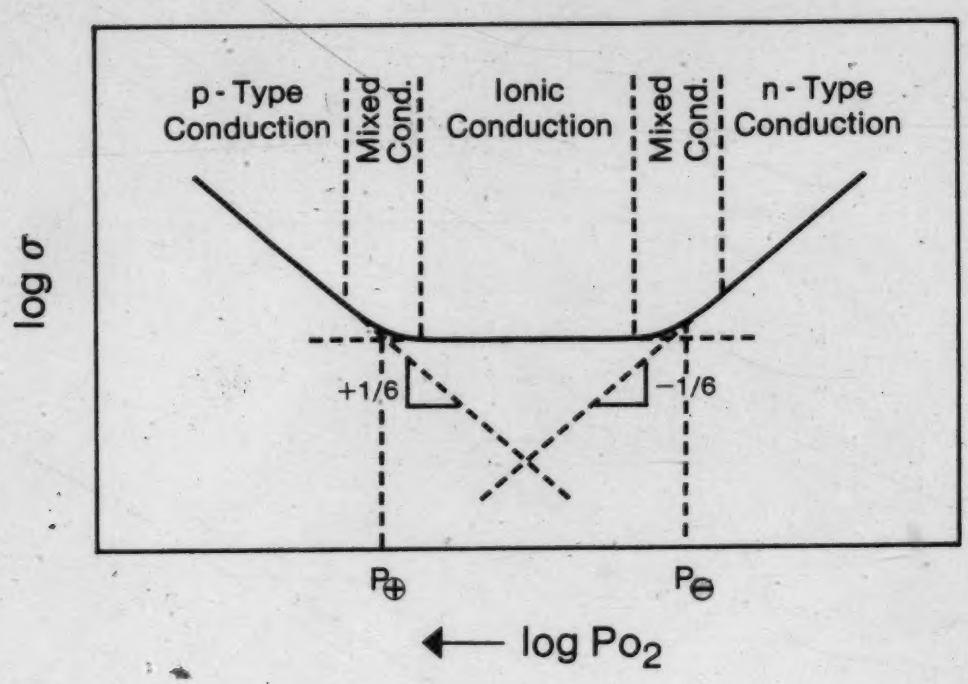

Figure 3. Schematic representation of partial ionic and electronic conductivities.

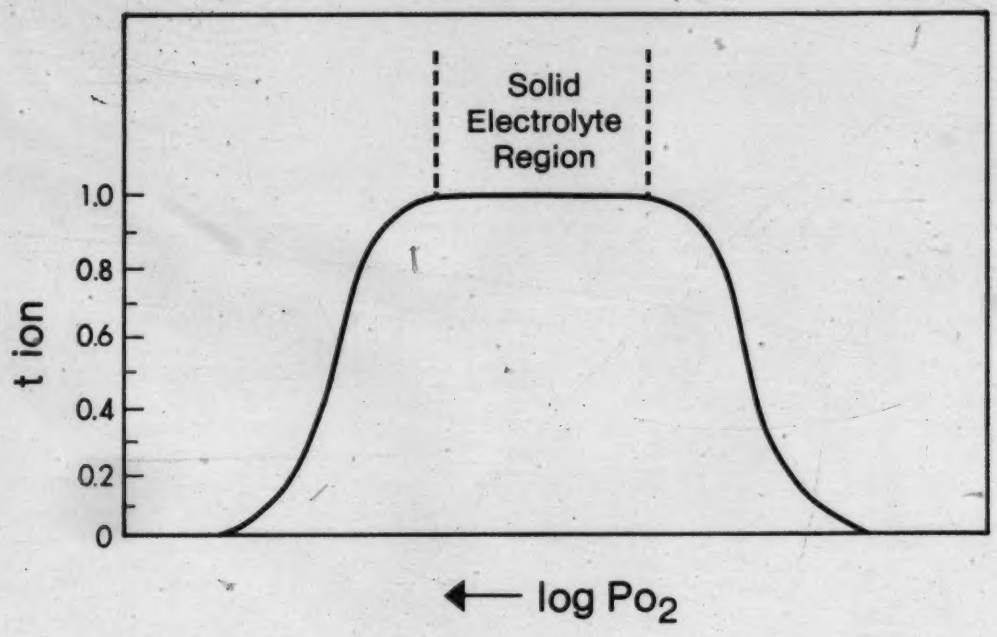

Figure 4. Schematic representation of the electrolytic region where $t_{ion} > 0.99$.

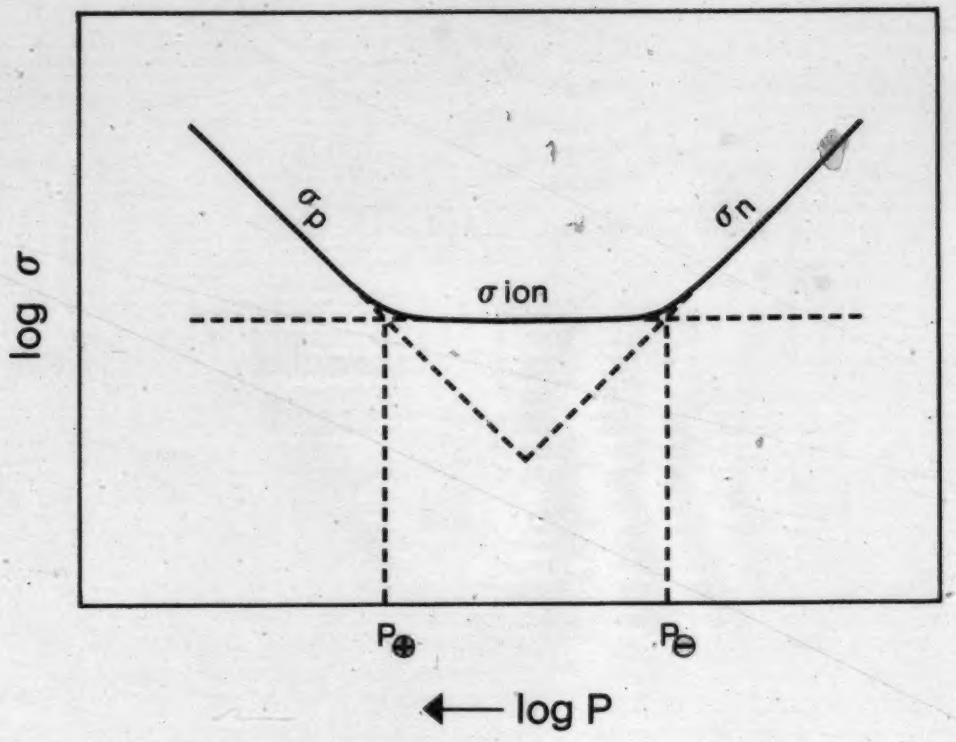

Figure 5. Partial conductivities as a function of oxygen partial pressure.

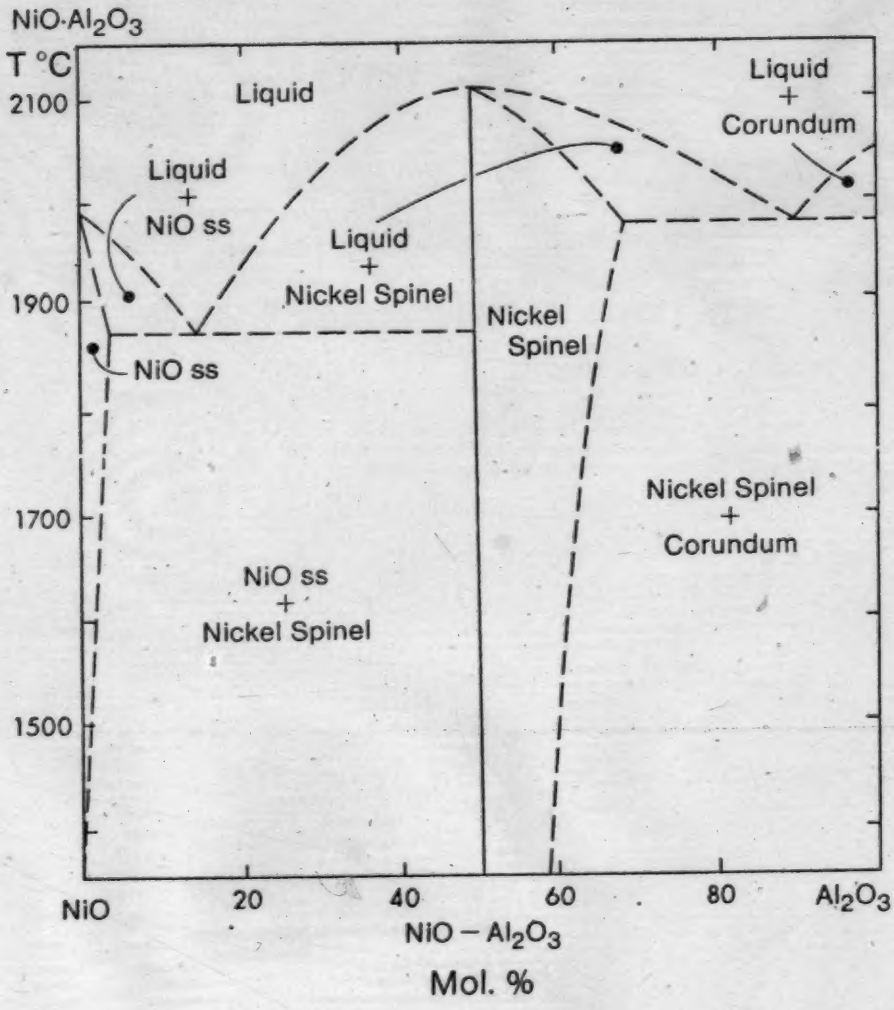

Figure 6. NiO-Al$_2$O$_3$ system.

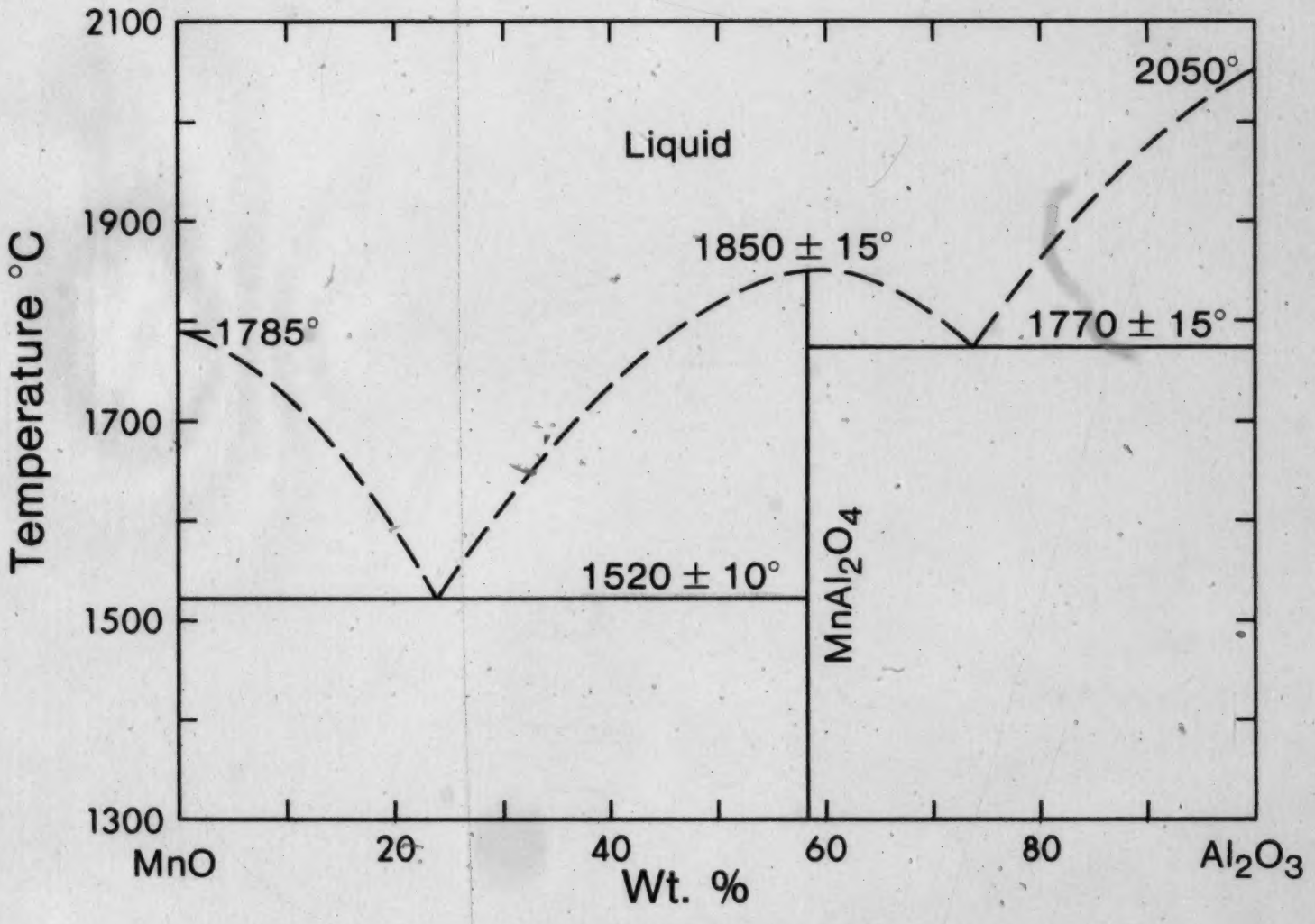

Figure 7. $MnO-Al_2O_3$ system.

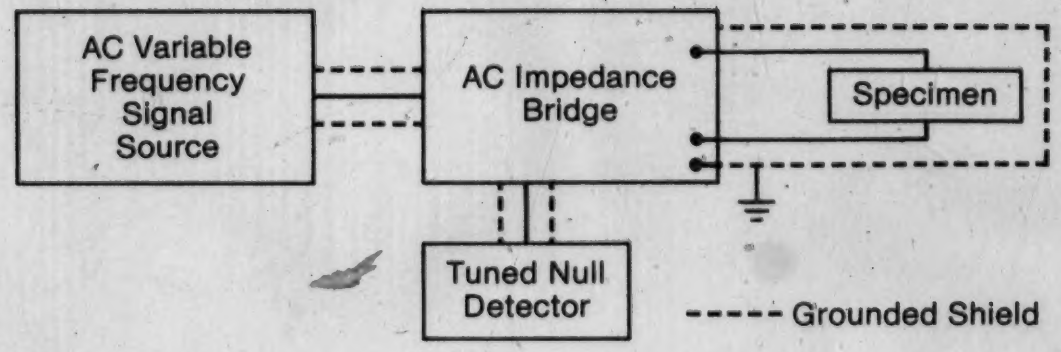

Figure 8. Circuit used to measure the two-probe ac electrical conductivity.

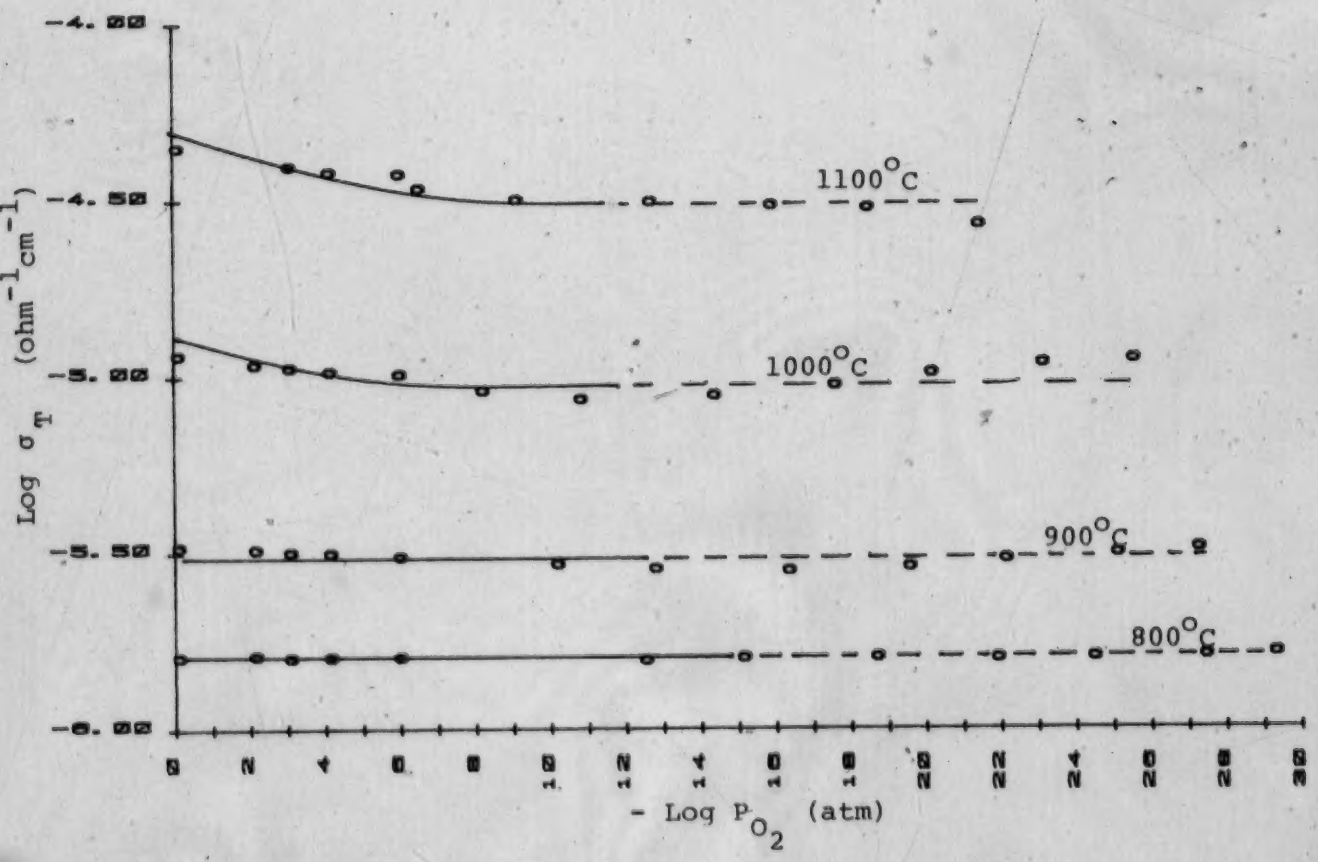

Figure 9. Conductivity isotherms for $NiAl_2O_4$ (Sample B4).

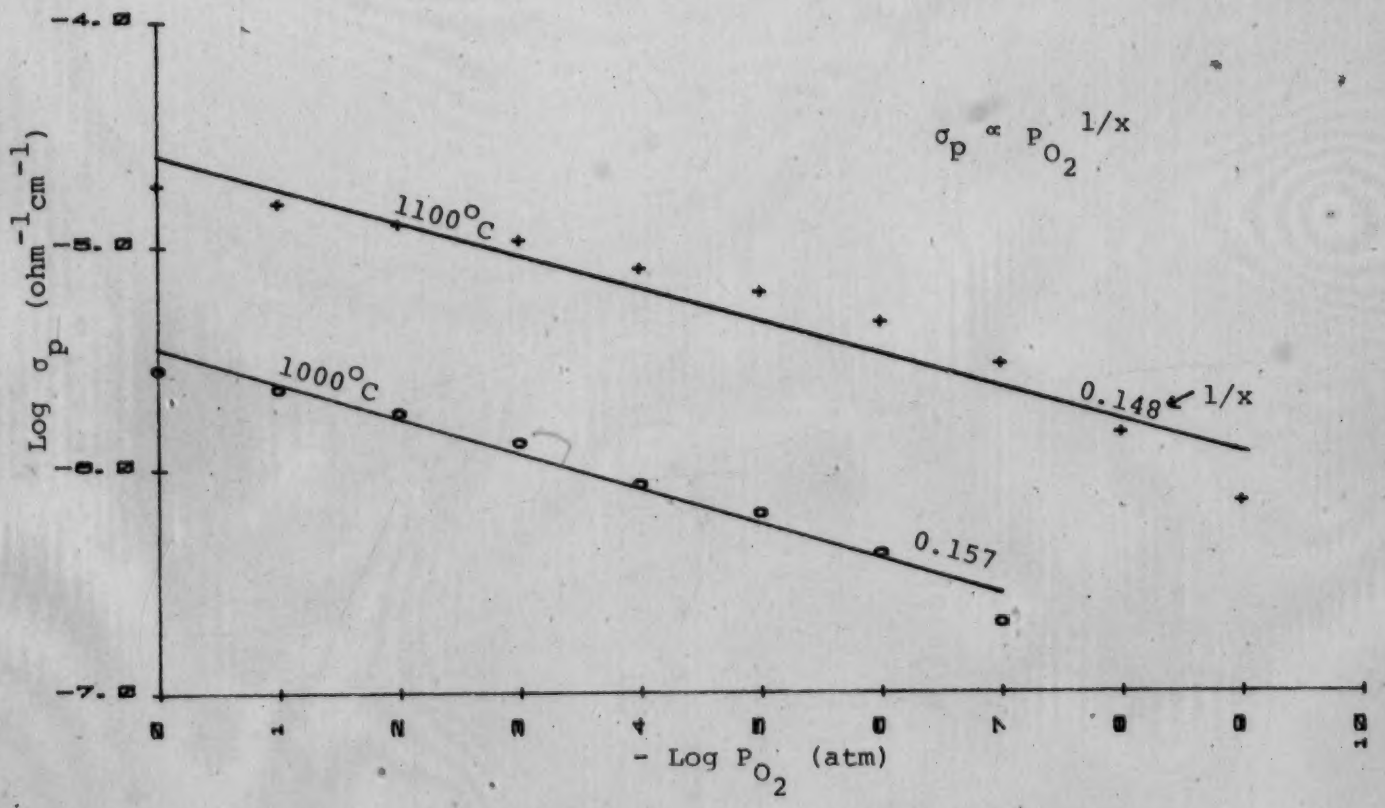

Figure 10. P-type conductivity isotherms for $NiAl_2O_4$ (Sample B4).

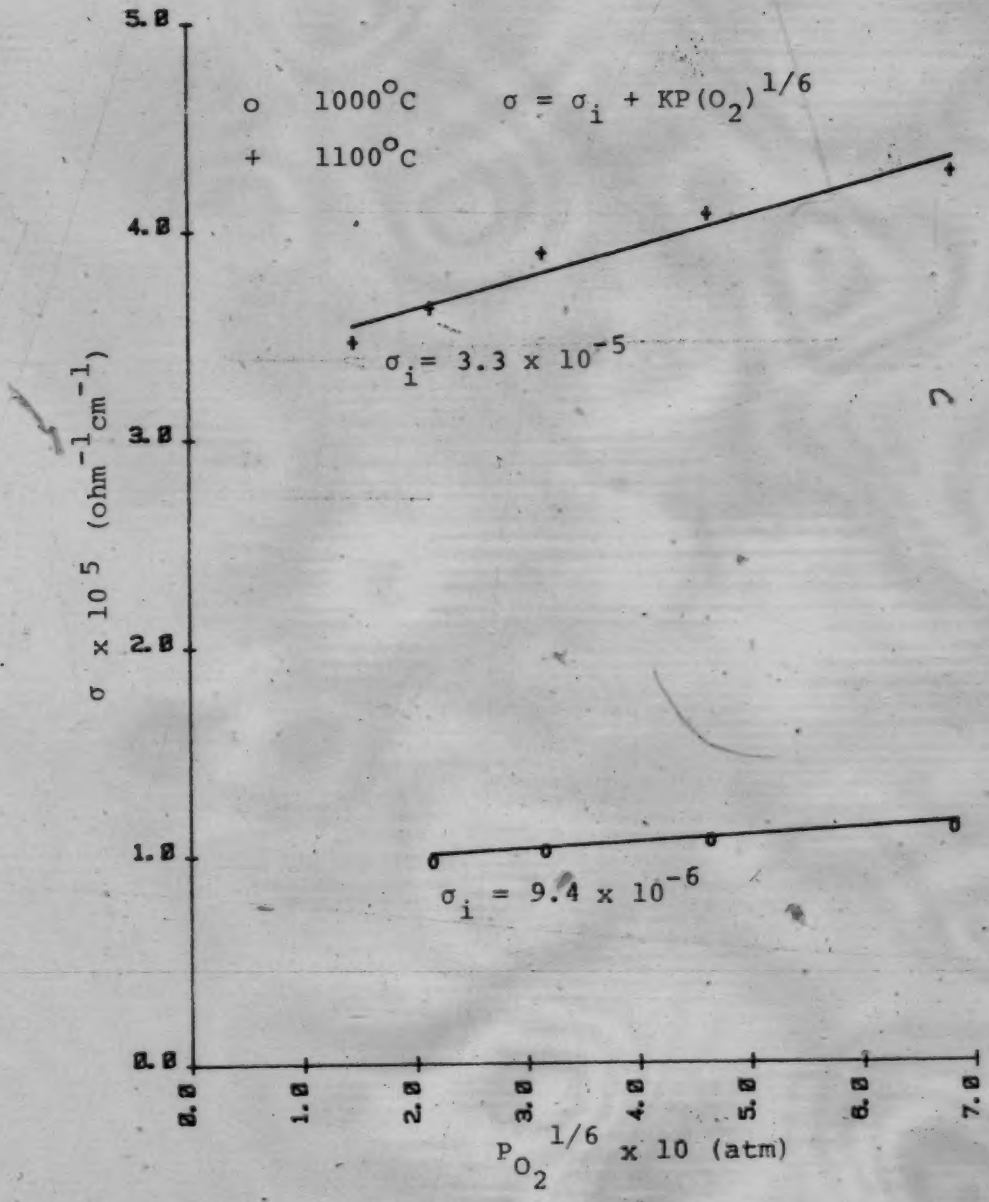

Figure 11. Determination of the ionic conductivity of $NiAl_2O_4$ (Sample B4).

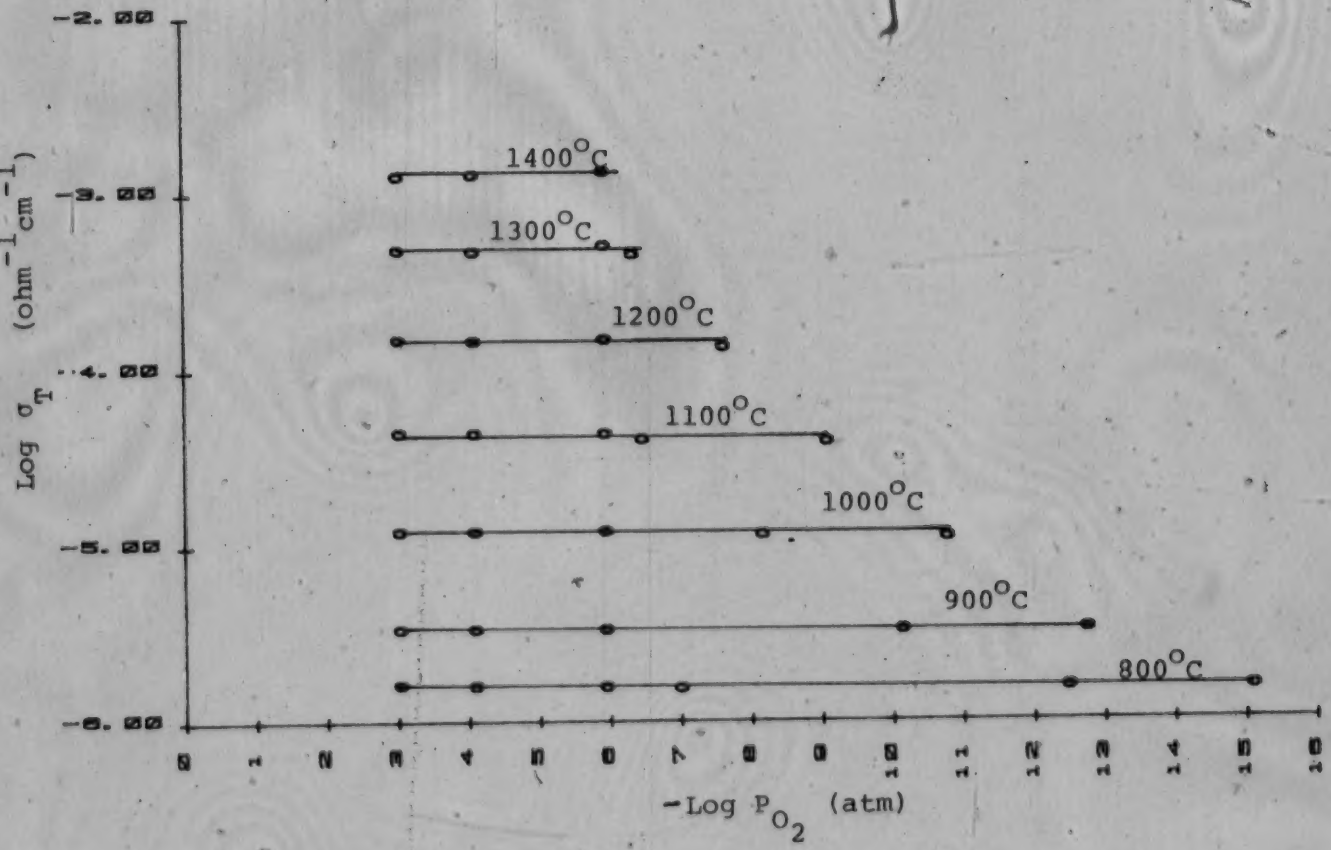

Figure 12. Conductivity isotherms for $NiAl_2O_4$ (Sample B2).

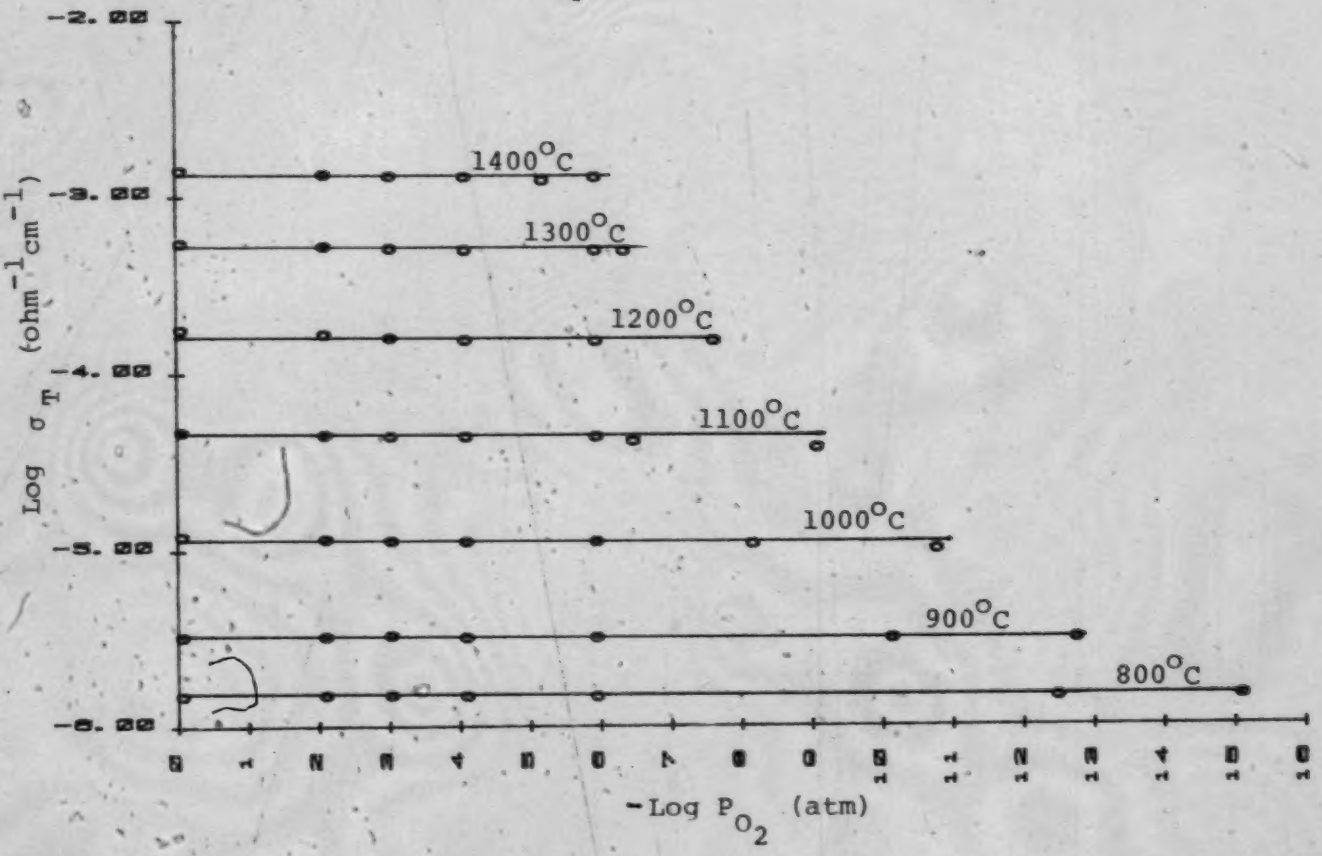

Figure 13. Conductivity isotherms for $NiAl_2O_4$ (Sample B6).

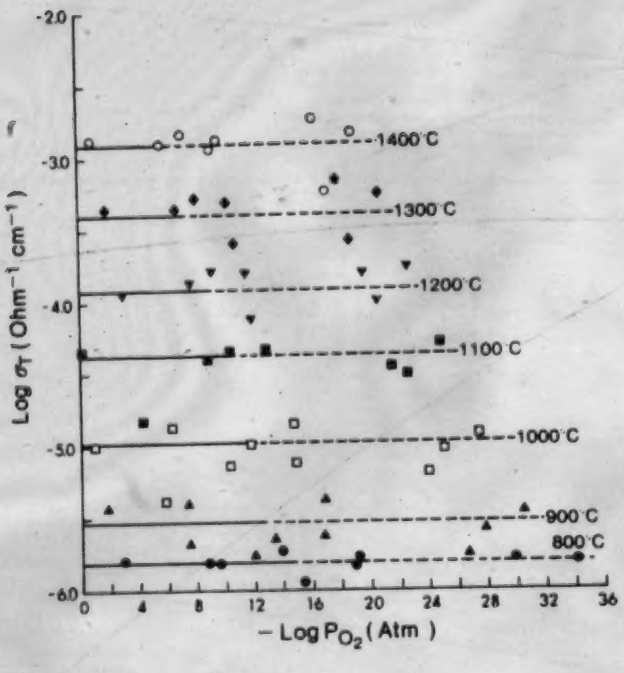

Figure 14. Conductivity isotherms for $NiAl_2O_4$ (Reversible Electrodes).

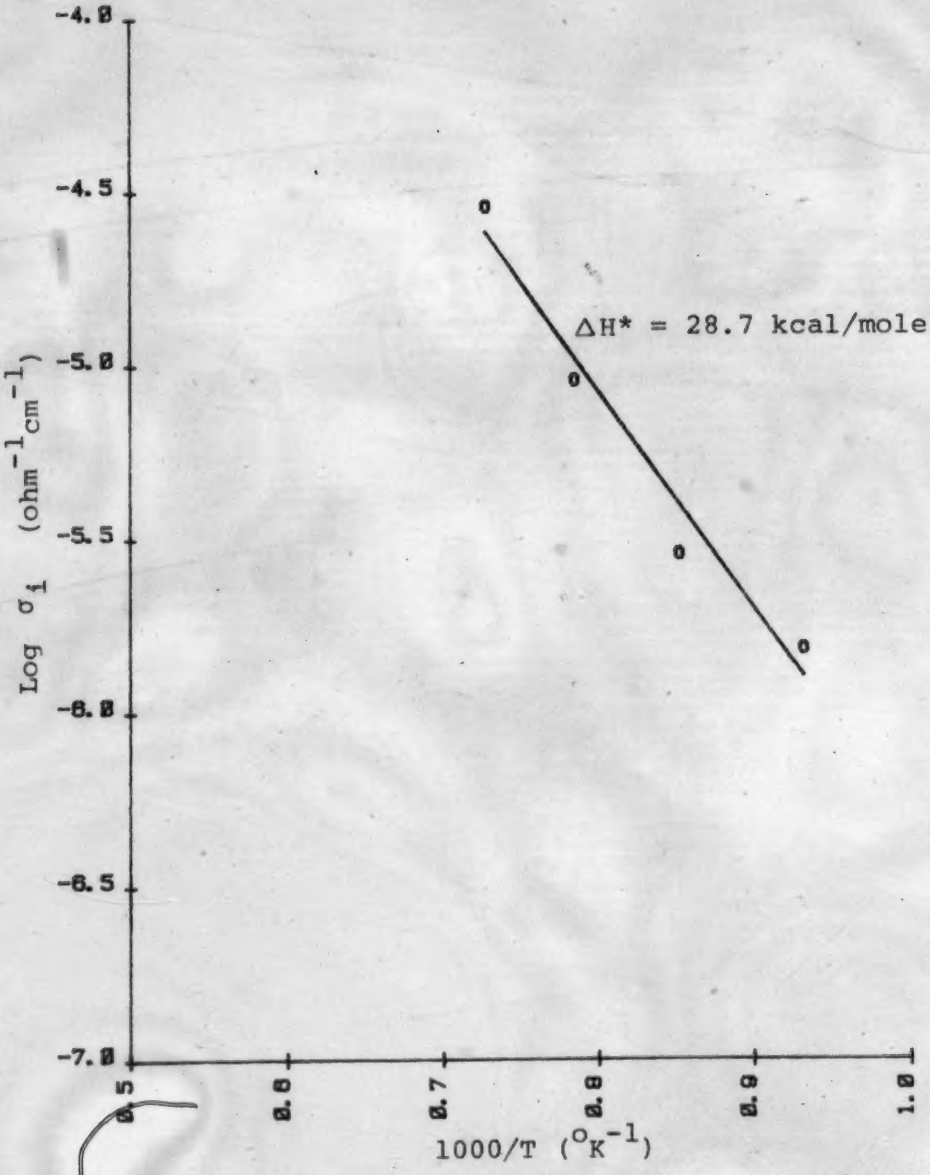

Figure 15. Arrhenius plot of the ionic conductivity of $NiAl_2O_4$ (Sample B4).

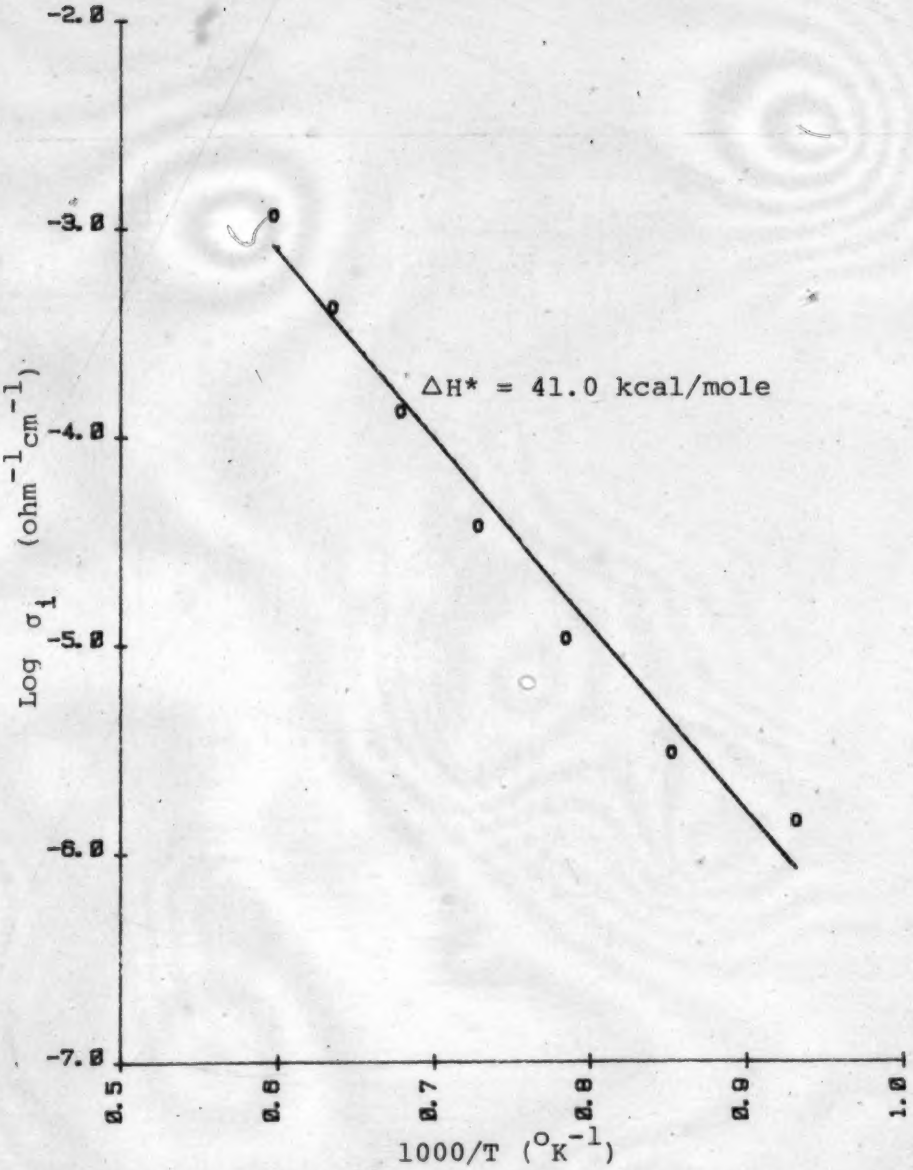

Figure 16. Arrhenius plot of the ionic conductivity of $NiAl_2O_4$ (Sample B2).

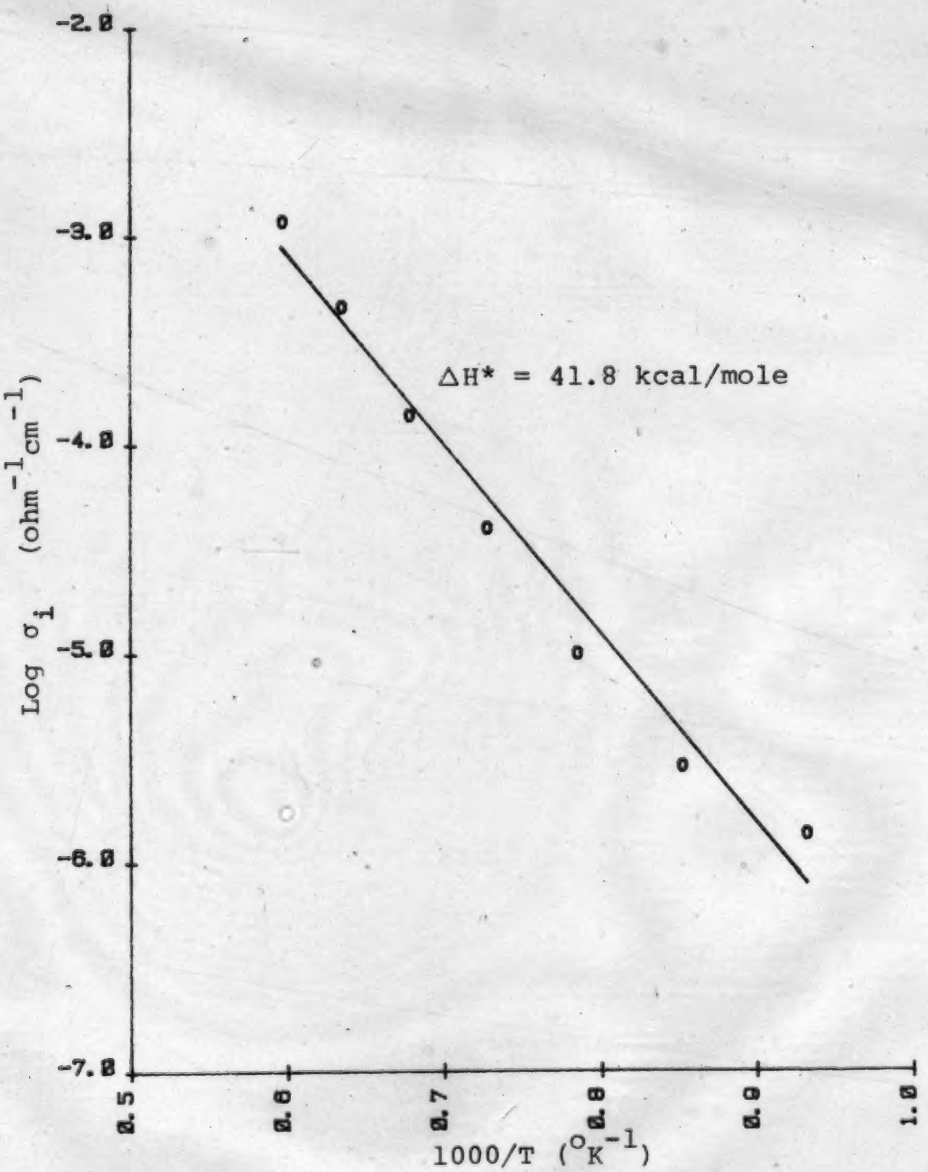

Figure 17. Arrhenius plot of the ionic conductivity of $NiAl_2O_4$ (Sample B6).

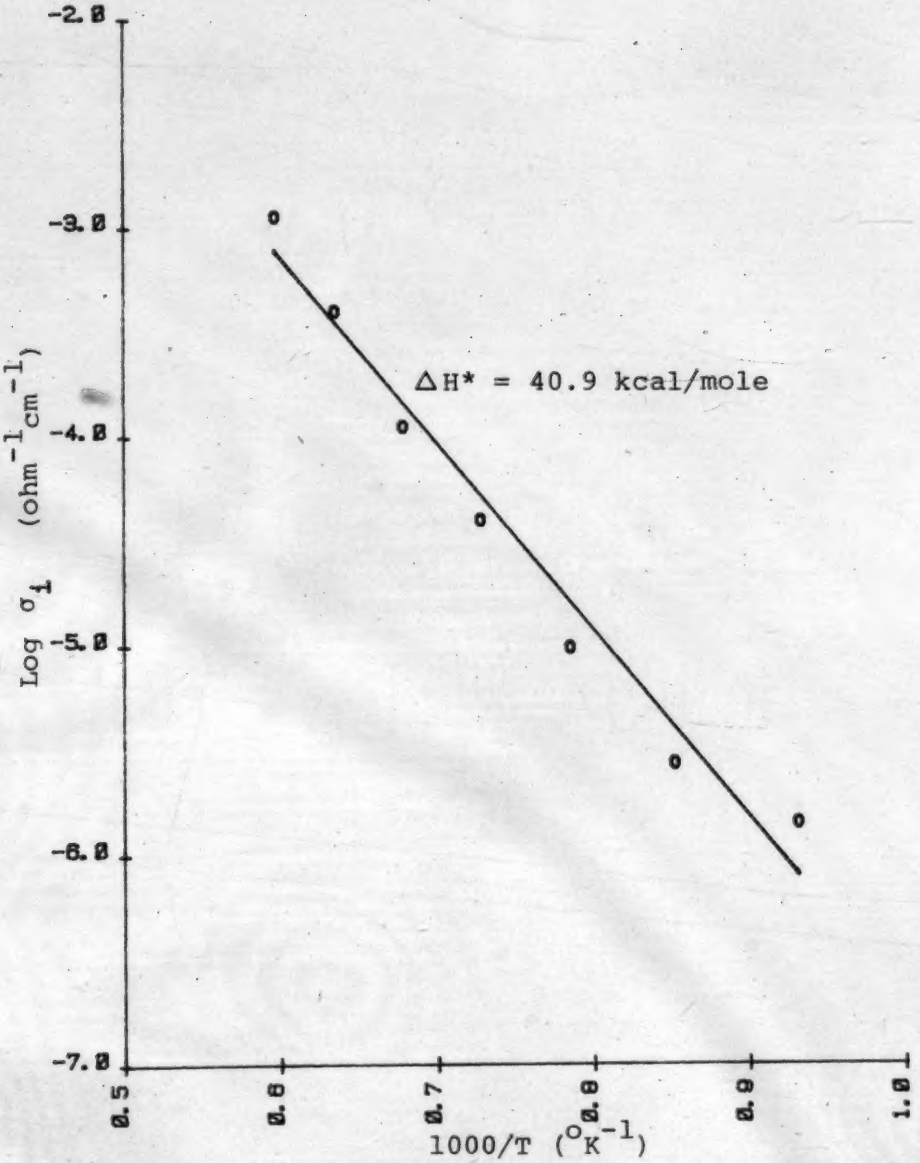

Figure 18. Arrhenius plot of the ionic conductivity of $NiAl_2O_4$ (Reversible Electrodes).

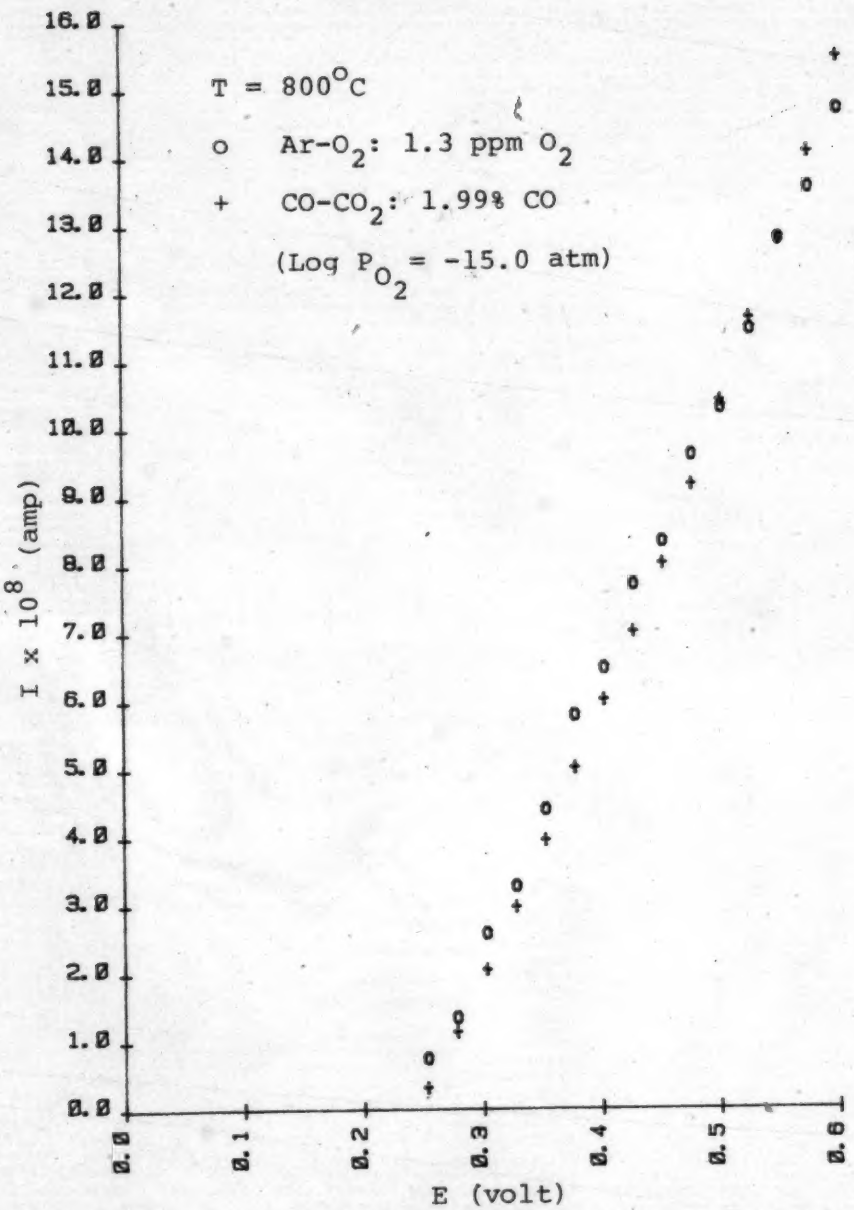

Figure 19. Current - applied potential curves for $NiAl_2O_4$ at 800°C.

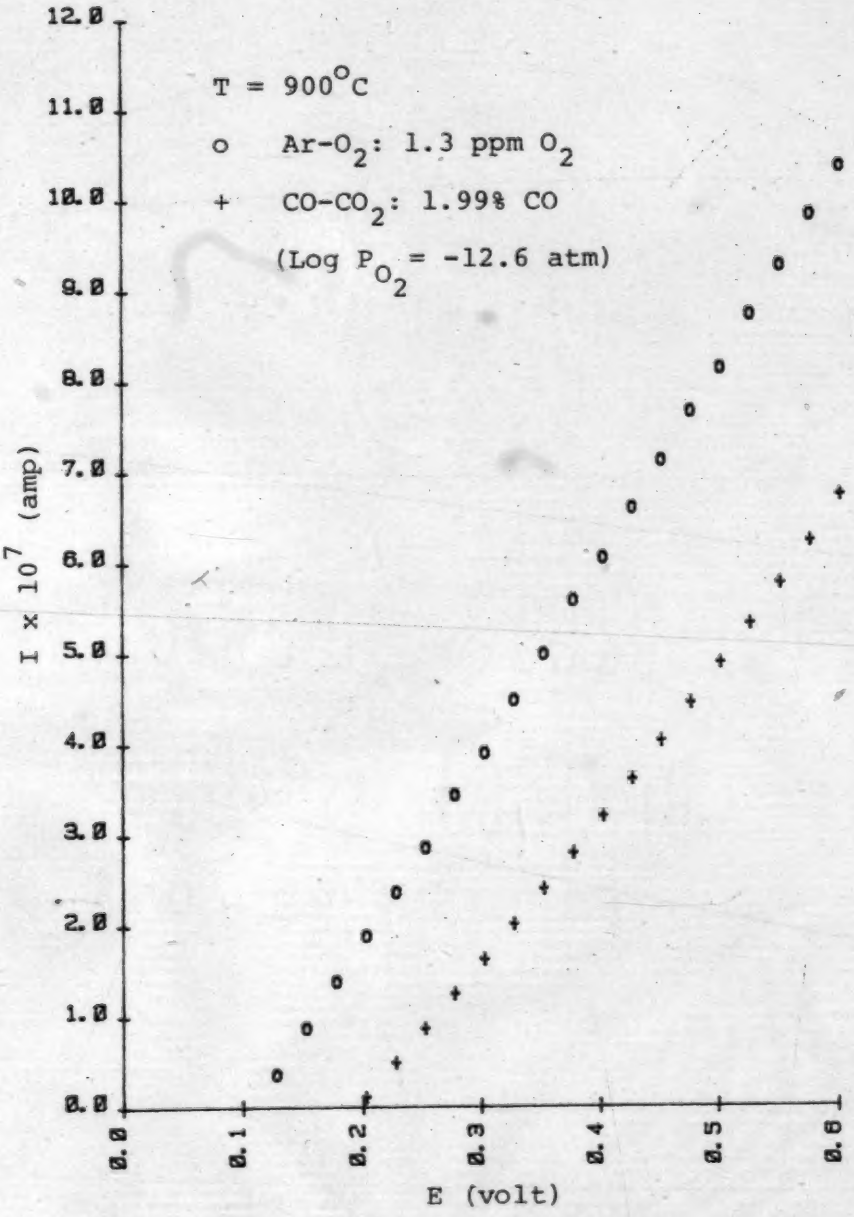

Figure 20. Current - applied potential curves for $NiAl_2O_4$ at 900°C.

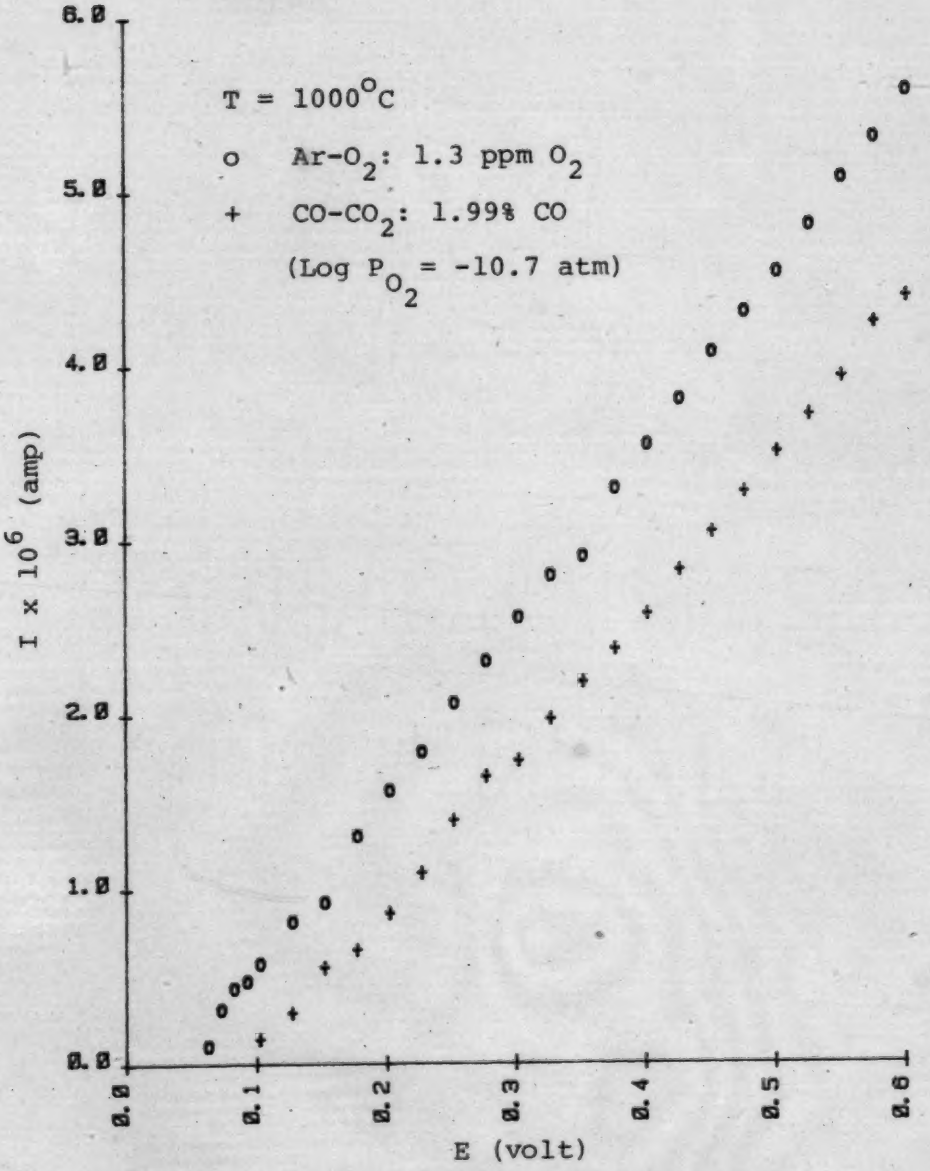

Figure 21. Current - applied potential curves for $NiAl_2O_4$ at 1000°C.

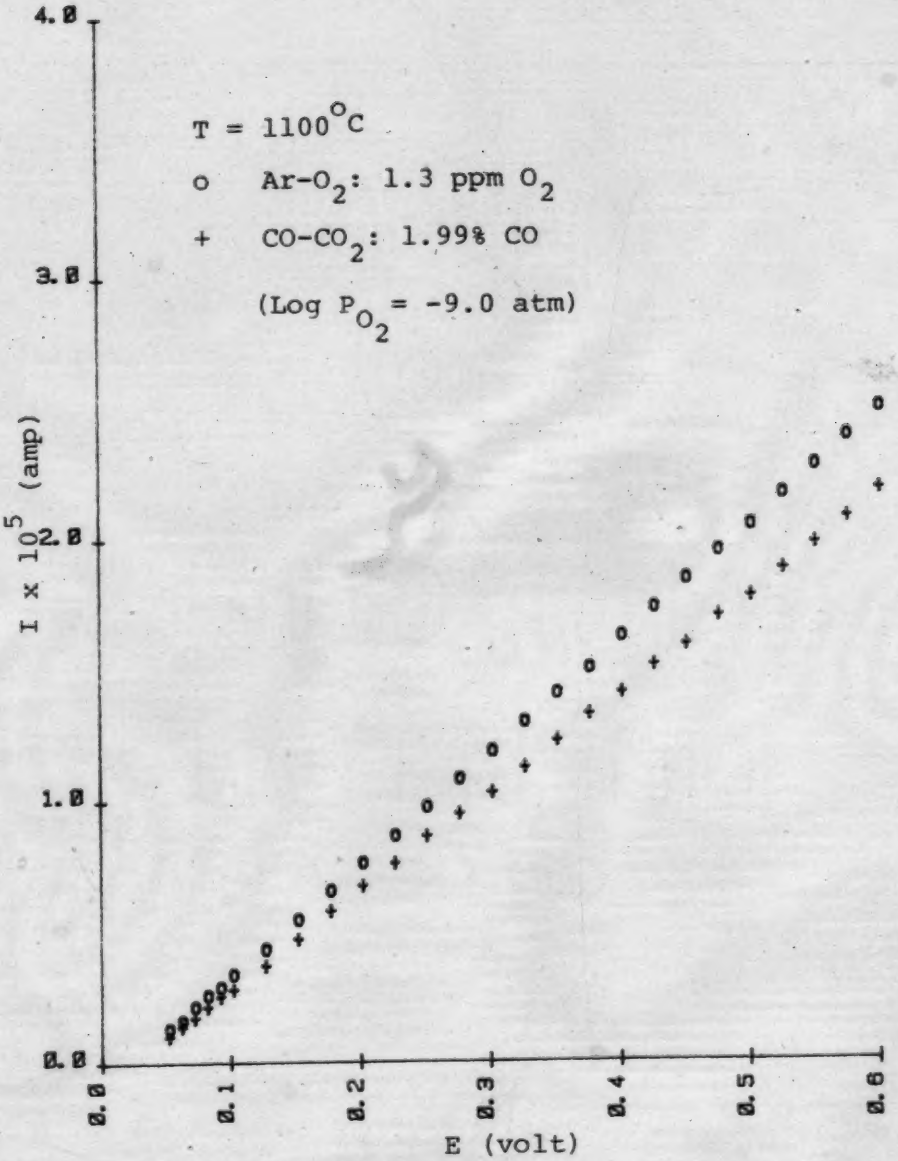

Figure 22. Current - applied potential curves for $NiAl_2O_4$ at 1100°C.

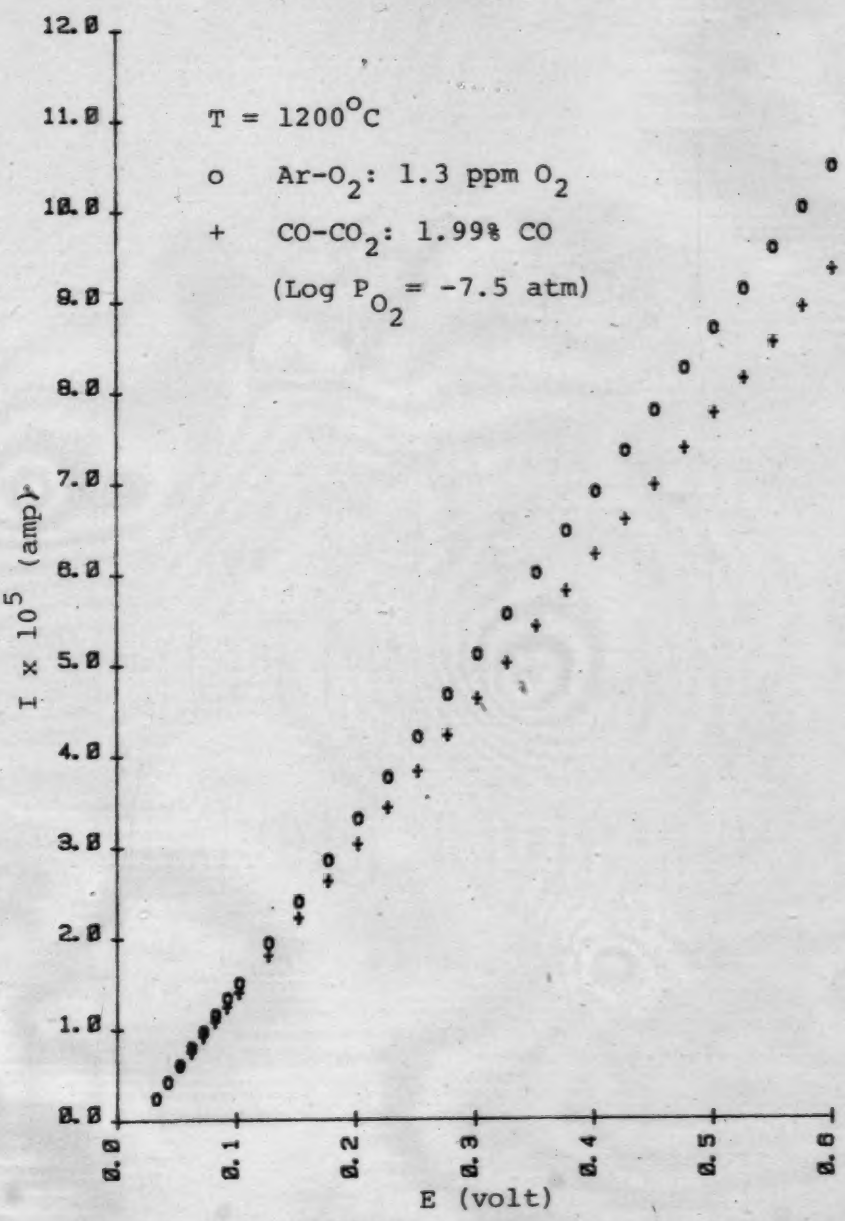

Figure 23. Current - applied potential curves for $NiAl_2O_4$ at 1200°C.

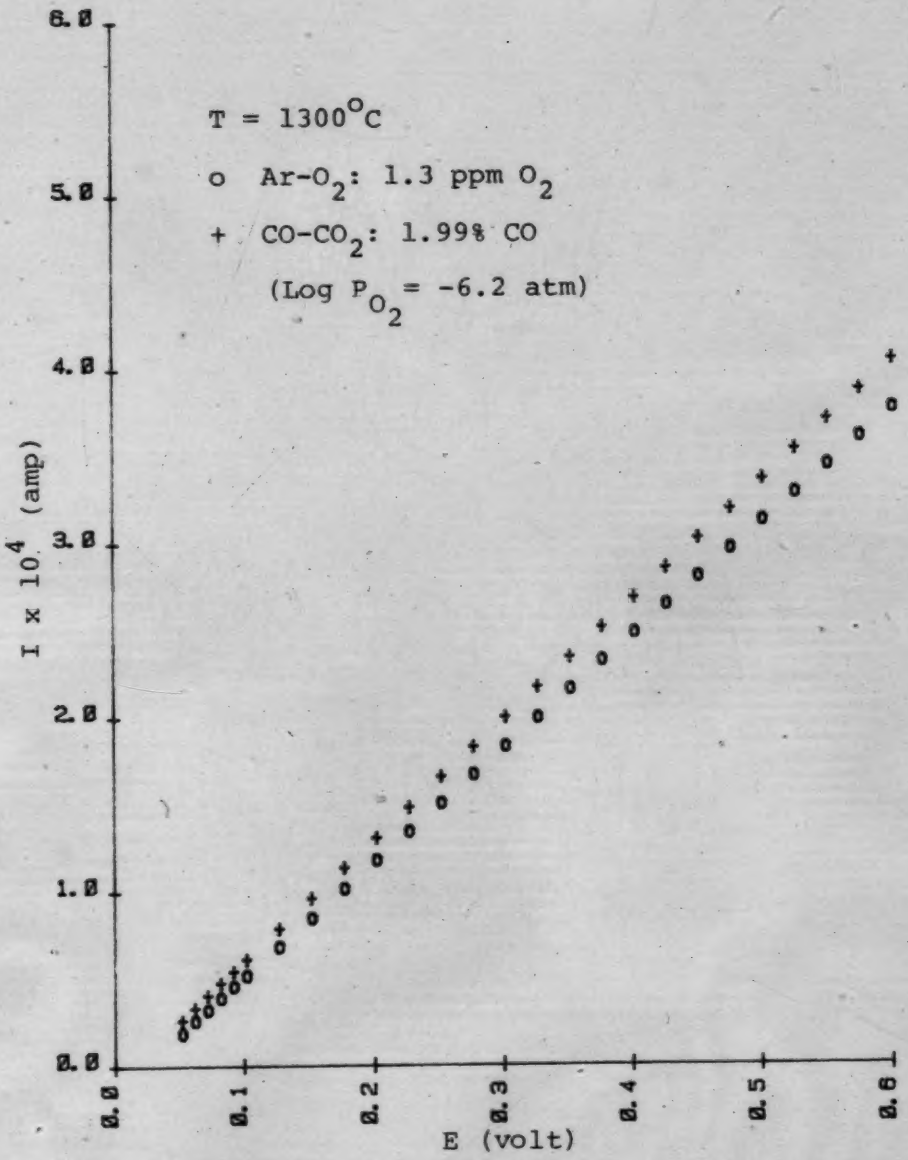

Figure 24. Current - applied potential curves for $NiAl_2O_4$ at 1300°C.

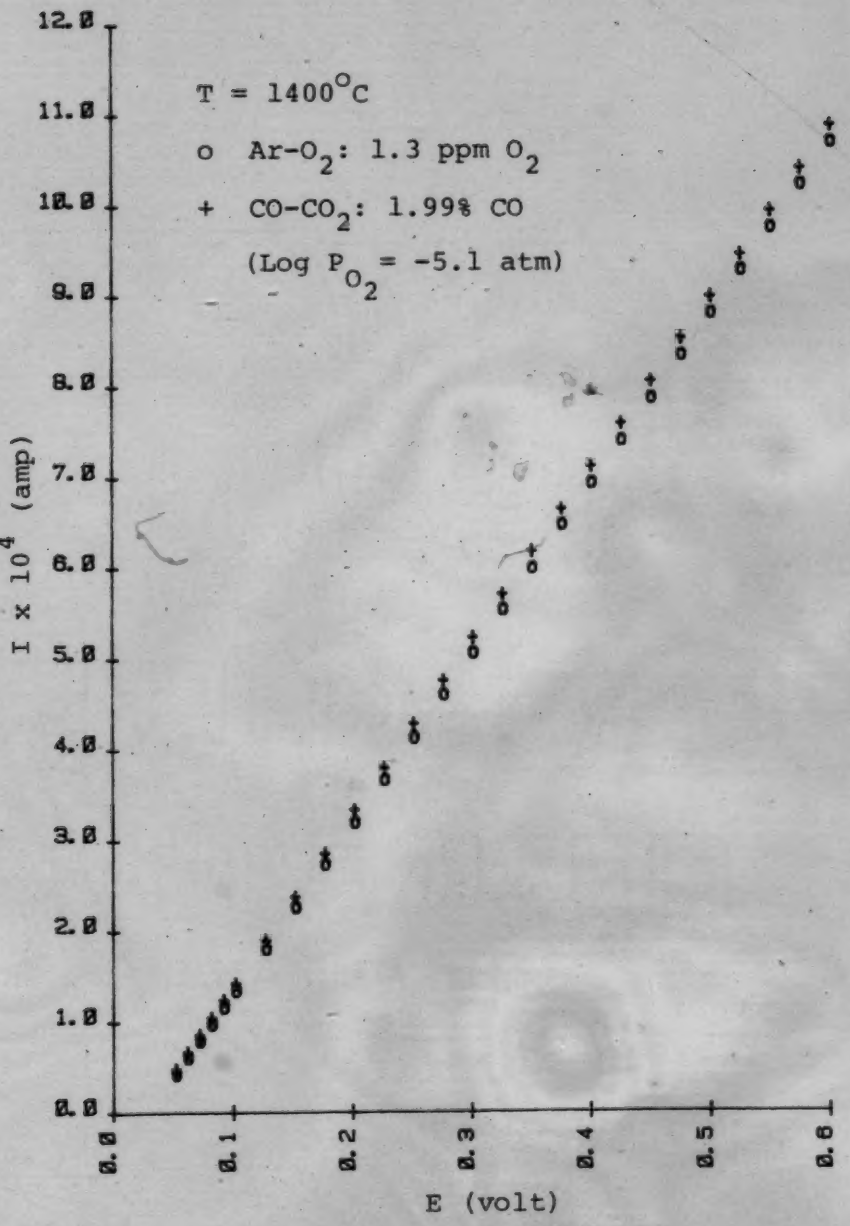

Figure 25. Current - applied potential curves for $NiAl_2O_4$ at 1400°C.

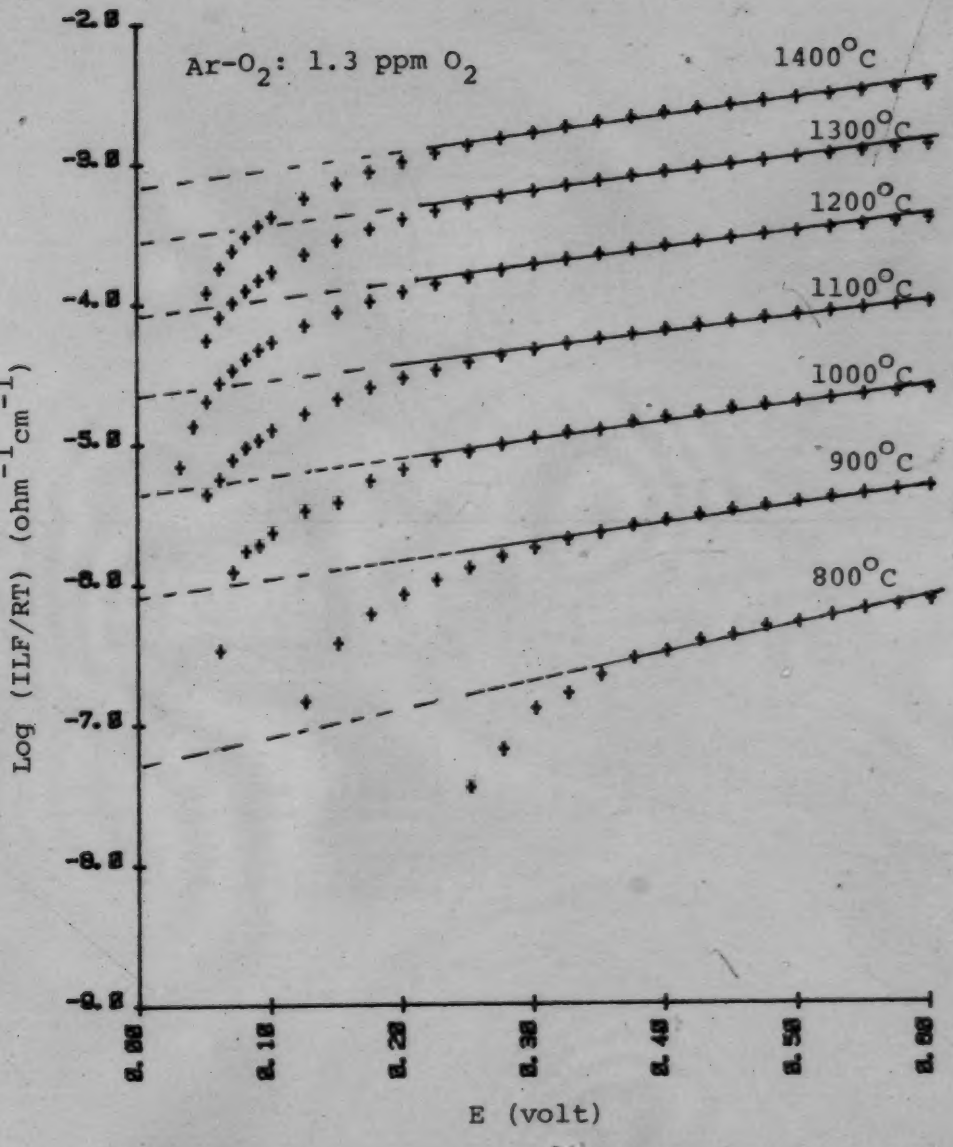

Figure 26. Logarithmic current - potential plots for $NiAl_2O_4$ ($Ar-O_2$: 1.3 ppm O_2).

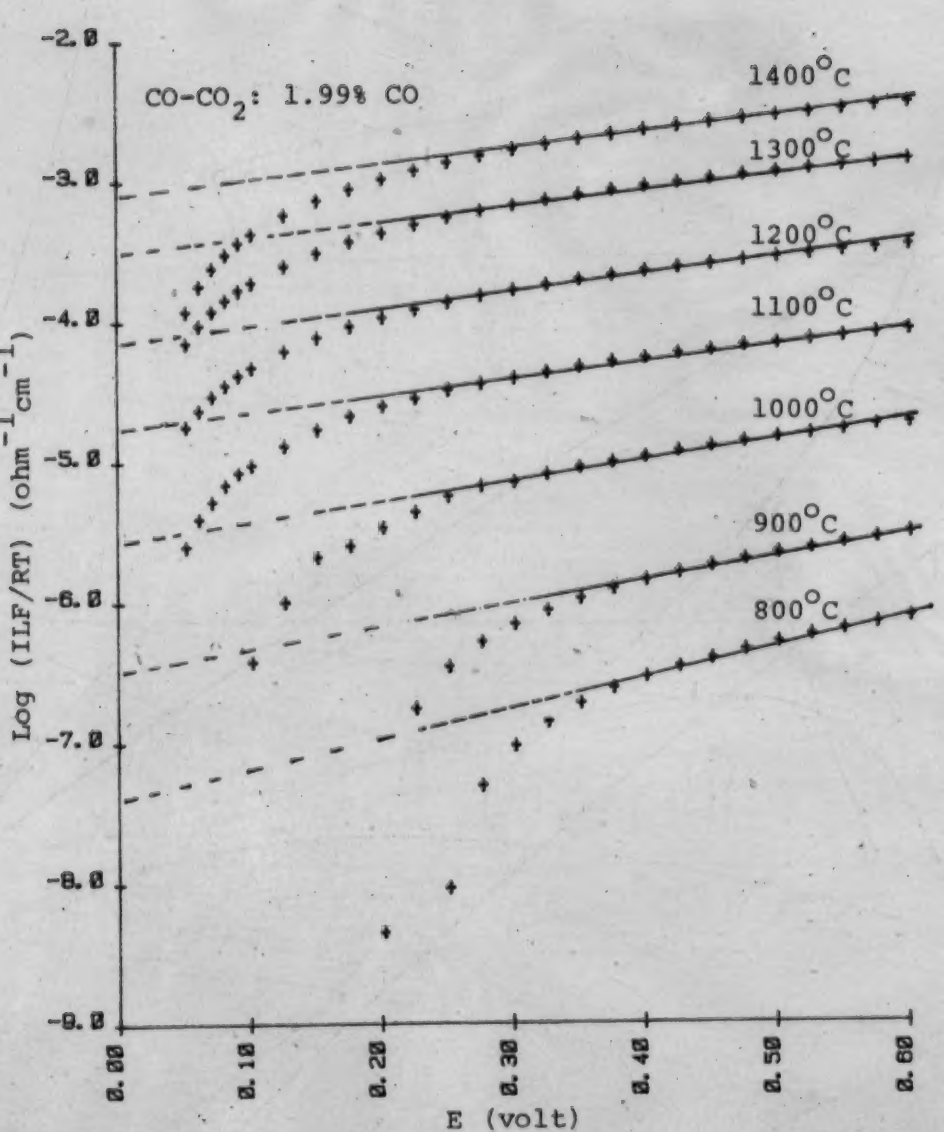

Figure 27. Logarithmic current - potential plots for $NiAl_2O_4$ ($CO-CO_2$: 1.99% CO).

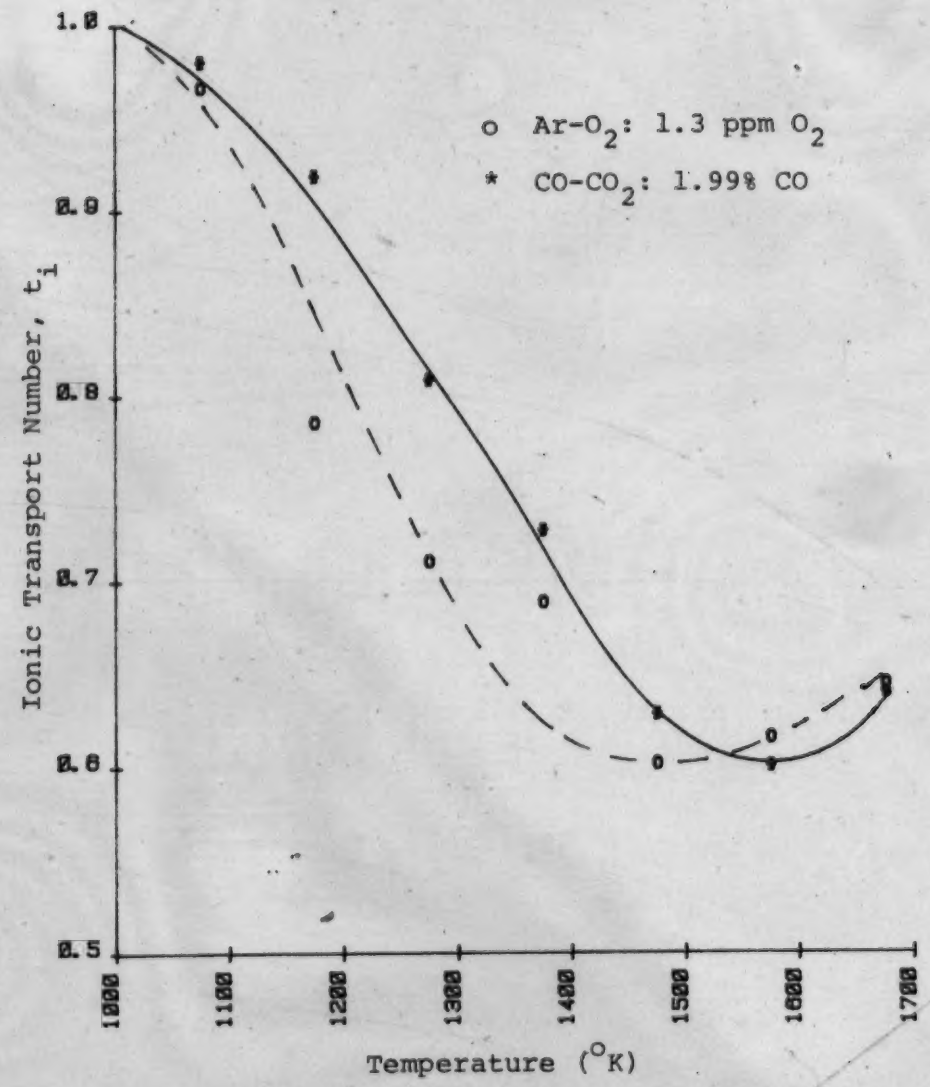

Figure 28. Ionic transport number - temperature plots for $NiAl_2O_4$ (DC Polarization Measurements).

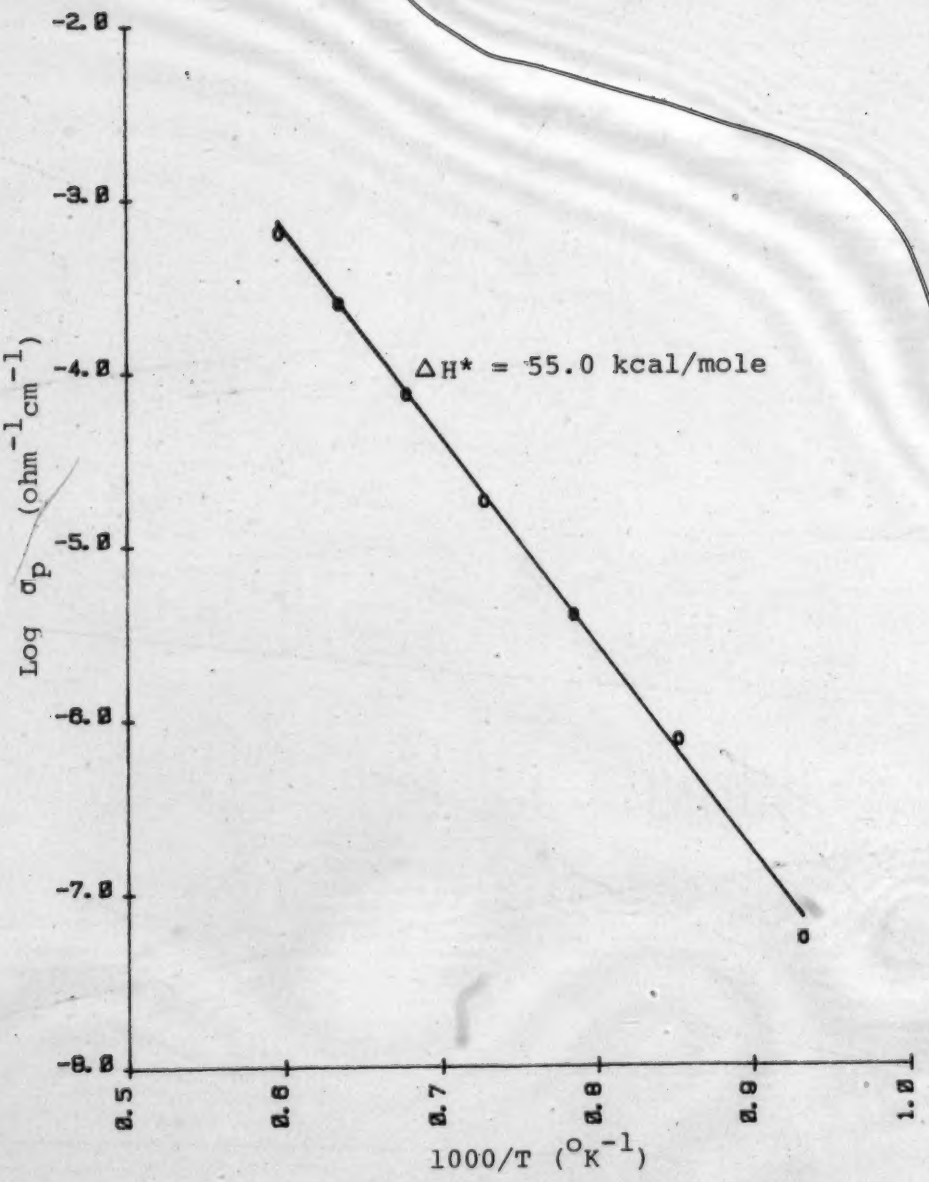

Figure 29. Arrhenius plot of the p-type conductivity of $NiAl_2O_4$ (Ar-O_2: 1.3 ppm O_2, DC Polarization Measurements).

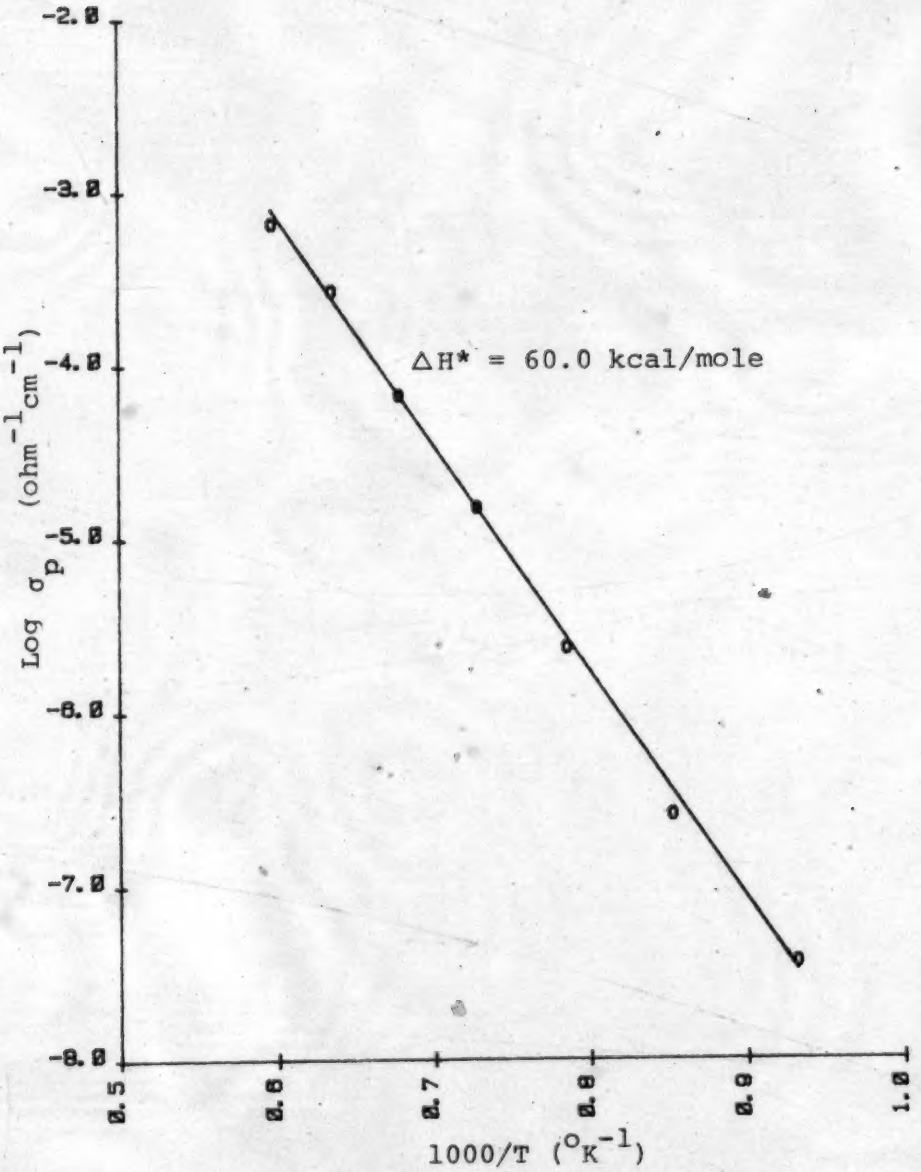

Figure 30. Arrhenius plot of the p-type conductivity of $NiAl_2O_4$ ($CO-CO_2$: 1.99% CO, DC Polarization Measurements).

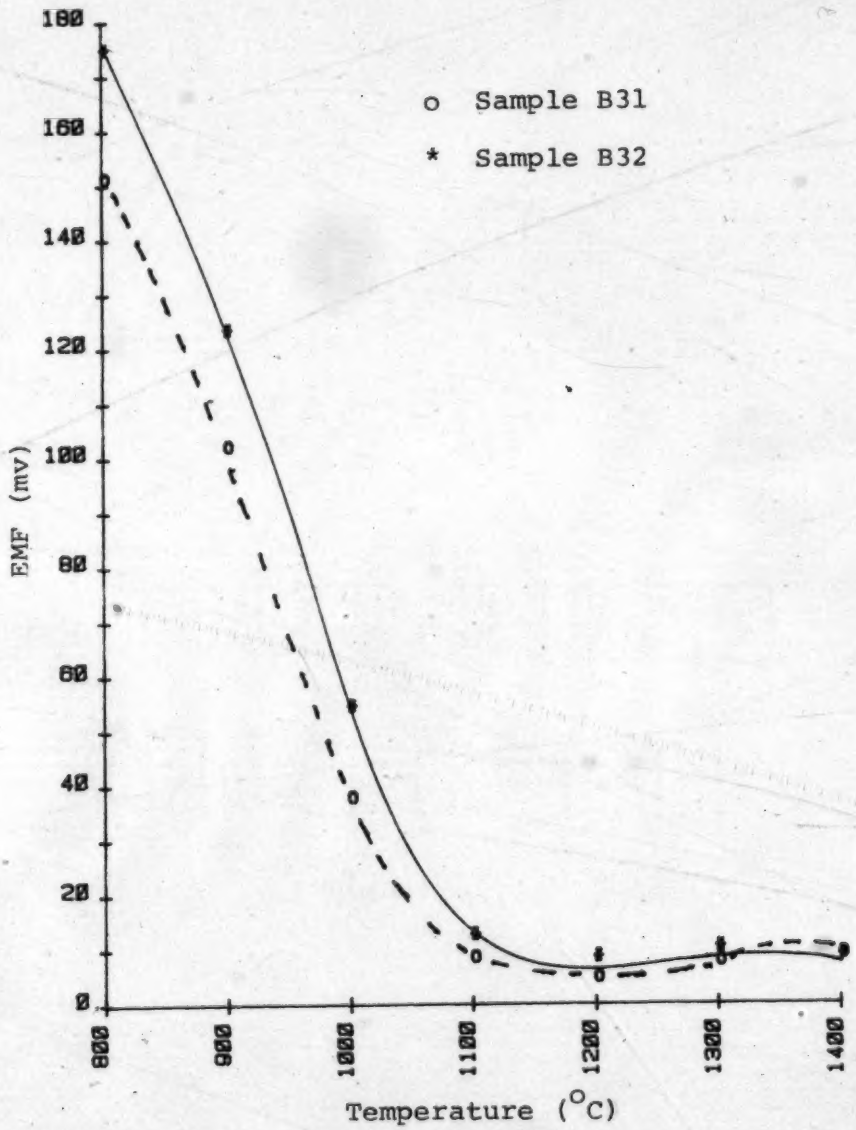

Figure 31. Emf - temperature plots for $NiAl_2O_4$ (Emf Measurements).

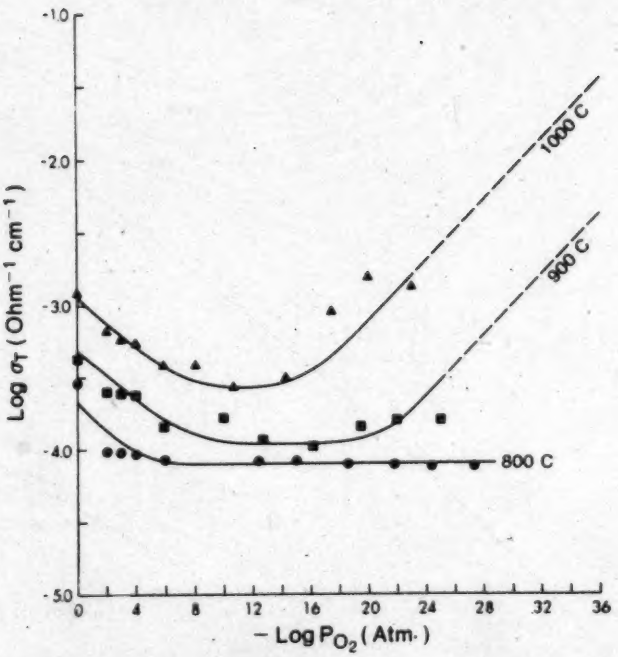

Figure 32. Conductivity isotherms for $MnAl_2O_4$ (Sample D10).

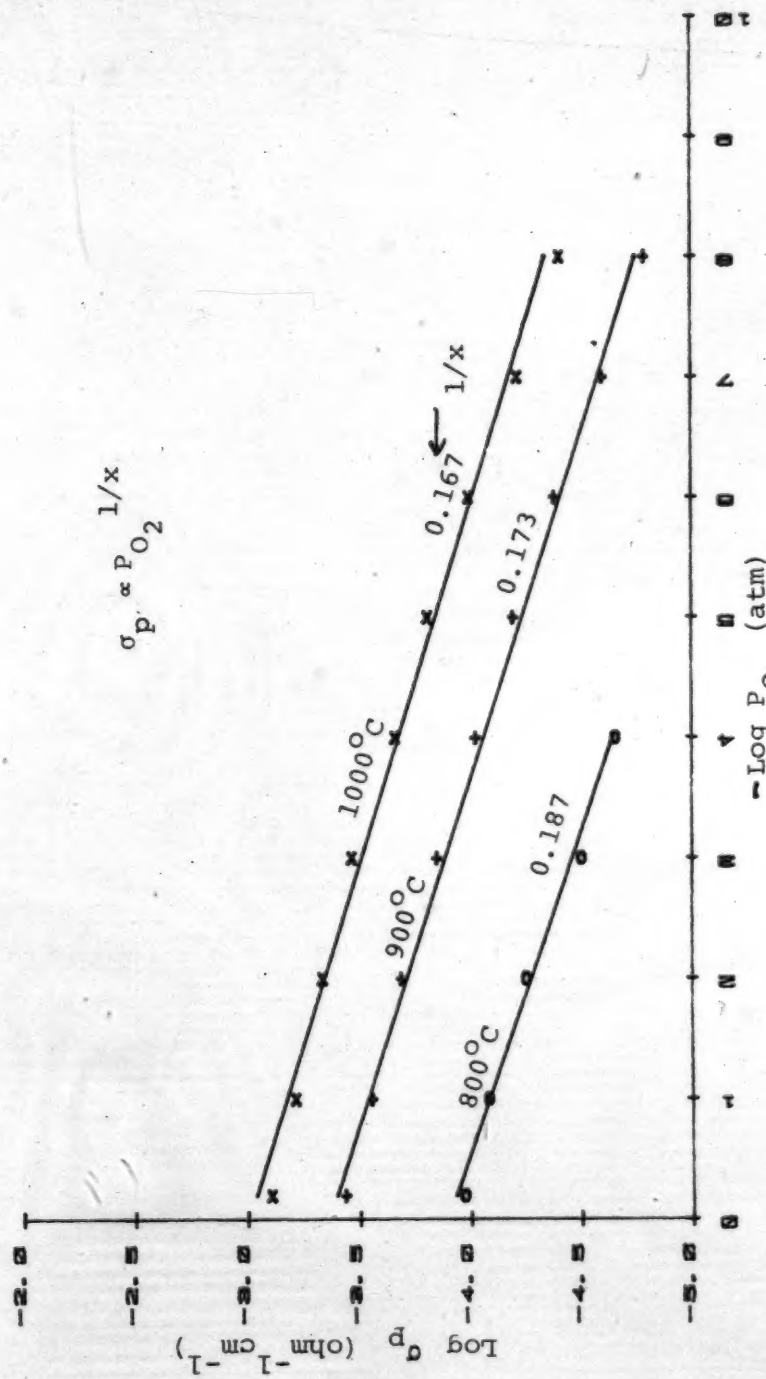

Figure 33. P-type conductivity isotherms for $MnAl_xO_4$ (Sample D10).

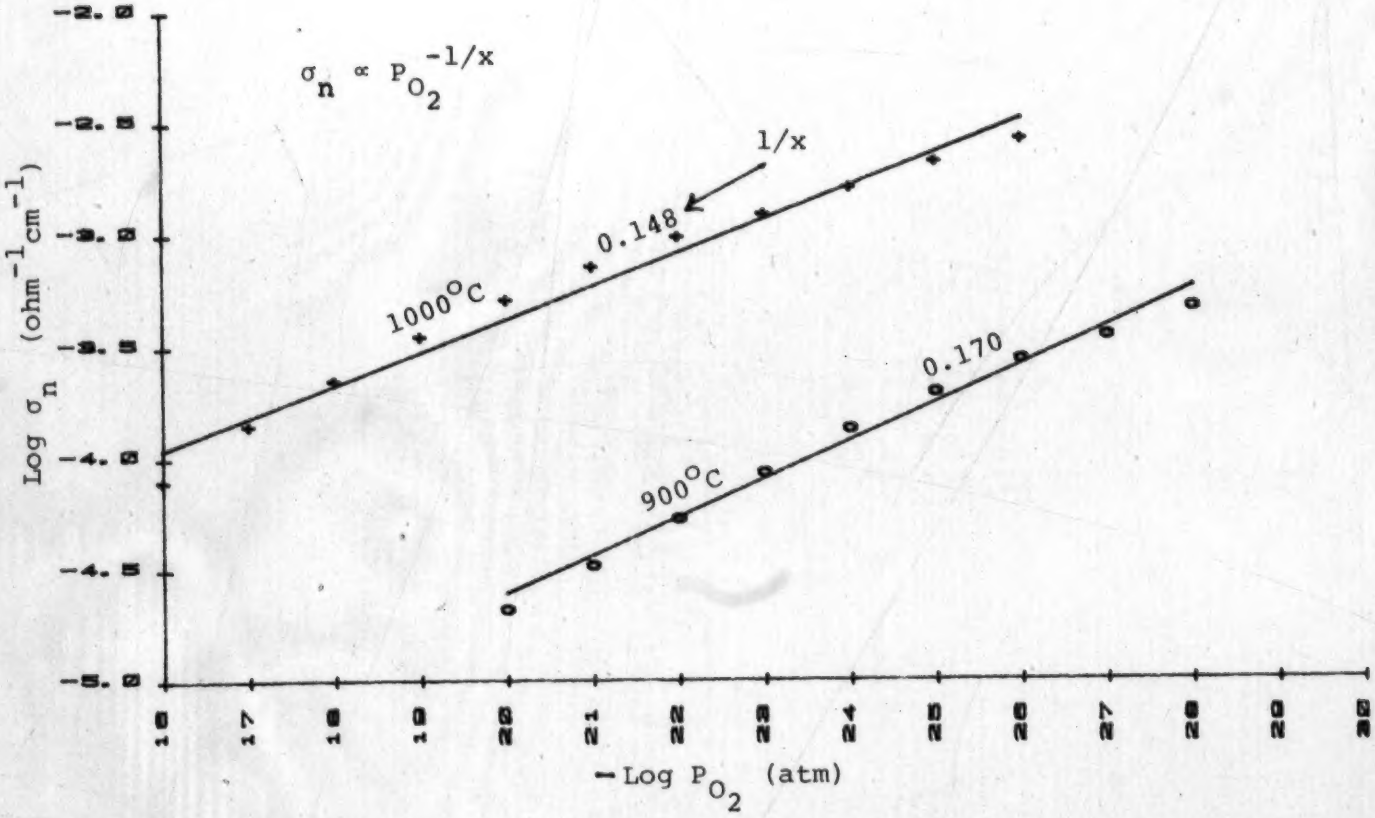

Figure 34. N-type conductivity isotherms for $MnAl_2O_4$ (Sample D10).

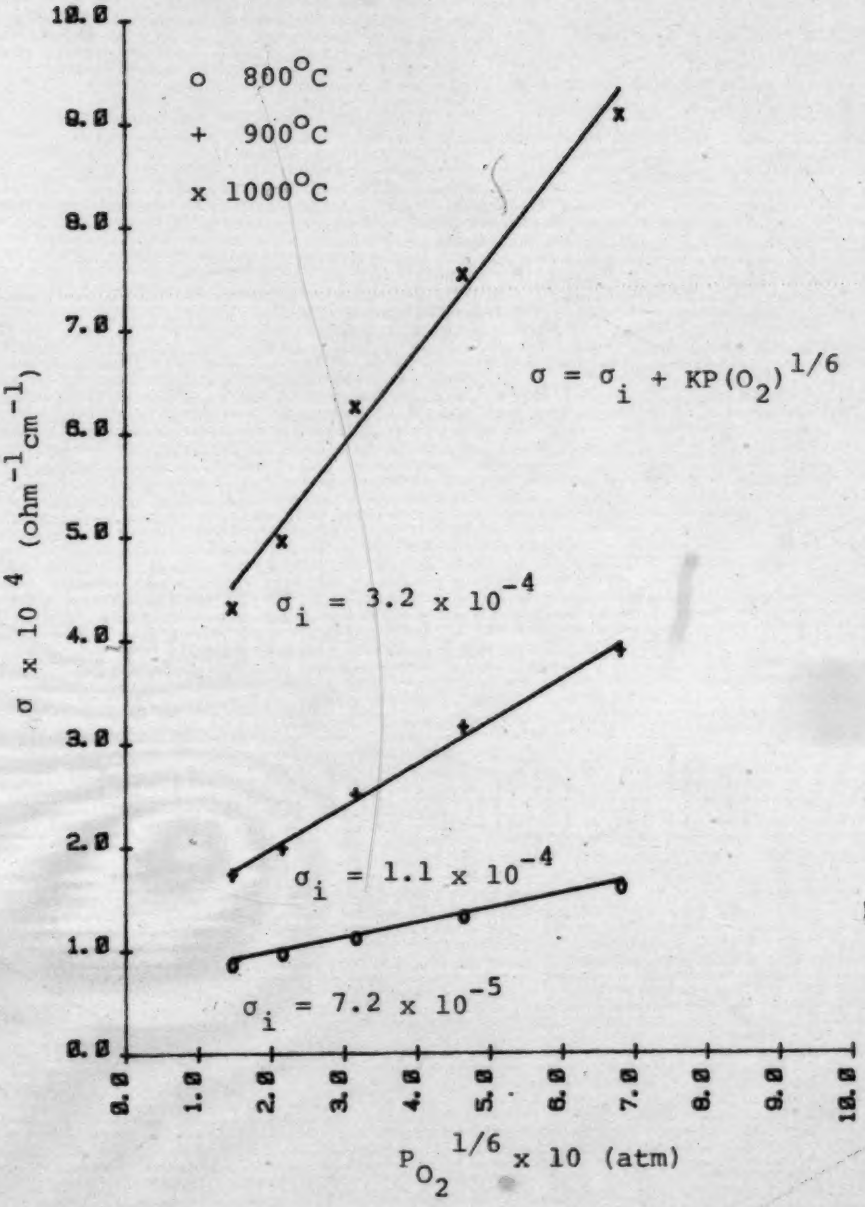

Figure 35. Determination of the ionic conductivity of $MnAl_2O_4$ (Sample D10).

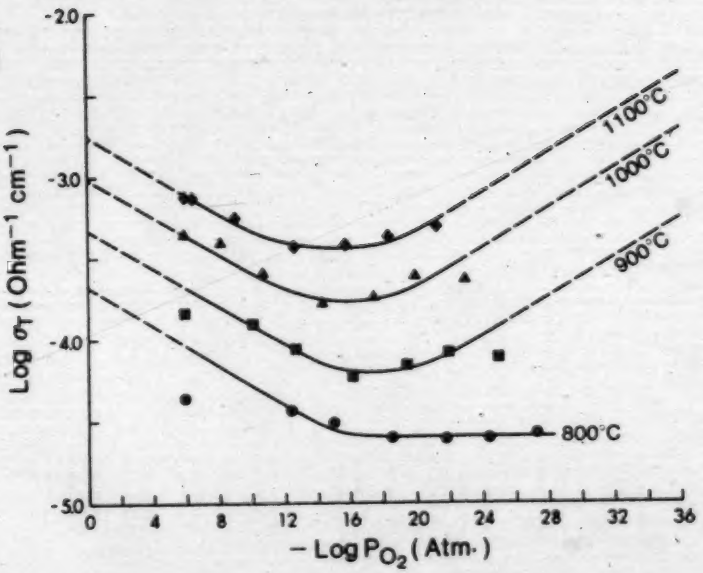

Figure 36. Conductivity isotherms for $MnAl_2O_4$ (Sample D2).

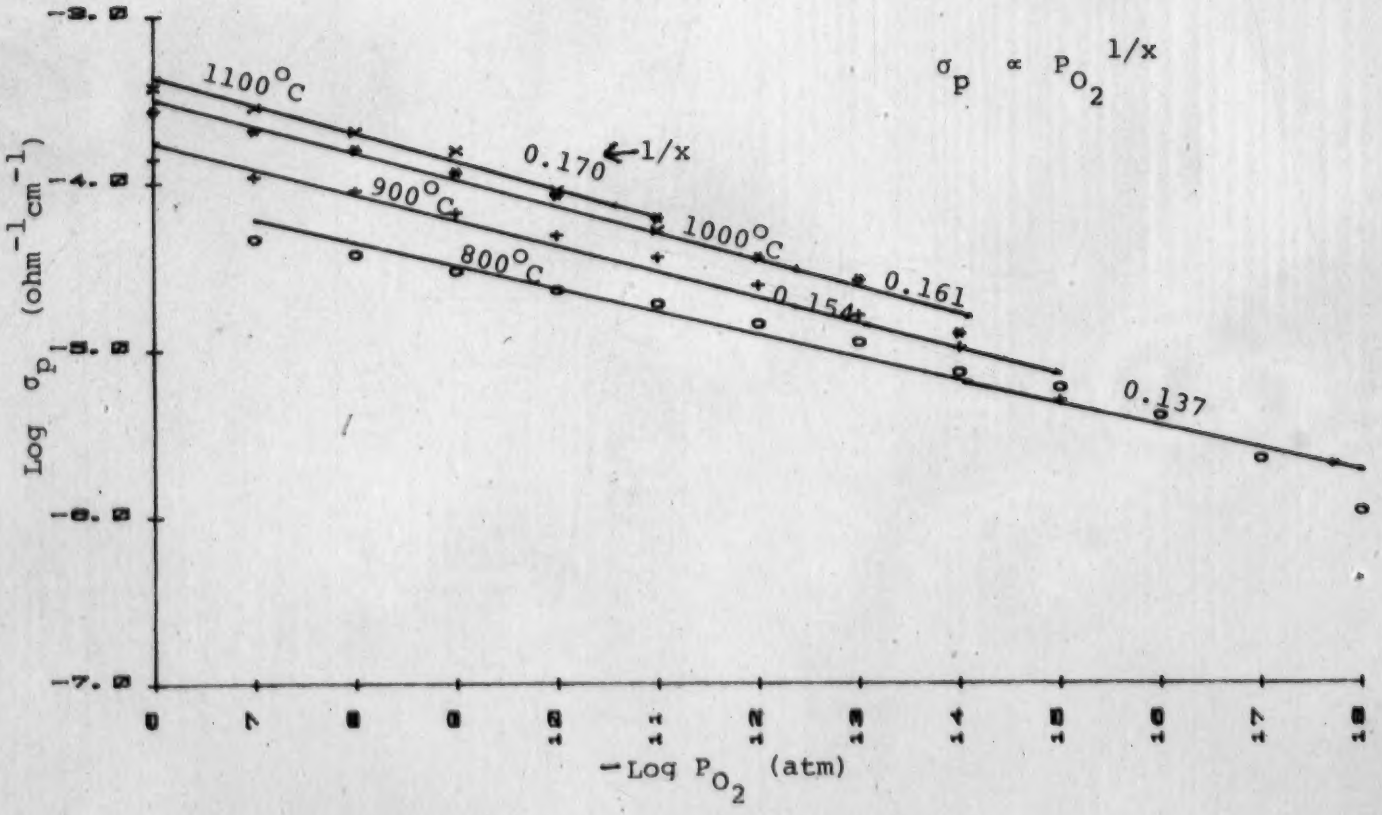

Figure 37. P-type conductivity isotherms for $MnAl_2O_4$ (Sample D2).

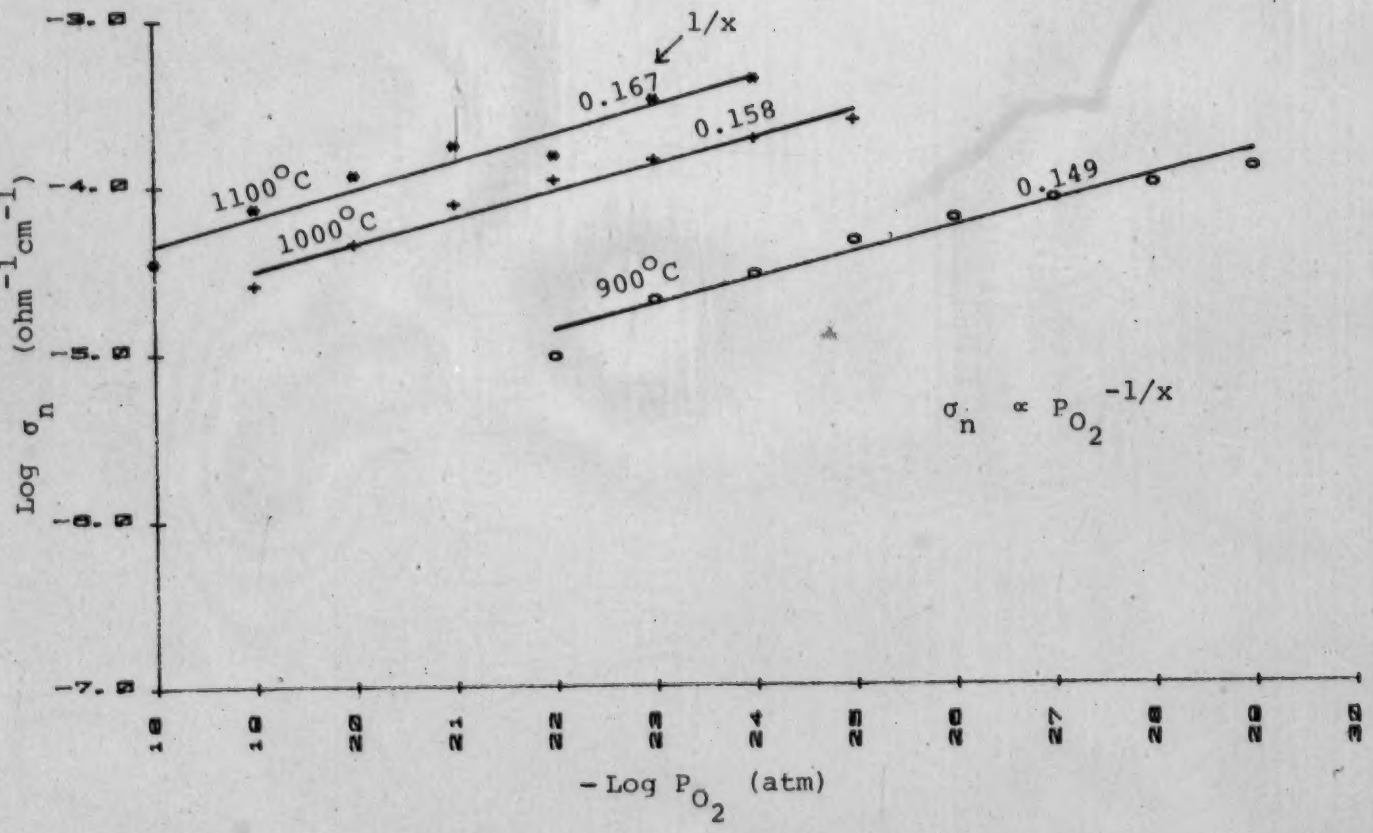

Figure 38. N-type conductivity isotherms for $MnAl_2O_4$ (Sample D2).

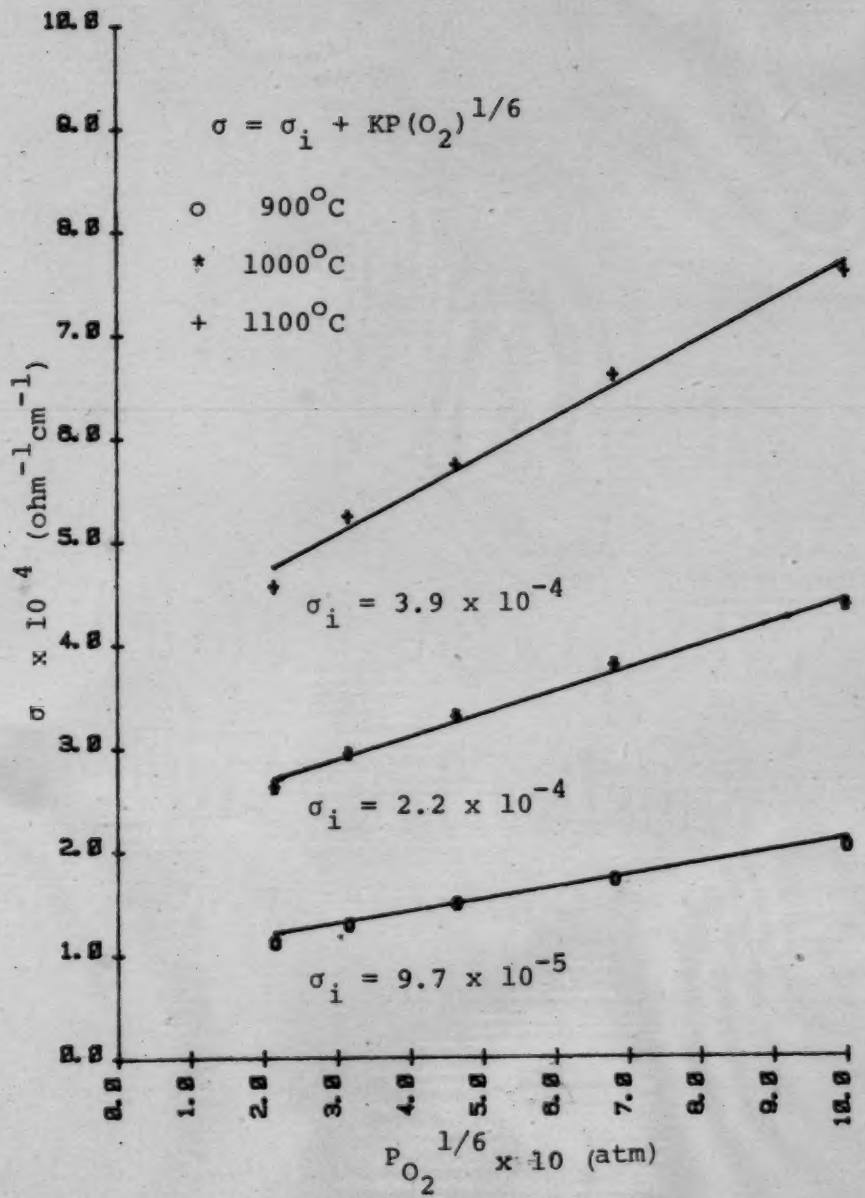

Figure 39. Determination of the ionic conductivity of $MnAl_2O_4$ (Sample D2).

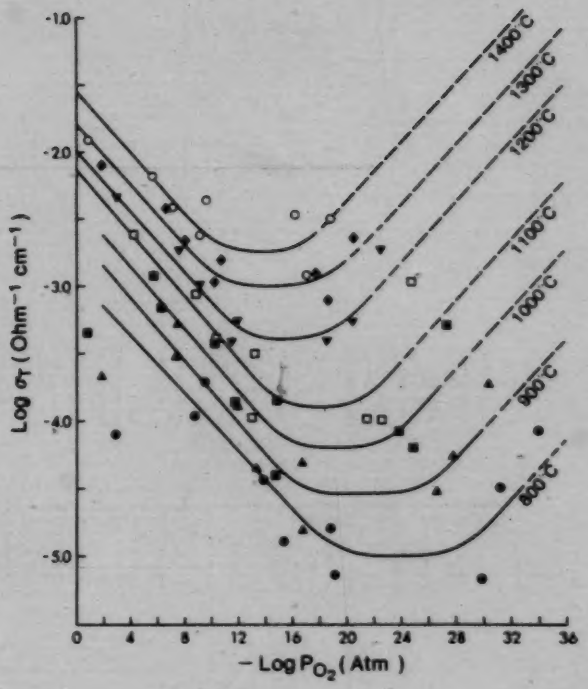

Figure 40. Conductivity isotherms for $MnAl_2O_4$ (Reversible Electrodes).

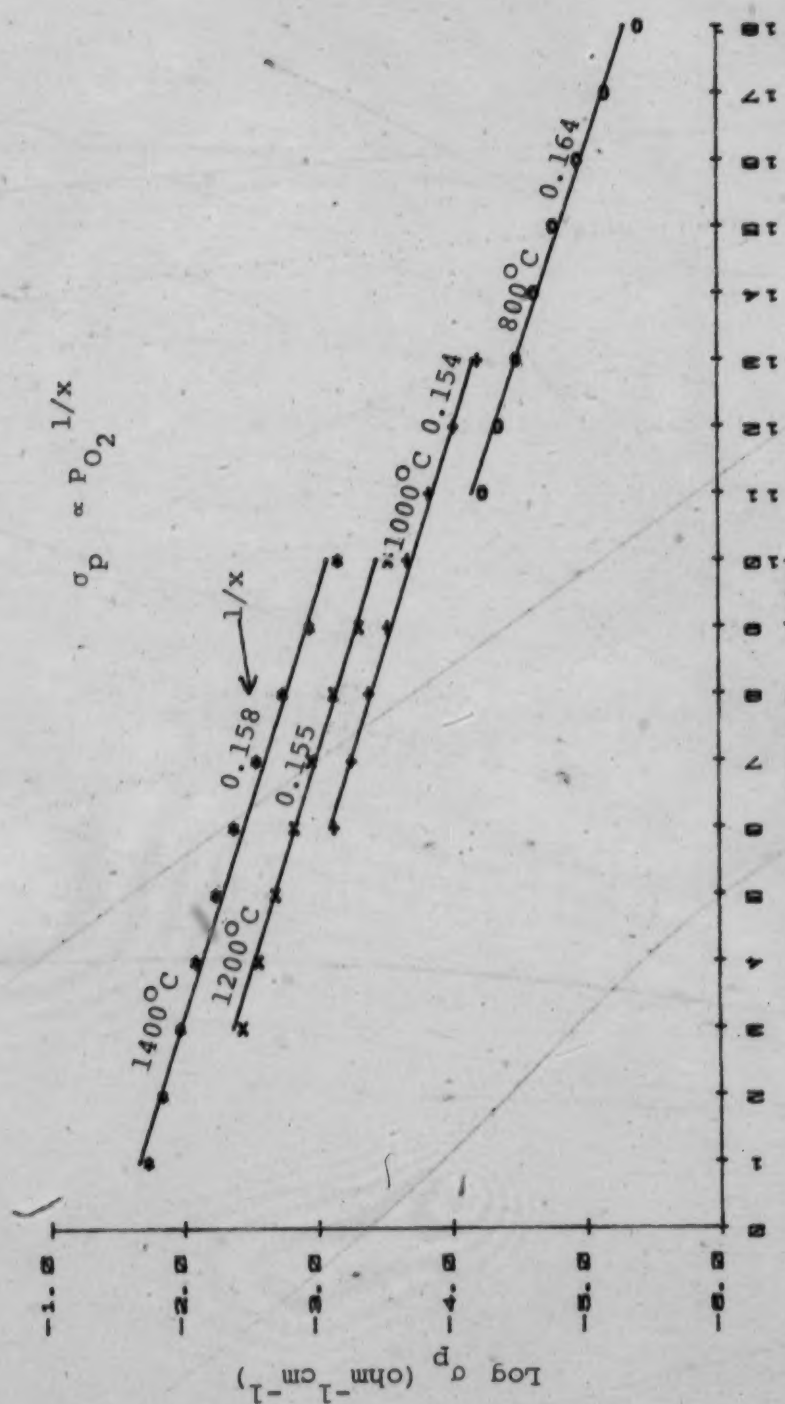

Figure 41. P-type conductivity isotherms for MnAl$_2$O$_4$ (Reversible Electrodes).

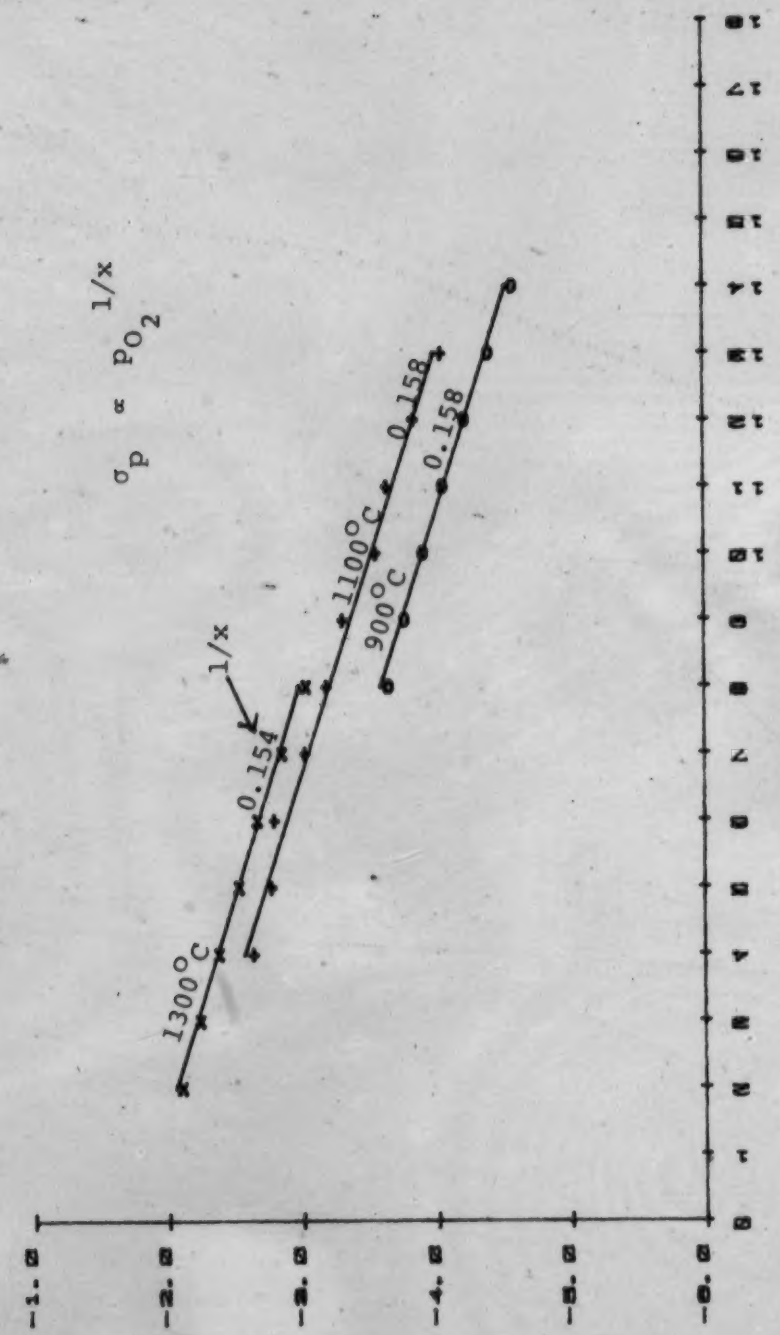

Figure 42. P-type conductivity isotherms for $MnAl_2O_4$. (Reversible Electrodes).

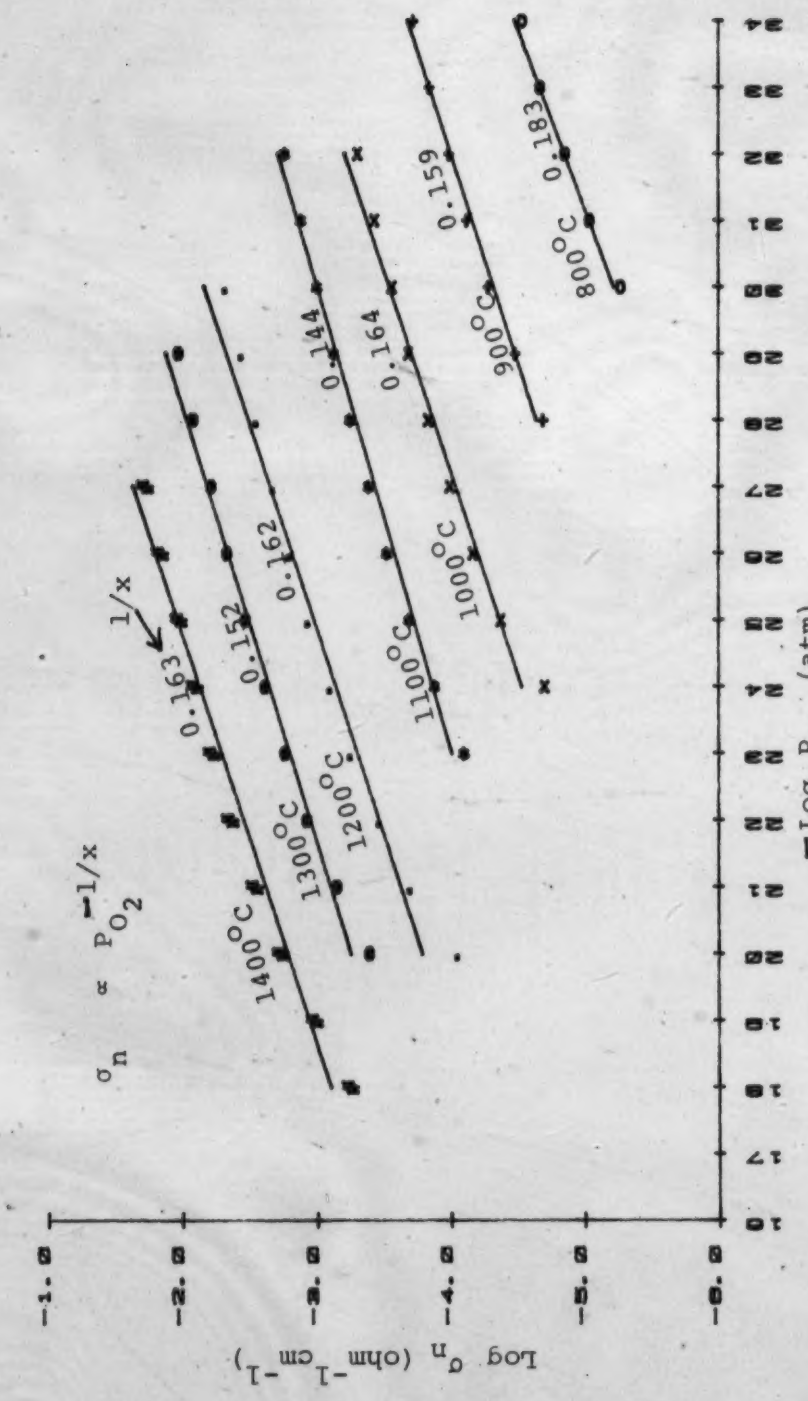

Figure 43. N-type conductivity isotherms for $MnAl_2O_4$ (Reversible Electrodes).

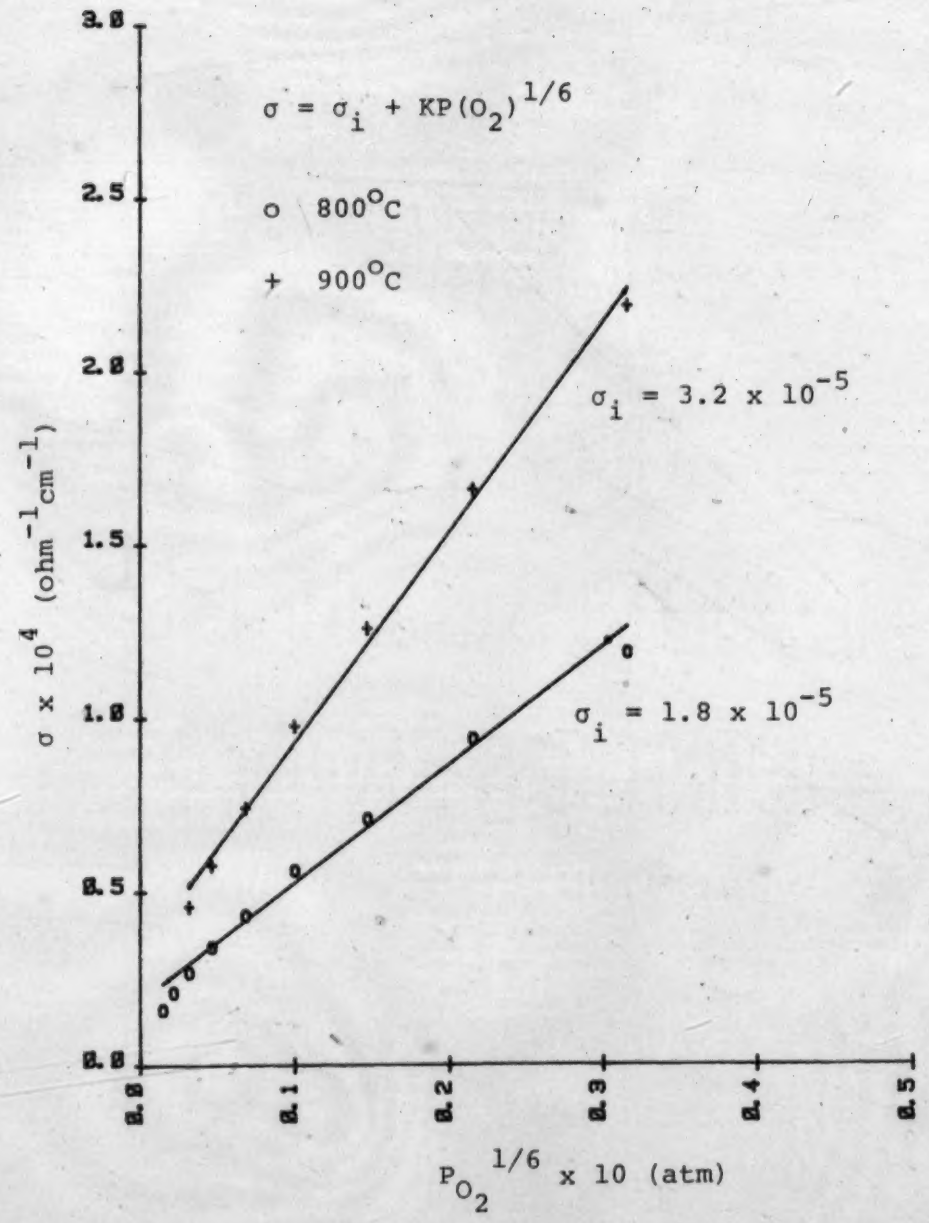

Figure 44. Determination of the ionic conductivity of $MnAl_2O_4$ at 800°-900°C (Reversible Electrodes).

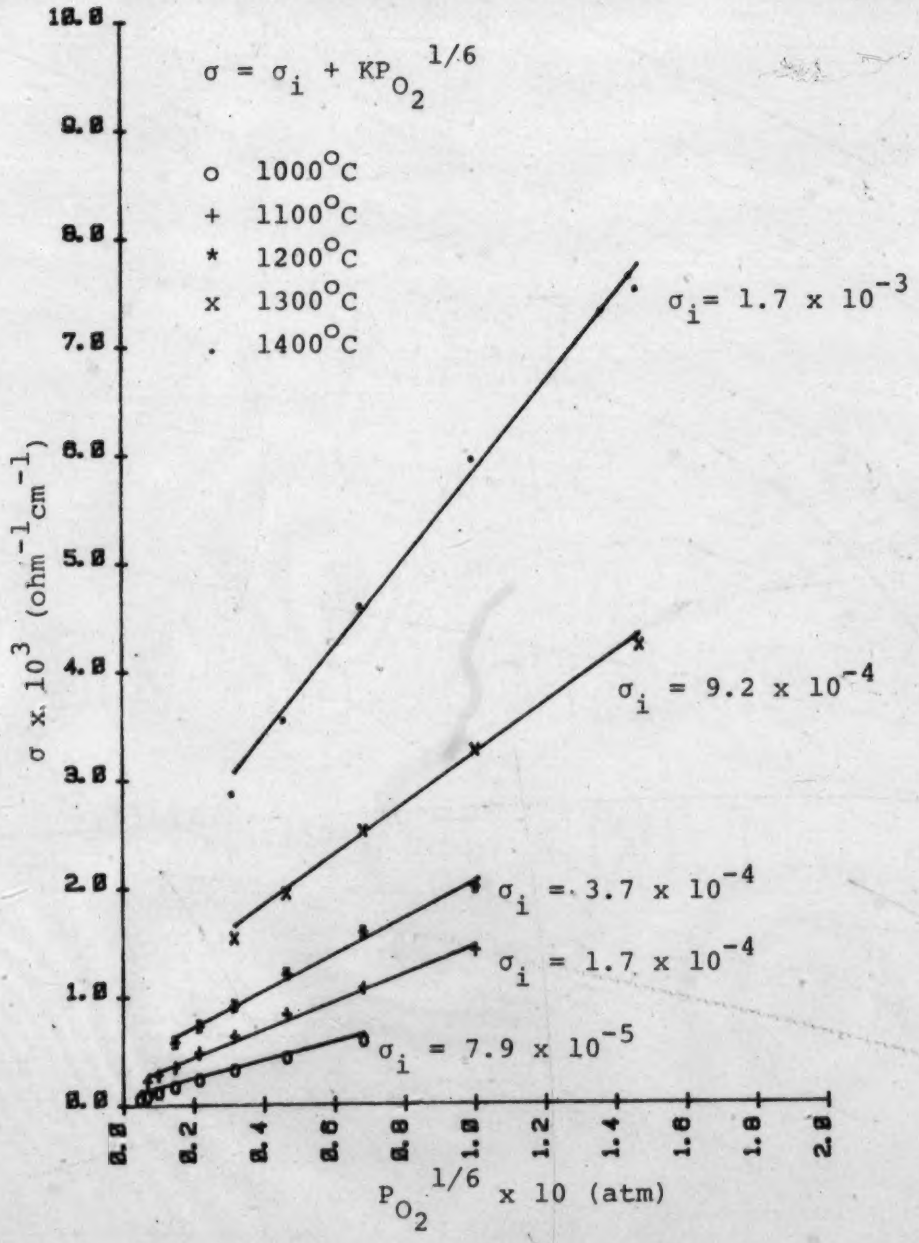

Figure 45. Determination of the ionic conductivity of $MnAl_2O_4$ at 1000°-1400°C (Reversible Electrodes).

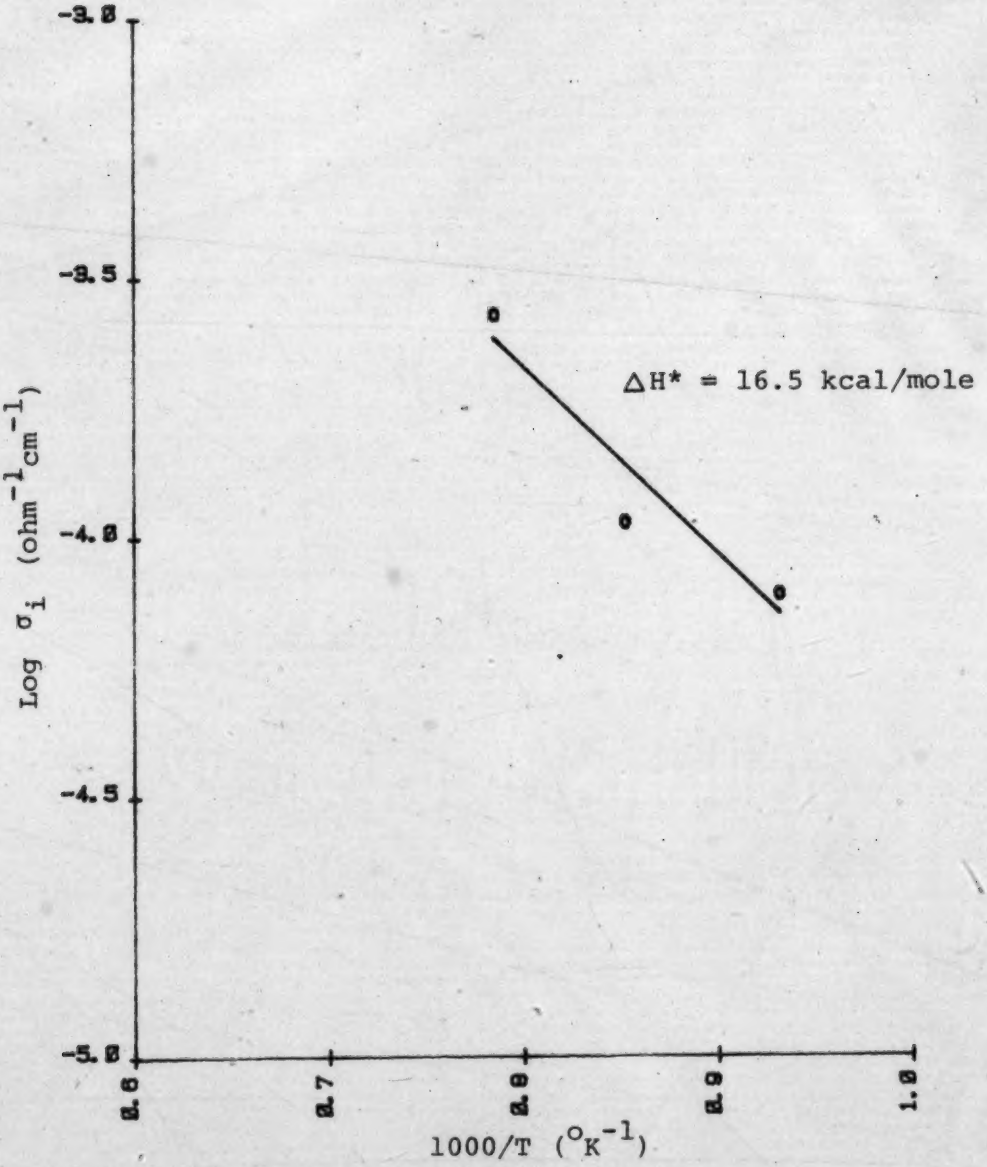

Figure 46. Arrhenius plot of the ionic conductivity of $MnAl_2O_4$ (Sample D10).

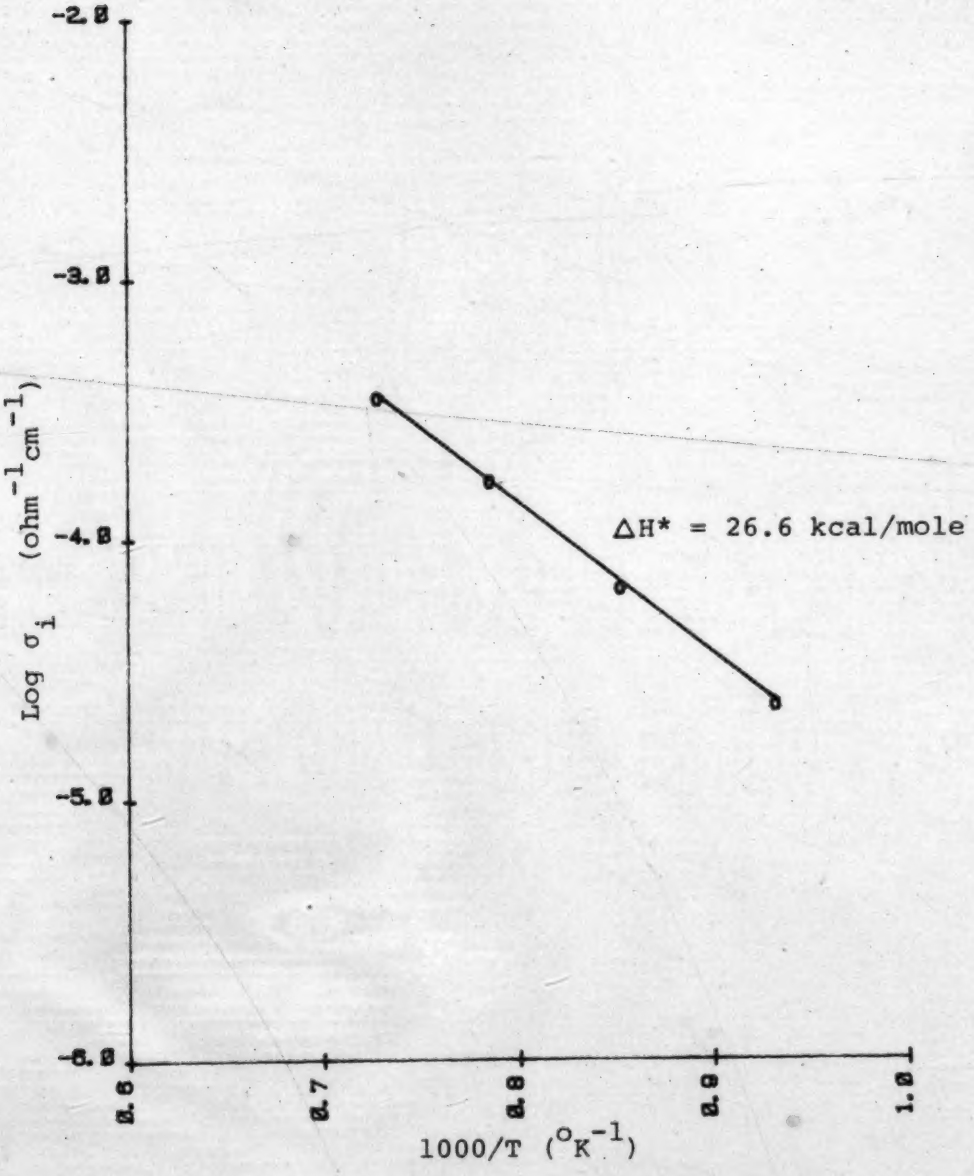

Figure 47. Arrhenius plot of the ionic conductivity of $MnAl_2O_4$ (Sample D2).

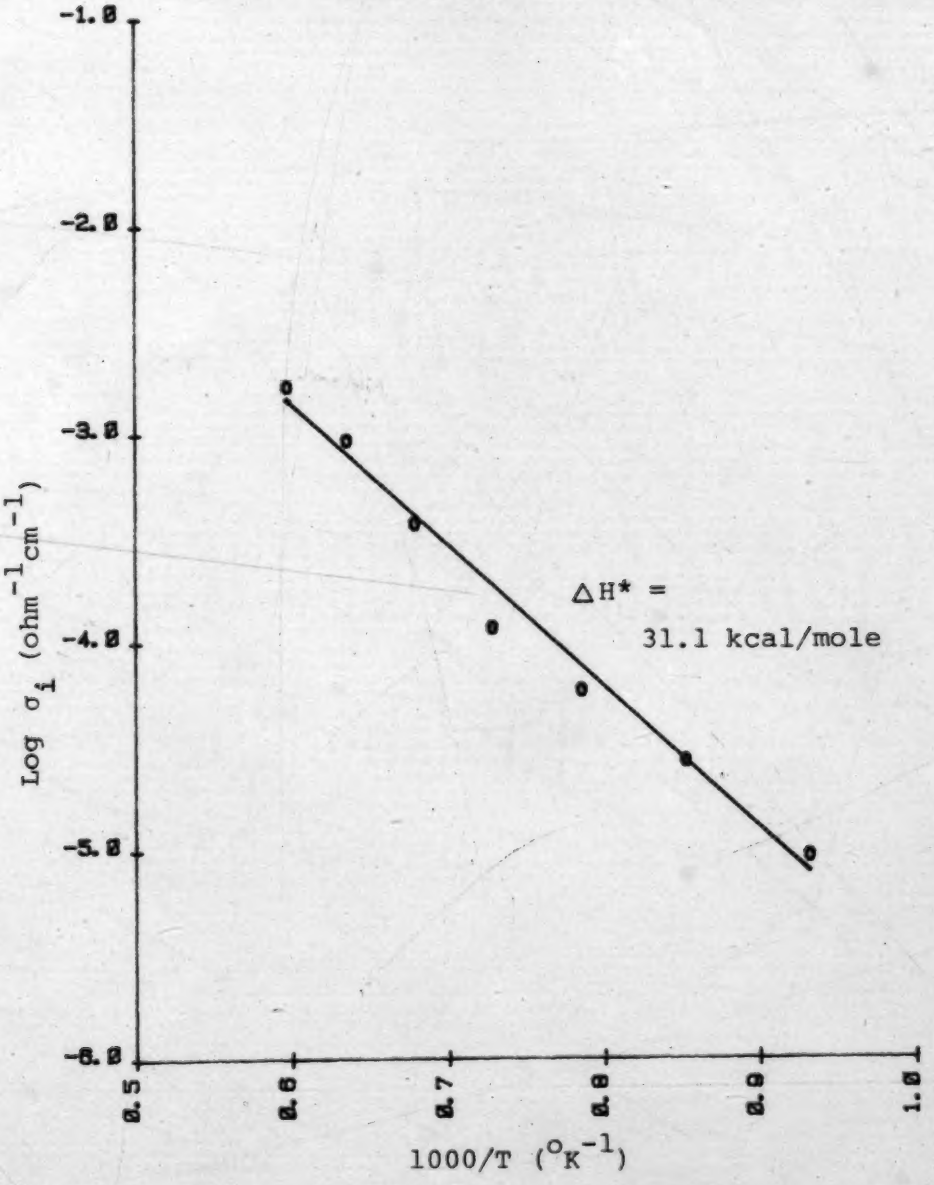

Figure 48. Arrhenius plot of the ionic conductivity of $MnAl_2O_4$ (Reversible Electrodes).

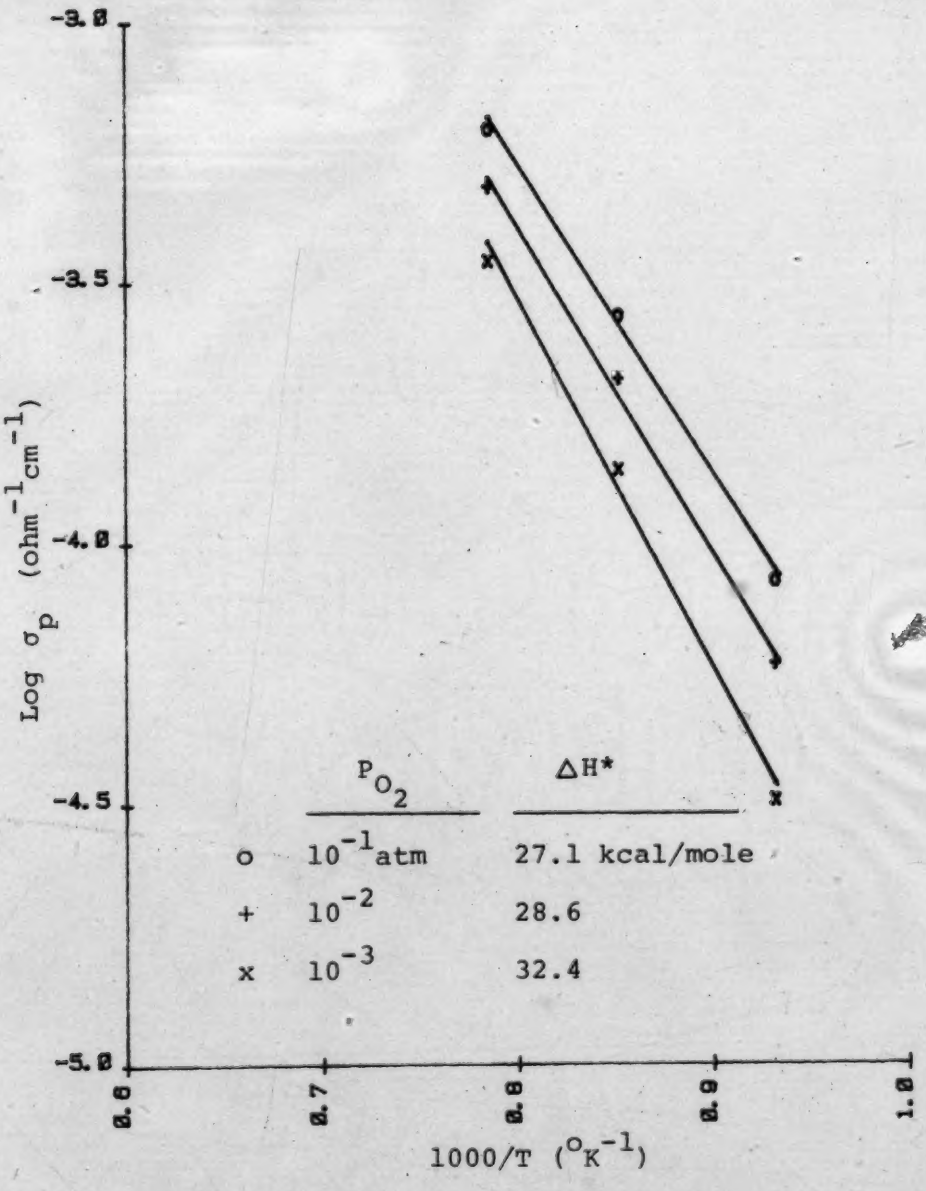

Figure 49. Arrhenius plots of the p-type conductivity of $MnAl_2O_4$ (Sample D10).

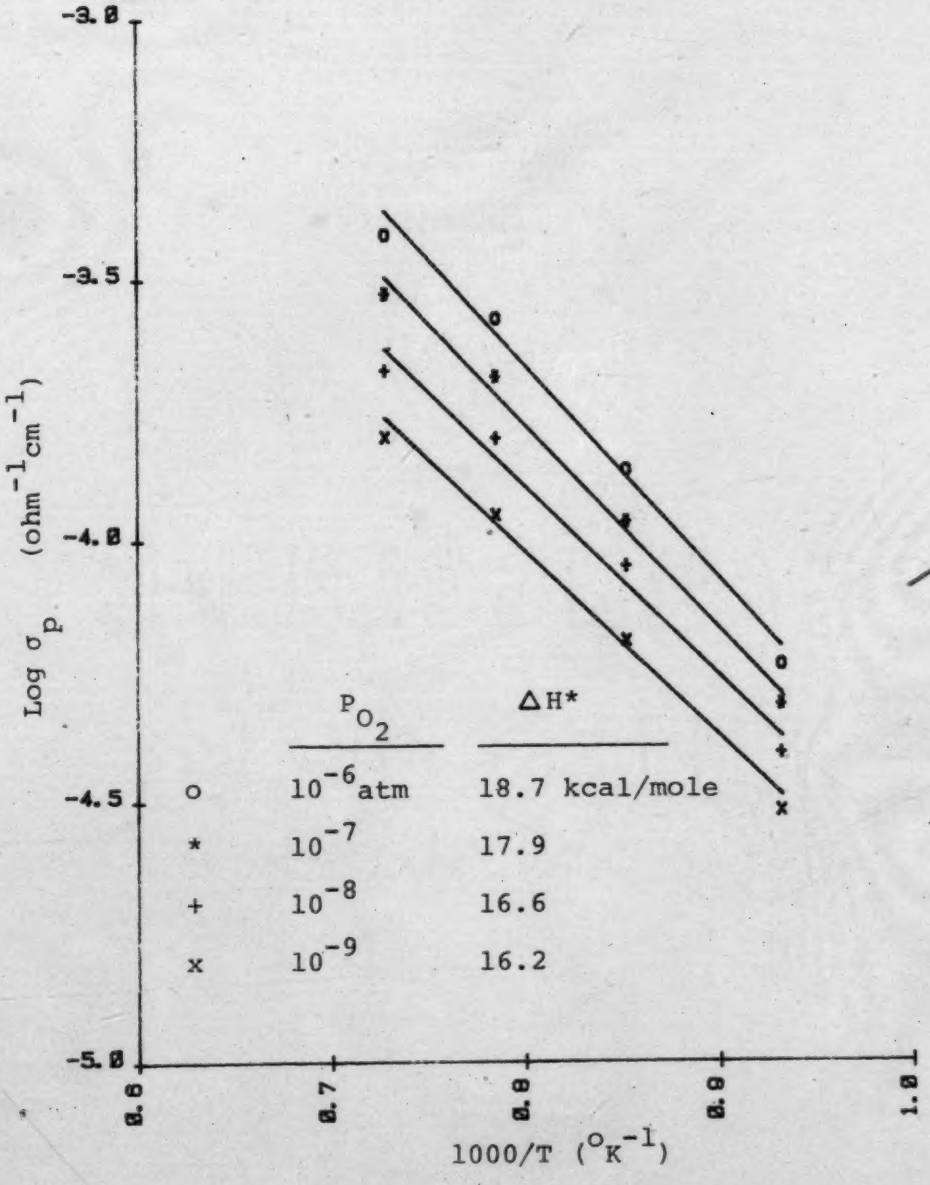

Figure 50. Arrhenius plots of the p-type conductivity of $MnAl_2O_4$ (Sample D2).

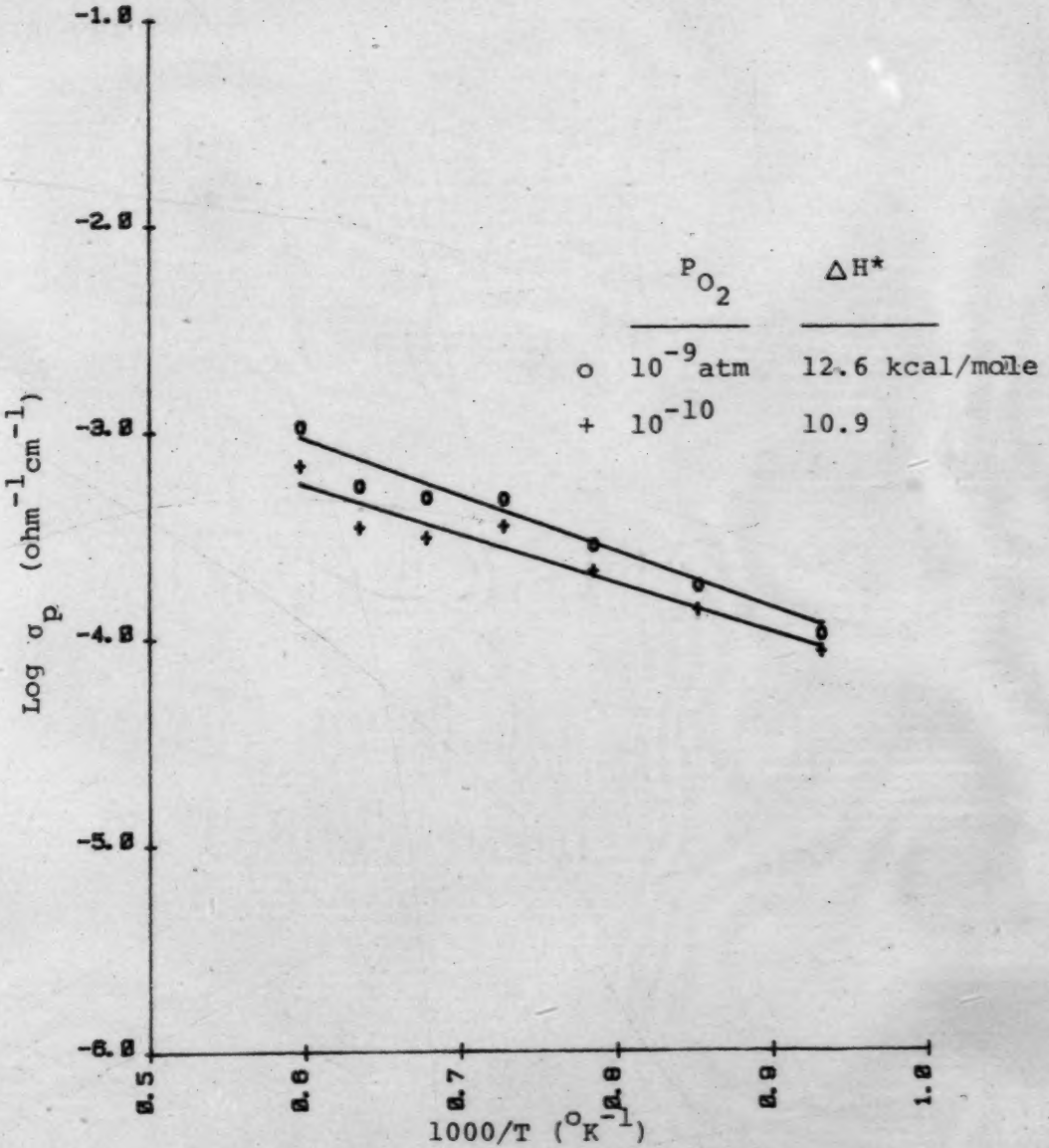

Figure 51. Arrhenius plots of the p-type conductivity of $MnAl_2O_4$ (Reversible Electrodes).

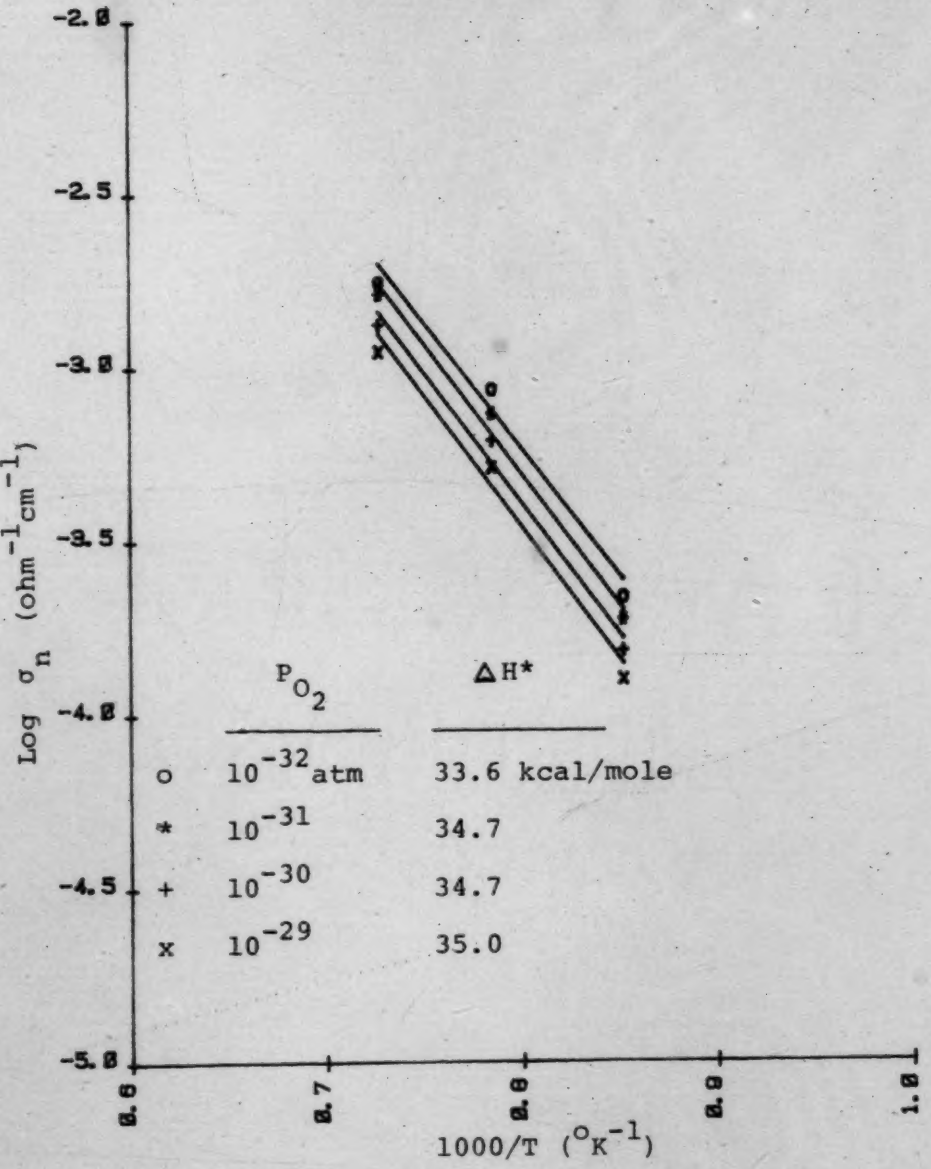

Figure 52. Arrhenius plots of the n-type conductivity of $MnAl_2O_4$ (Sample D2).

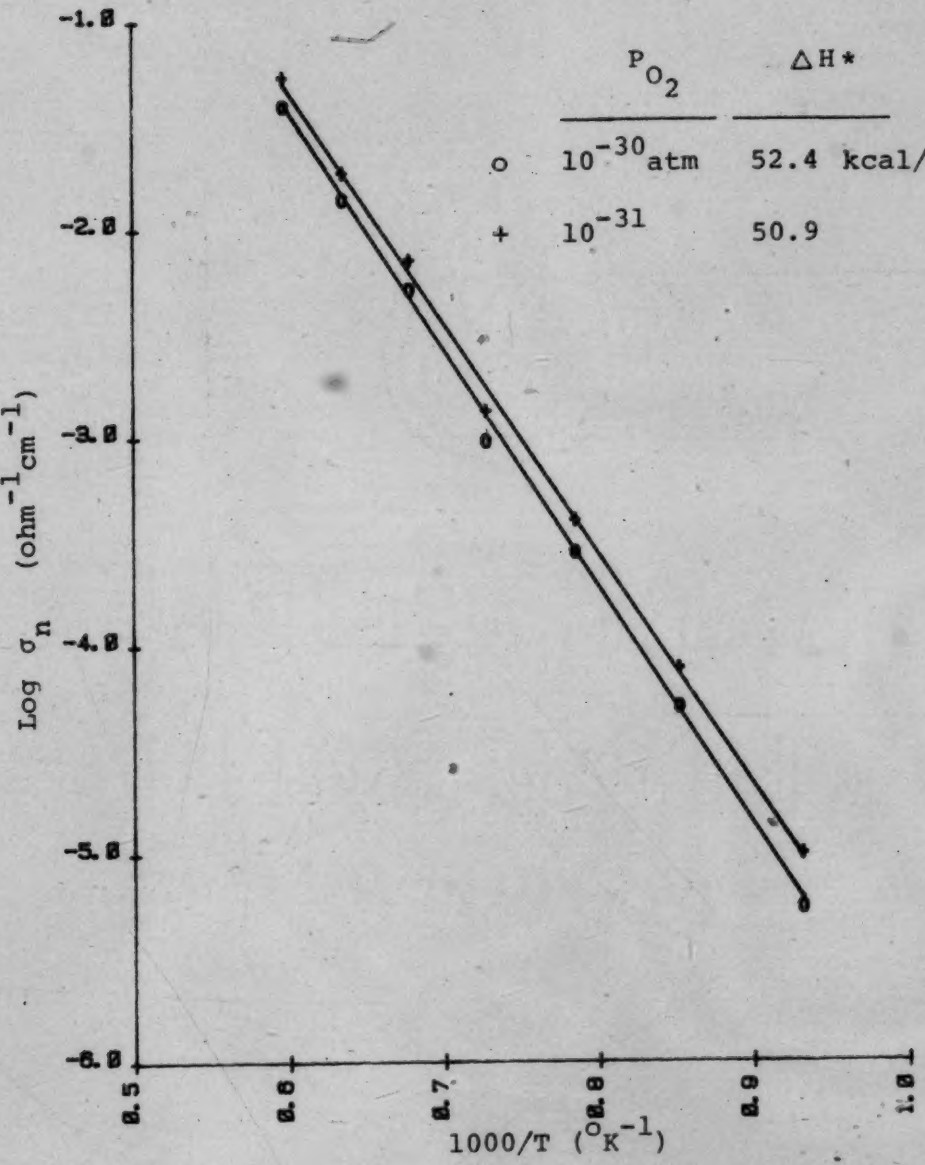

Figure 53. Arrhenius plots of the n-type conductivity of $MnAl_2O_4$ (Reversible Electrodes).

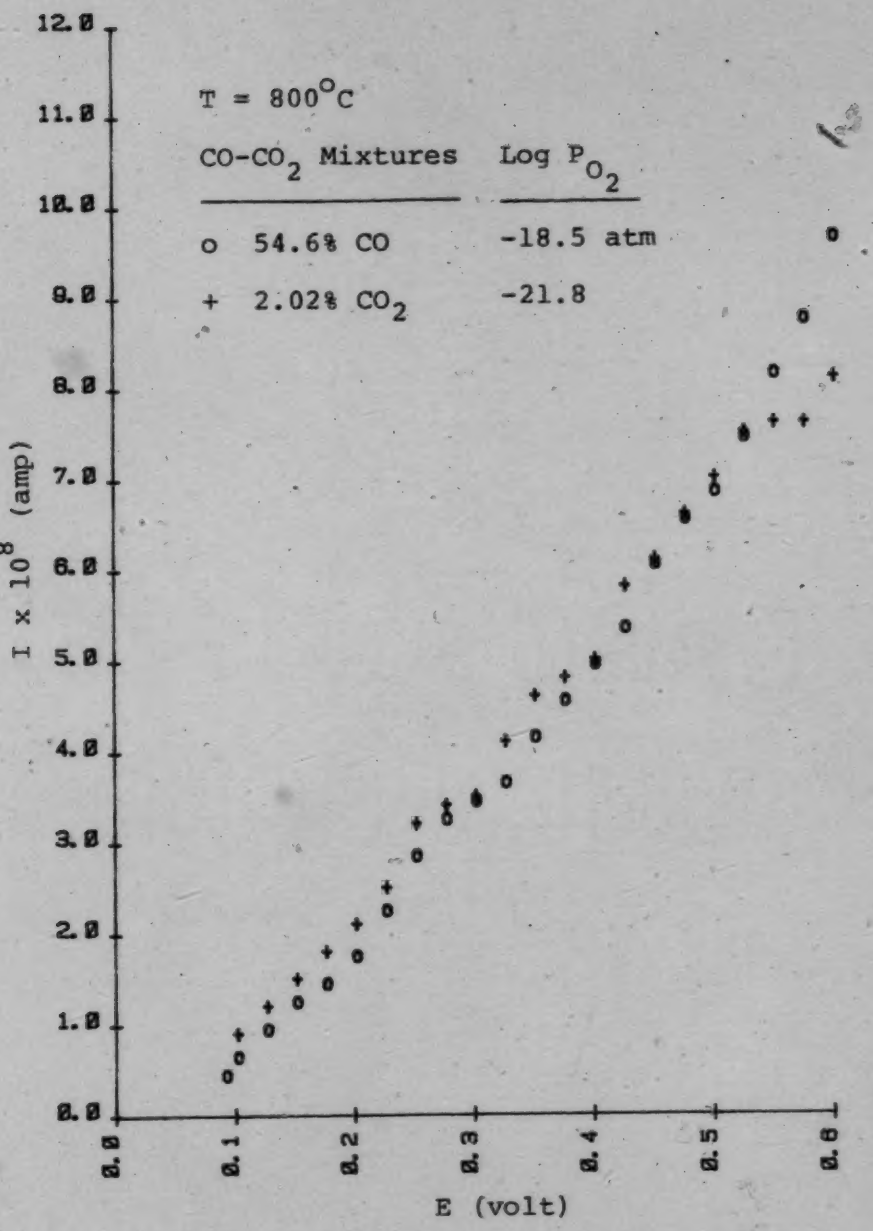

Figure 54. Current - applied potential curves for $MnAl_2O_4$ at 800°C.

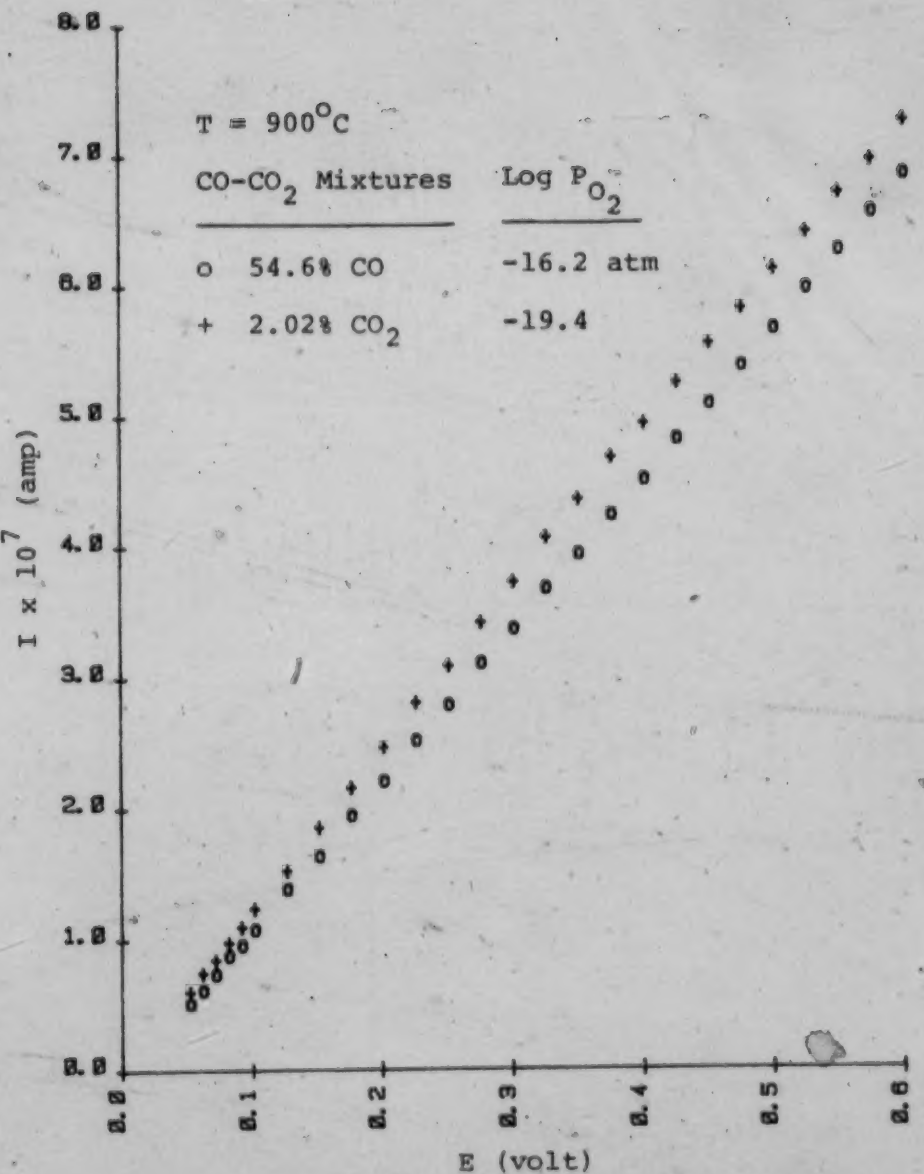

Figure 55. Current - applied potential curves for $MnAl_2O_4$ at 900°C.

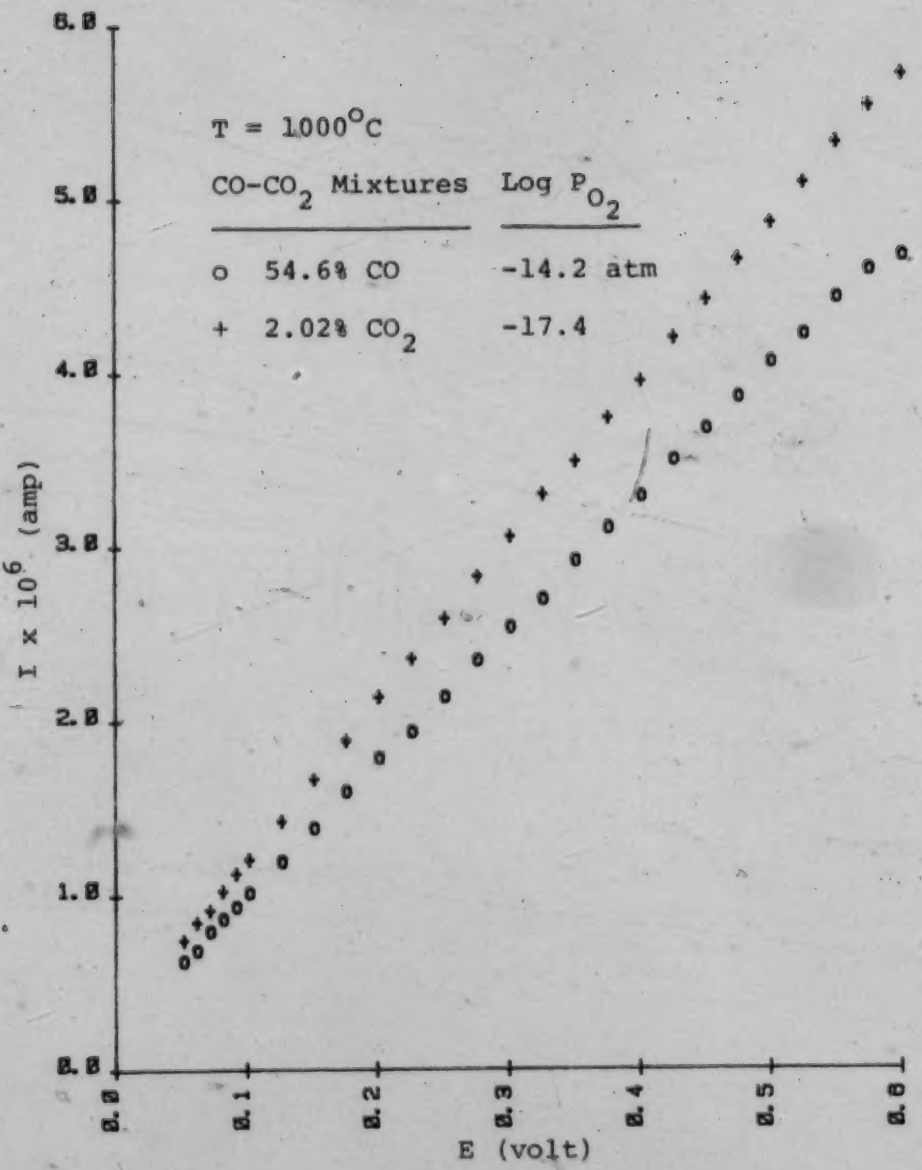

Figure 56. Current - applied potential curves for $MnAl_2O_4$ at 1000°C.

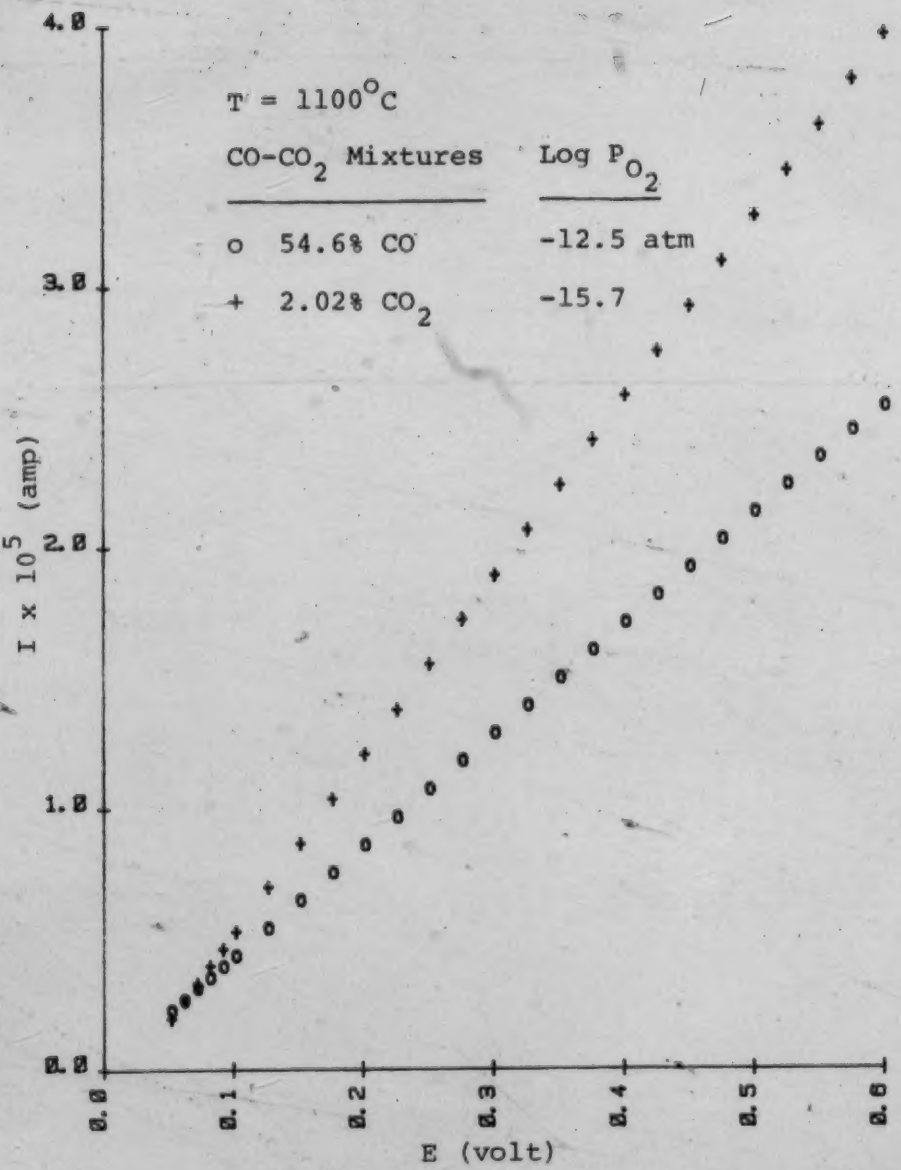

Figure 57. Current - applied potential curves for $MnAl_2O_4$ at 1100°C.

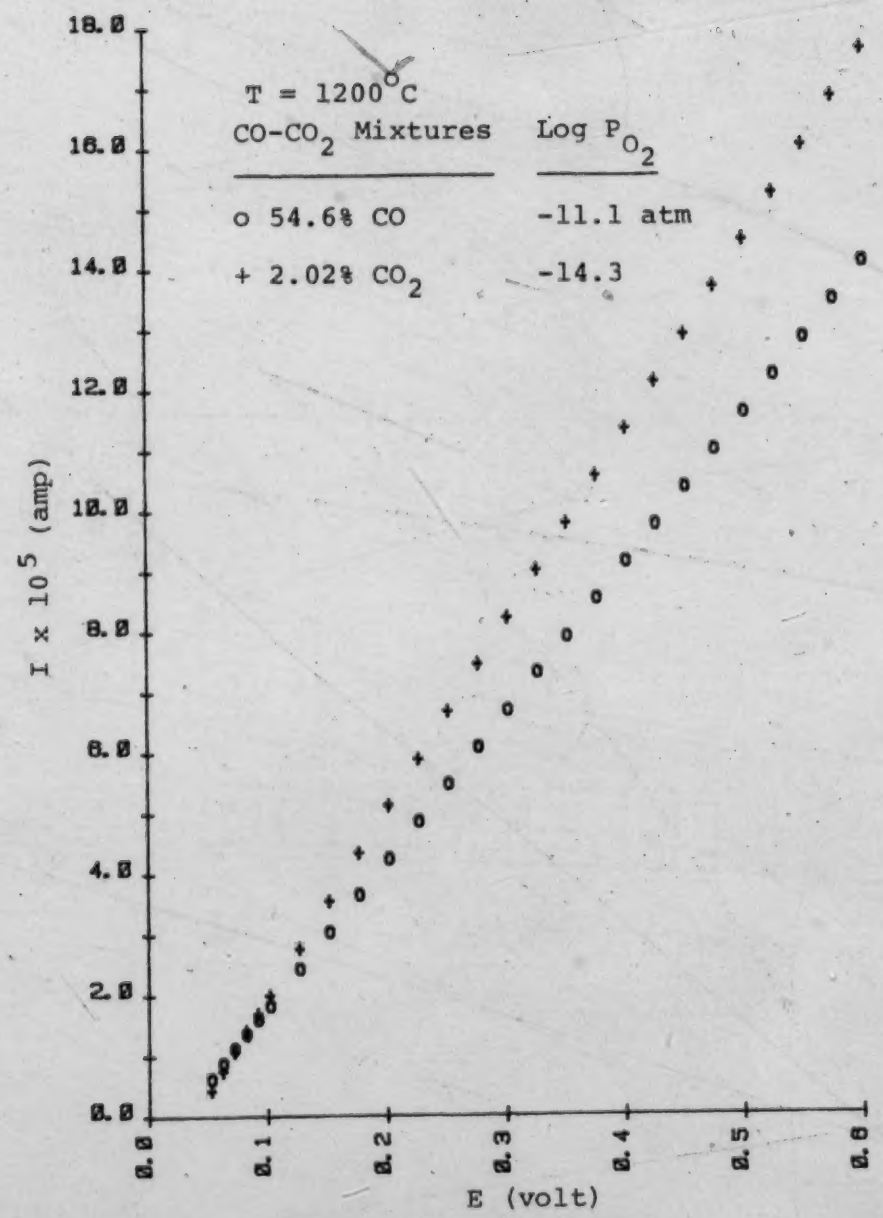

Figure 58. Current - applied potential curves for $MnAl_2O_4$ at 1200°C.

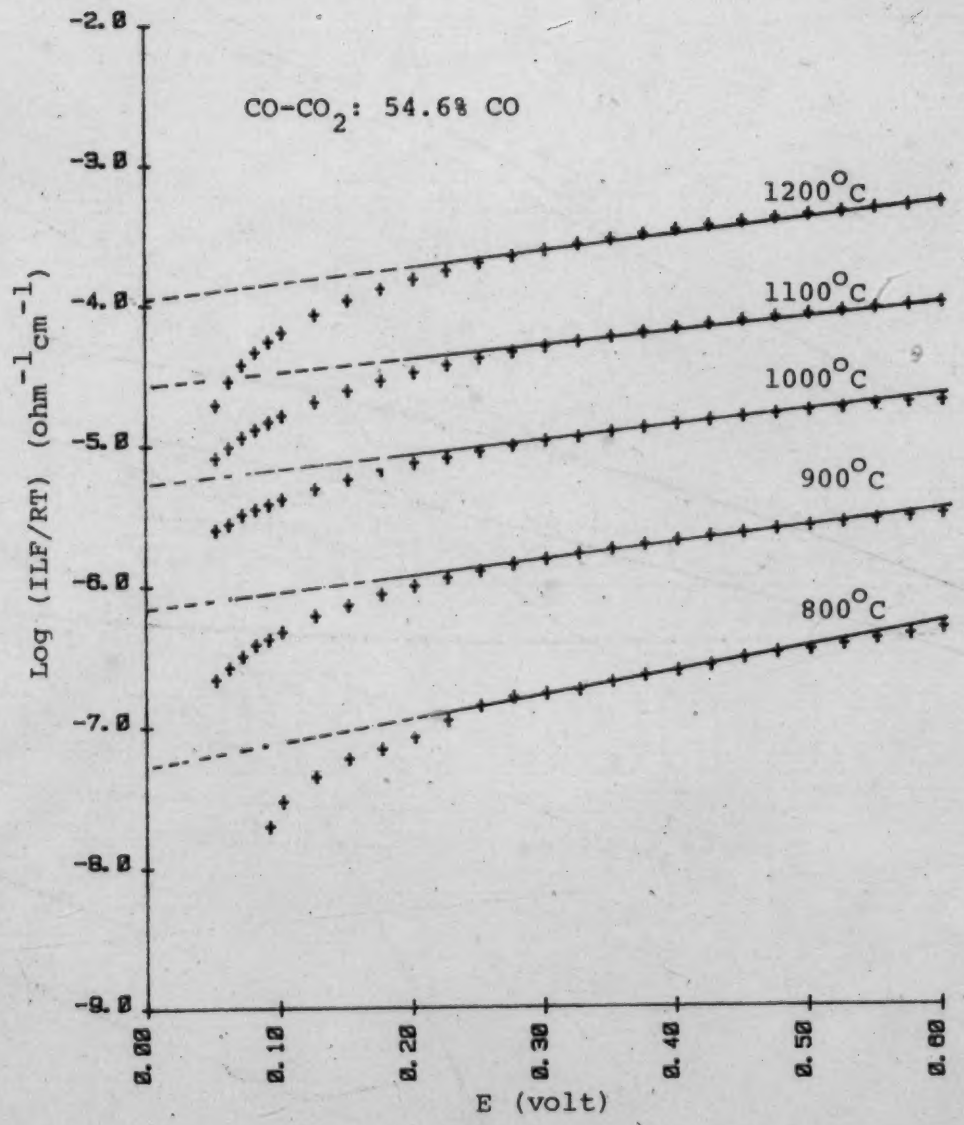

Figure 59. Logarithmic current - potential plots for $MnAl_2O_4$ ($CO-CO_2$: 54.6% CO).

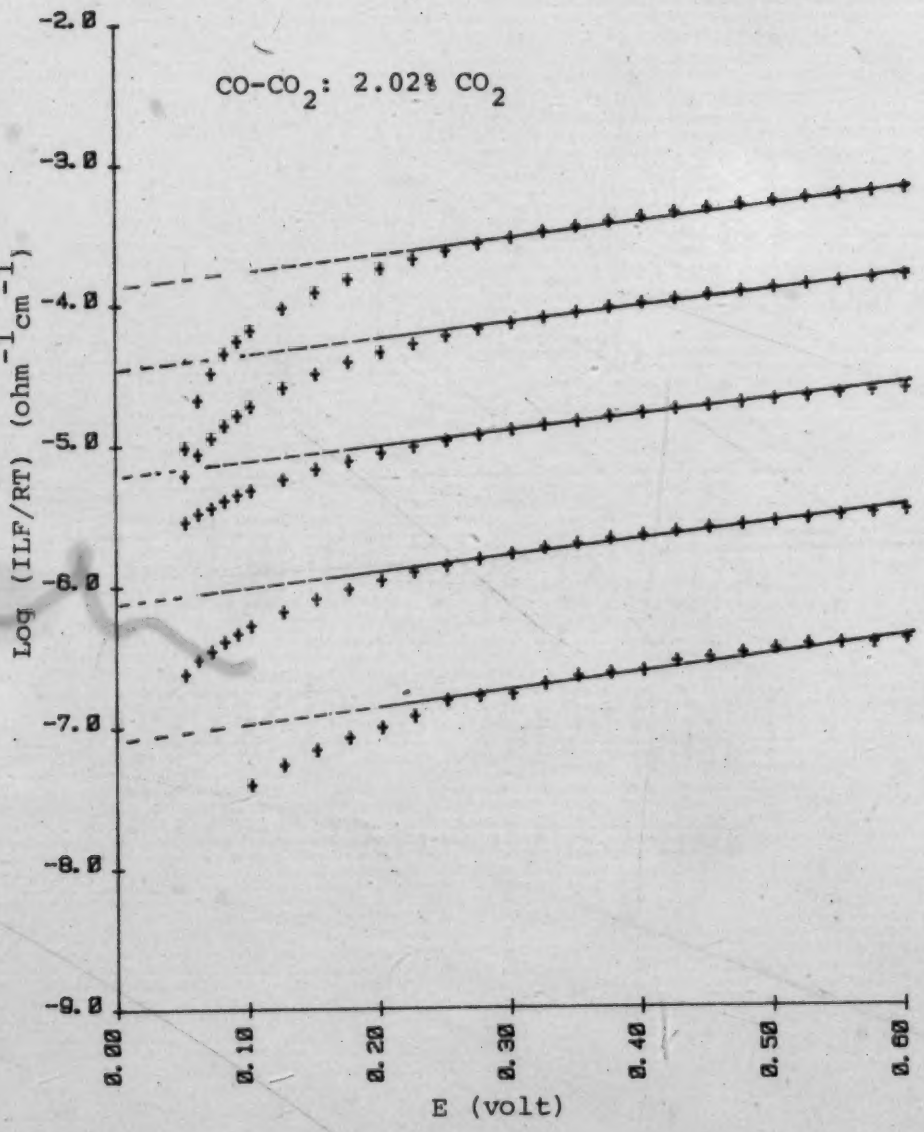

Figure 60. Logarithmic current - potential plots for $MnAl_2O_4$ ($CO-CO_2$: 2.02% CO_2).

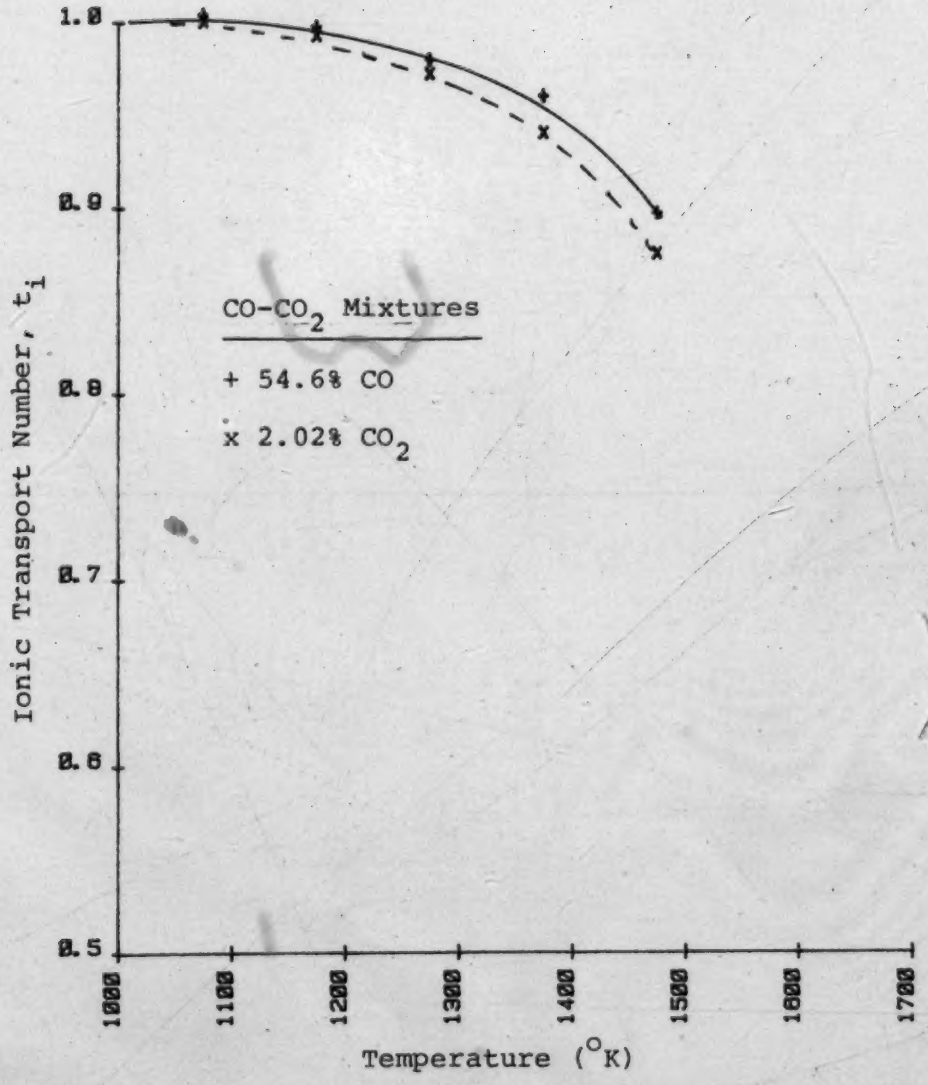

Figure 61. Ionic transport number - temperature plots for $MnAl_2O_4$ (DC Polarization Measurements).

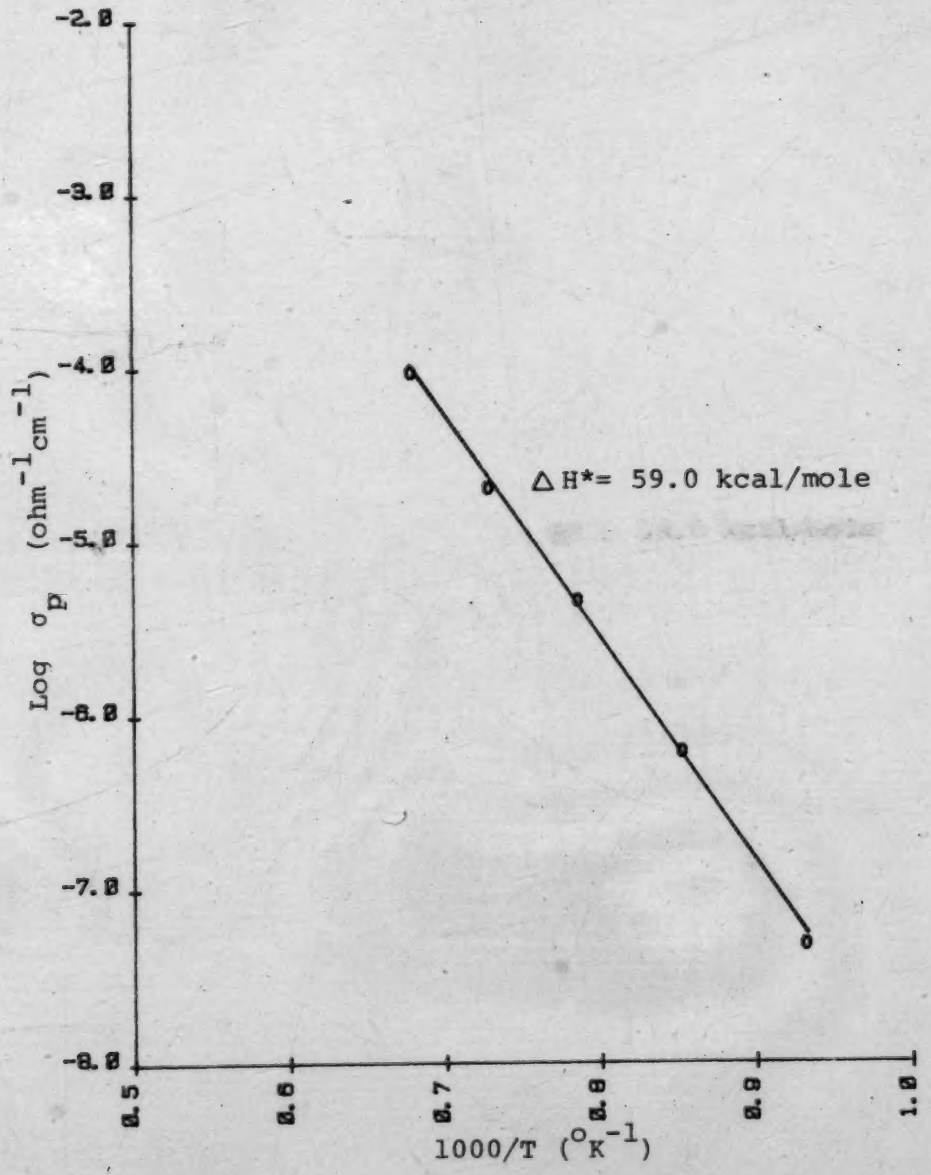

Figure 62. Arrhenius plot of the p-type conductivity of $MnAl_2O_4$ ($CO-CO_2$: 54.6% CO, DC Polarization Measurements).

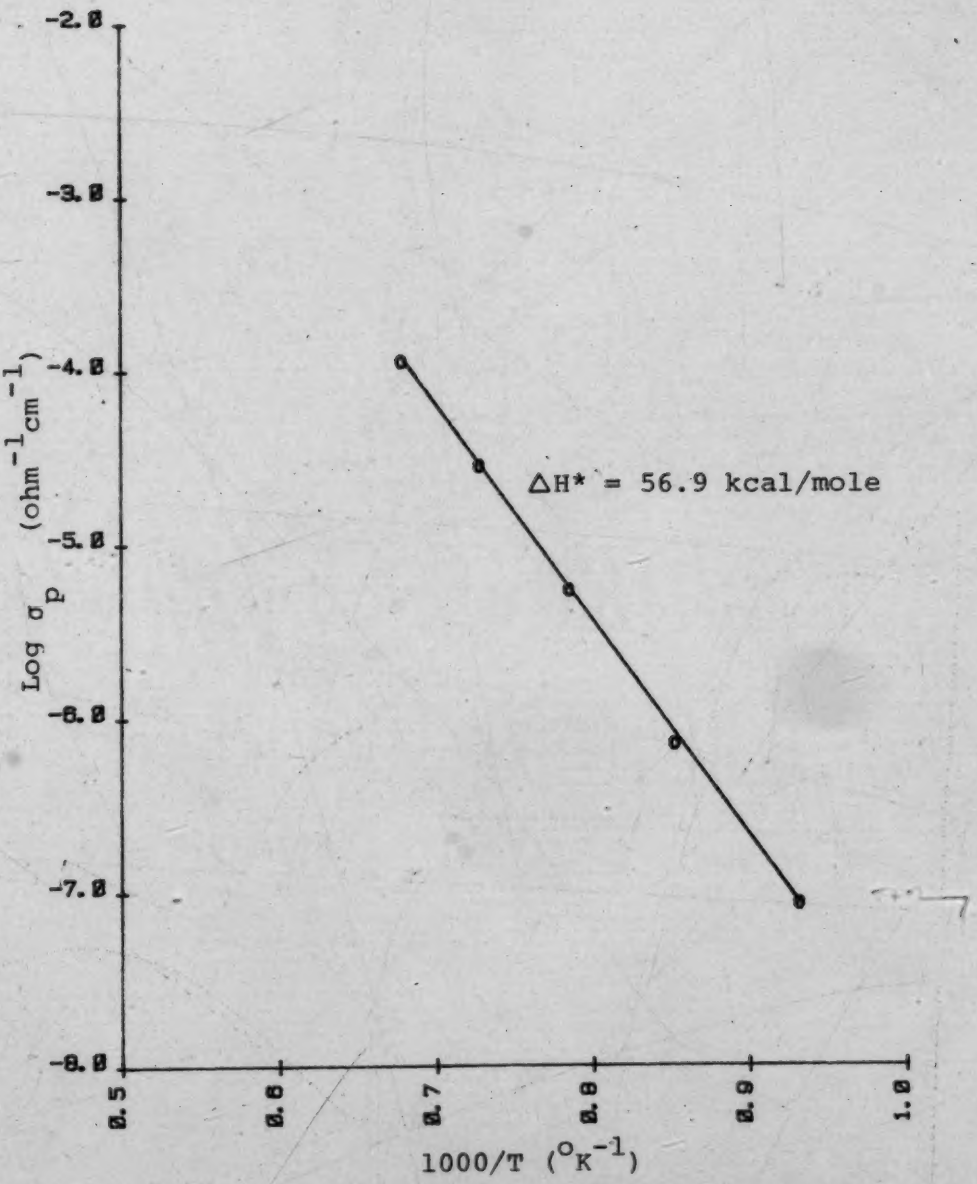

Figure 63. Arrhenius plot of the p-type conductivity of $MnAl_2O_4$ (CO-CO_2: 2.02% CO_2, DC Polarization Measurements).

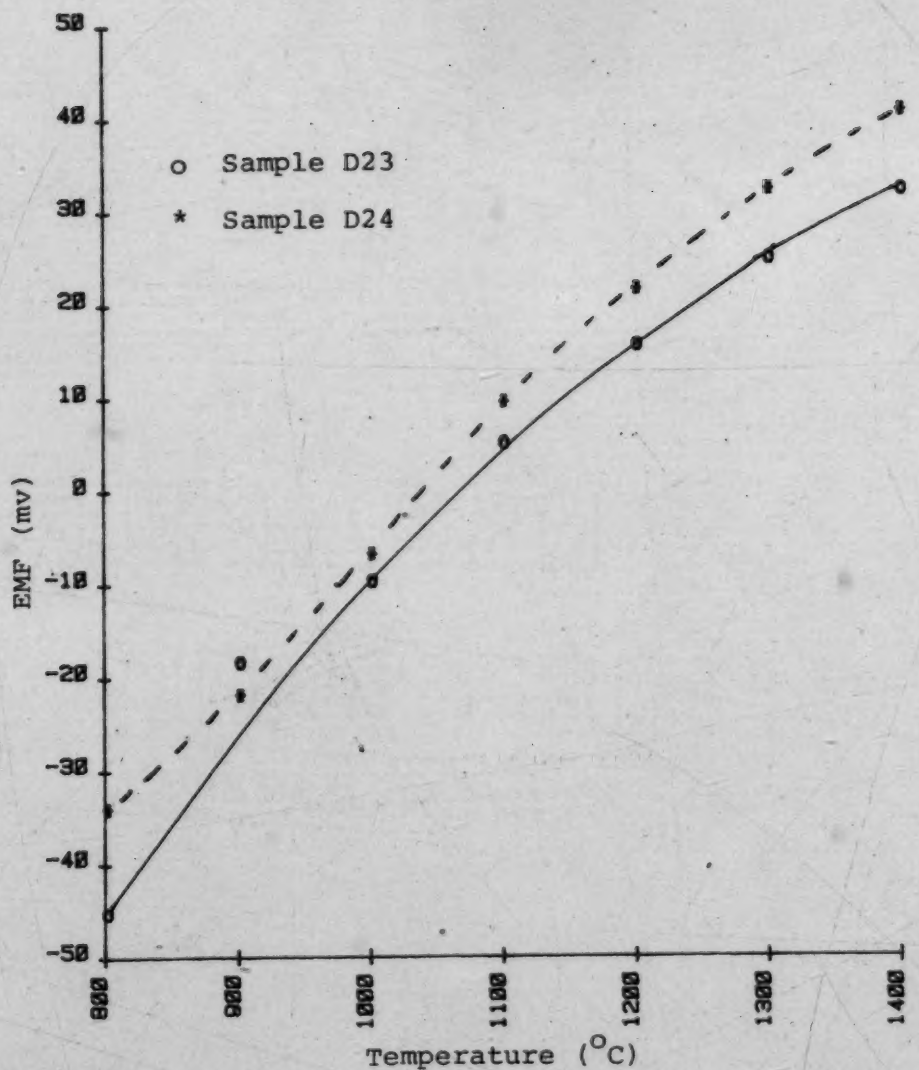

Figure 64. Emf - temperature plots for $MnAl_2O_4$ (Emf Measurements).

Tables

Table 1. Self-diffusion in Oxide Systems

Oxide	D_o (cm^2/sec)	Q (kcal/mole)	Ref.
Mn in MnO		40	116
Ni in NiO	1.7×10^{-3}	56	62
Ni in NiO	4.4×10^{-4}	44.2	115
O in NiO	1.0×10^{-5}	54	73
Fe in Fe_2O_3	4×10^{5}	112	55
Cr in Cr_2O_3	4×10^{3}	100	60
Al in Al_2O_3	28	114	71
Al in Al_2O_3	2	110	79
O in Al_2O_3†	1.9×10^{3}	152	79
O in Al_2O_3†	6.4×10^{5}	188	80
O in ZrO_2-15% CaO	0.018	31.2	76
Zn in $ZnAl_2O_4$	2.5×10^{2}	78	60
Ni in $NiAl_2O_4$	3×10^{-4}	55	61
Ni in $NiAl_2O_4$	2.9×10^{-5}	53.3	63
Cr in $NiAl_2O_4$	1.17×10^{-3}	50	65
Mg in $MgAl_2O_4$	2×10^{2}	86	63
Co in $CoAl_2O_4$	8	85	67
Fe in $FeAl_2O_4$	0.38	65.1	69
Fe in $FeAl_2O_4$†	1.02	62.2	69
Ni in $NiCr_2O_4$	0.85	75	60
Ni in $NiCr_2O_4$	1.5×10^{-3}	61.4	63
Cr in $NiCr_2O_4$	0.75	73	60
Cr in $NiCr_2O_4$	2	100	67
O in $NiCr_2O_4$	0.017	65.4	77

---

†Single crystal

Table 2. Equilibrium Oxygen Partial Pressures of Reversible Electrodes at 1000°C [158]

Reversible Electrode	Log $P(O_2)$ (atm)
Cu_2O-CuO	- 0.87
Fe_2O_3-Fe_3O_4	- 5.47
Cu-Cu_2O	- 6.24
Ni-NiO	-10.30
Co-CoO	-11.89
Fe-FeO	-14.84
Mo-MoO_2	-14.86
Cr-Cr_2O_3	-21.80
Mn-MnO	-23.90
Nb-NbO	-25.10
V-VO	-27.50

Table 3. Thermodynamic Stability Limit of $NiAl_2O_4$

Temperature (°C)	Lower Limit Log $P(O_2)$ (atm)
1073	-15.13
1173	-13.05
1273	-11.30
1373	- 9.80
1473	- 8.50
1573	- 7.37
1673	- 6.38

Table 4. Thermodynamic Stability Limits of $MnAl_2O_4$.

Temperature (°K)	Upper Limit Log $P(O_2)$ (atm)	Lower Limit Log $P(O_2)$ (atm)
1073	-0.97	-32.87
1173	-0.07	-29.36
1273	0.69	-26.41
1373	1.34	-23.88
1473	1.90	-21.70
1573	2.40	-19.80
1673	2.83	-18.12

Table 5. Conductivity Data For $NiAl_2O_4$ (Sample B4)

Temperature (°C)	Log $P(O_2)$ (atm)	Log σ ($ohm^{-1}cm^{-1}$)
800	-29.20	-5.79
	-27.33	-5.80
	-24.36	-5.80
	-21.80	-5.80
	-18.58	-5.80
	-15.03	-5.80
	-12.42	-5.81
	- 5.88	-5.80
	- 4.03	-5.80
	- 2.97	-5.80
	- 2.03	-5.80
	- 0.01	-5.80
900	-27.15	-5.50
	-24.99	-5.51
	-22.02	-5.52
	-19.45	-5.54
	-16.24	-5.55
	-12.68	-5.55
	-10.07	-5.54
	- 5.88	-5.51
	- 4.03	-5.50
	- 2.97	-5.50
	- 2.03	-5.49
	- 0.01	-5.49
1000	-25.43	-4.96
	-23.01	-4.97
	-20.04	-4.99
	-17.48	-5.03
	-14.26	-5.06
	-10.71	-5.07
	- 8.10	-5.04
	- 5.88	-5.00
	- 4.03	-4.99
	- 2.97	-4.98
	- 2.03	-4.97
	- 0.01	-4.94
1100	-21.32	-4.58
	-18.36	-4.53
	-15.79	-4.52
	-12.57	-4.51
	- 9.02	-4.50
	- 6.41	-4.47
	- 5.88	-4.43
	- 4.03	-4.42

- 2.97	-4.41
- 2.03	-4.39
- 0.01	-4.35

Table 6. Conductivity Data For $NiAl_2O_4$ (Sample B6)

Temperature (°C)	Log $P(O_2)$ (atm)	Log σ ($ohm^{-1}cm^{-1}$)
800	-15.03	-5.85
	-12.42	-5.85
	- 5.88	-5.84
	- 4.03	-5.84
	- 2.97	-5.84
	- 2.03	-5.84
	- 0.01	-5.84
900	-12.68	-5.52
	-10.07	-5.52
	- 5.88	-5.51
	- 4.03	-5.51
	- 2.97	-5.50
	- 2.03	-5.51
	- 0.01	-5.49
1000	-10.71	-5.02
	- 8.10	-4.98
	- 5.88	-4.97
	- 4.03	-4.97
	- 2.97	-4.96
	- 2.03	-4.95
	- 0.01	-4.94
1100	- 9.02	-4.44
	- 6.41	-4.40
	- 5.88	-4.38
	- 4.03	-4.37
	- 2.97	-4.37
	- 2.03	-4.37
	- 0.01	-4.35
1200	- 7.56	-3.84
	- 5.88	-3.84
	- 4.03	-3.83
	- 2.97	-3.82
	- 2.03	-3.80
	- 0.01	-3.77
1300	- 6.29	-3.33
	- 5.88	-3.33
	- 4.03	-3.32
	- 2.97	-3.31
	- 2.03	-3.30
	- 0.01	-3.28
1400	- 5.88	-2.92

- 5.14	-2.93
- 4.03	-2.91
- 2.97	-2.91
- 2.03	-2.90
- 0.01	-2.87

Table 7. Conductivity Data For $NiAl_2O_4$ (Reversible Electrodes)

Temperature (°C)	Log $P(O_2)$ (atm)	Log σ ($ohm^{-1}cm^{-1}$)
800	-34.09	-5.80
	-29.88	-5.78
	-19.25	-5.78
	-18.96	-5.84
	-15.38	-5.95
	-13.91	-5.73
	- 9.59	-5.82
	- 8.83	-5.80
	- 2.95	-5.80
900	-30.52	-5.46
	-27.91	-5.59
	-26.67	-5.75
	-16.85	-5.37
	-16.76	-5.63
	-13.44	-5.65
	-11.97	-5.76
	- 7.52	-5.68
	- 7.45	-5.39
	- 1.84	-5.43
1000	-27.50	-4.93
	-25.09	-5.03
	-23.97	-5.19
	-14.91	-5.12
	-14.83	-4.85
	-11.80	-4.99
	-10.33	-5.14
	- 6.28	-4.87
	- 5.77	-5.38
	- 0.91	-5.00
1100	-24.93	-4.30
	-22.68	-4.50
	-21.65	-4.45
	-13.32	-4.59
	-13.10	-4.32
	-10.41	-4.34
	- 8.92	-4.40
	- 4.28	-4.83
	- 0.13	-4.33
1200	-22.70	-3.77
	-20.61	-4.01
	-19.66	-3.81
	-11.96	-4.12

	-11.61	-3.80
	- 9.20	-3.79
	- 7.71	-3.87
	- 2.99	-3.93
1300	-20.76	-3.26
	-18.81	-3.57
	-17.91	-3.16
	-10.76	-3.59
	-10.32	-3.31
	- 8.14	-3.27
	- 6.66	-3.34
	- 1.87	-3.34
1400	-19.05	-2.84
	-17.23	-3.23
	-16.38	-2.73
	- 9.71	-2.87
	- 9.18	-2.94
	- 7.21	-2.84
	- 5.73	-2.89
	- 0.88	-2.88

Table 8. P-type Conductivity Data For $NiAl_2O_4$ (DC Polarization Measurements)

Temperature (°C)	Log $P(O_2)$ (atm)	Log σ_p ($ohm^{-1}cm^{-1}$)
800	- 5.88	-7.23
900		-6.08
1000		-5.36
1100		-4.71
1200		-4.09
1300		-3.57
1400		-3.16
800	-15.03	-7.40
900	-12.68	-6.55
1000	-10.71	-5.59
1100	- 9.02	-4.78
1200	- 7.56	-4.13
1300	- 6.29	-3.53
1400	- 5.17	-3.15

Table 9. Emf - Temperature Data For $NiAl_2O_4$ (Emf Measurements, $P(O_2)=0.21$ atm)

Temperature (°C)	Sample B31 Emf (mv)	Sample B32 Emf (mv)
800	150.60	173.30
900	101.30	121.70
1000	37.04	52.82
1100	7.81	11.01
1200	4.08	6.87
1300	7.02	8.69
1400	8.26	7.24

Table 10. Conductivity Data For $MnAl_2O_4$ (Sample D10)

Temperature (°C)	Log $P(O_2)$ (atm)	Log σ ($ohm^{-1}cm^{-1}$)
800	-27.33	-4.12
	-24.36	-4.12
	-21.80	-4.11
	-18.58	-4.10
	-15.03	-4.08
	-12.42	-4.07
	- 5.88	-4.07
	- 4.03	-4.03
	- 2.97	-4.02
	- 2.03	-4.01
	- 0.01	-3.54
900	-24.99	-3.80
	-22.02	-3.80
	-19.45	-3.84
	-16.24	-3.98
	-12.68	-3.92
	-10.07	-3.78
	- 5.88	-3.83
	- 4.03	-3.61
	- 2.97	-3.60
	- 2.03	-3.59
	- 0.01	-3.36
1000	-23.01	-2.88
	-20.04	-2.80
	-17.48	-3.05
	-14.26	-3.51
	-10.71	-3.57
	- 8.10	-3.42
	- 5.88	-3.42
	- 4.03	-3.27
	- 2.97	-3.24
	- 2.03	-3.18
	- 0.01	-2.92

Table 11. Conductivity Data For $MnAl_2O_4$ (Sample D2)

Temperature (°C)	Log $P(O_2)$ (atm)	Log σ ($ohm^{-1}cm^{-1}$)
800	-27.33	-4.59
	-24.36	-4.61
	-21.80	-4.62
	-18.58	-4.61
	-15.03	-4.51
	-12.42	-4.44
	- 5.88	-4.36
900	-24.99	-4.10
	-22.02	-4.09
	-19.45	-4.15
	-16.24	-4.22
	-12.68	-4.06
	-10.07	-3.90
	- 5.88	-3.84
1000	-23.01	-3.65
	-20.04	-3.62
	-17.48	-3.75
	-14.26	-3.78
	-10.71	-3.59
	- 8.10	-3.41
	- 5.88	-3.36
1100	-21.32	-3.31
	-18.36	-3.37
	-15.79	-3.42
	-12.57	-3.43
	- 9.02	-3.26
	- 6.41	-3.13
	- 5.88	-3.12

Table 12. Conductivity Data For $MnAl_2O_4$ (Reversible Electrodes)

Temperature (°C)	Log $P(O_2)$ (atm)	Log σ ($ohm^{-1}cm^{-1}$)
800	-34.09	-4.09
	-31.26	-4.49
	-29.88	-5.16
	-19.25	-5.13
	-18.96	-4.79
	-15.38	-4.89
	-13.91	-4.45
	- 9.59	-3.71
	- 8.83	-3.97
	- 2.95	-4.09
900	-30.52	-3.73
	-27.91	-4.28
	-26.67	-4.53
	-16.85	-4.82
	-16.76	-4.32
	-13.44	-4.36
	-11.97	-3.89
	- 7.52	-3.29
	- 7.45	-3.53
	- 1.84	-3.66
1000	-27.50	-3.31
	-25.09	-4.20
	-23.97	-4.09
	-14.91	-3.86
	-14.83	-4.41
	-11.80	-3.86
	-10.33	-3.44
	- 6.28	-3.17
	- 5.77	-2.93
	- 0.91	-3.35
1100	-24.93	-2.98
	-22.69	-4.01
	-21.65	-4.00
	-13.32	-3.50
	-13.10	-3.98
	-10.41	-3.40
	- 8.92	-3.06
	- 4.28	-2.62
1200	-22.70	-2.75
	-20.61	-3.28
	-19.66	-3.42
	-11.96	-3.27

	-11.61	-3.42
	- 9.20	-3.02
	- 7.71	-2.74
	- 2.99	-2.34
1300	-20.76	-2.65
	-18.81	-3.11
	-17.91	-2.92
	-10.76	-2.81
	-10.32	-2.98
	- 8.14	-2.66
	- 6.66	-2.43
	- 1.87	-2.10
1400	-19.05	-2.51
	-17.23	-2.93
	-16.38	-2.49
	- 9.71	-2.37
	- 9.18	-2.63
	- 7.21	-2.41
	- 5.73	-2.19
	- 0.88	-1.92

Table 13. P-type Conductivity Data For $MnAl_2O_4$ (DC Polarization Measurements)

Temperature (°C)	Log $P(O_2)$ (atm)	Log σ_p ($ohm^{-1}cm^{-1}$)
800	-18.58	-7.28
900	-16.24	-6.17
1000	-14.26	-5.30
1100	-12.57	-4.65
1200	-11.11	-3.99
800	-21.80	-7.03
900	-19.45	-6.11
1000	-17.48	-5.22
1100	-15.79	-4.51
1200	-14.33	-3.91

Table 14. Emf - Temperature Data For $MnAl_2O_4$ (Emf Measurements)

Temperature (°C)	Log $P(O_2)$ (atm)	Sample D23 Emf (mv)	Sample D24 Emf (mv)
800	-21.80	-45.81	-35.07
900	-19.45	-18.91	-22.90
1000	-17.48	-10.20	- 7.80
1100	-15.79	4.60	8.50
1200	-14.33	15.10	20.60
1300	-13.06	24.40	31.31
1400	-11.94	31.71	39.68

Plate

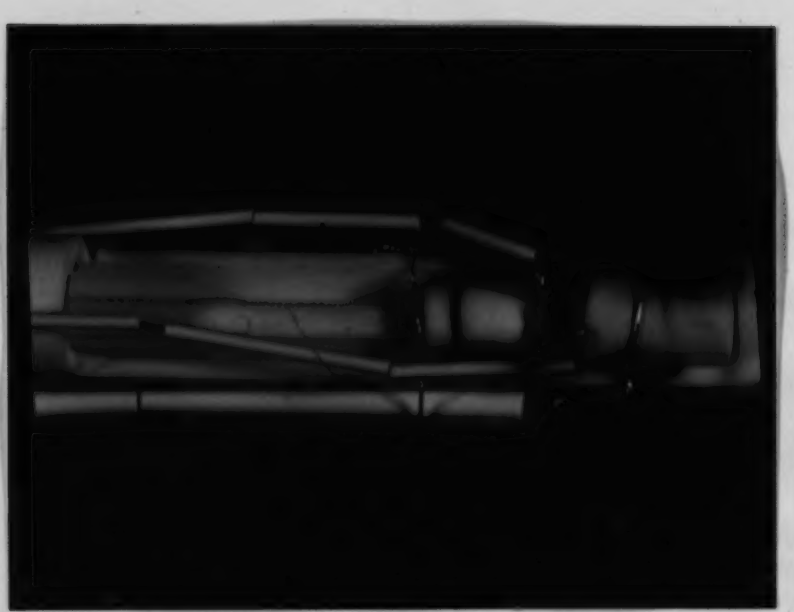

Plate 1. Two-probe conductivity cell holder

Bibliography

1. W. Nernst, *Z. Elektrochem.*, 6, 41 (1899)

2. F. Haber and S. Tolloczko, *Z. Anorg. Chem.*, 41, 407 (1904)

3. C. Tubandt and E. Lorenz, *Z. Physik. Chem.*, 87, 513 (1914)

4. K. Kiukkola and C. Wagner, *J. Electrochem. Soc.*, 104, 308 (1957)

5. K. Kiukkola and C. Wagner, *J. Electrochem. Soc.*, 104, 379 (1957)

6. J. N. Bradley and P. D. Greene, *Trans. Faraday Soc.*, 62, 2069 (1966)

7. B. B. Owens and G. R. Angue, *Science*, 157, 308 (1967)

8. R. A. Rapp in "Thermodynamics of Nuclear Materials," p. 559, IAEA, Vienna (1968)

9. N. M. Tallan and R. W. Vest, *J. Am. Ceram. Soc.*, 49, 401 (1966)

10. H. L. Tuller and A. S. Nowick, *J. Electrochem. Soc.*, 122, (1975)

11. R. M. Blumenthal, J. Coburn, J. Baukus and W. N. Hirthe, *J. Phys. Chem. Solids*, 27, 643 (1966)

12. J. Yee and F. A. Kroger, *J. Am. Ceram. Soc.*, 56, 189 (1973)

13. Y. F. Yao and J. T. Kummer, *J. Inorg. Chem.*, 29, 2453 (1967)

14. H. K. Bowen in "Conference on High Temperature Services Related to Open-Cycle Coal-Fired MHD Systems," p. 131, Tech. Report No. ANL 77-21 (1977)

15. T. O. Mason, W. Petuskey, W. W. Liang, J. W. Halloran, F. Yen, T. M. Pollack, J. F. Elliot and H. K. Bowen in "Proceedings of the 6th International Conference on MHD Electrical Power Generation," Vol. V (1975)

16. J. E. Fenstermacher, Jr. , L. R. White and R. R. Smyth in "Conference on High Temperature Services Related to Open-Cycle Coal-Fired MHD Systems," p.114, Tech. Report No. ANL 77-21 (1977)

17. W. H. Bragg, *Phil. Mag.*, 30, 305 (1915)

18. S. Nishikawa, *Proc. Math. Phys. Soc. Tokyo*, 8, 199 (1915)

19. F. W. Barth and E. Posnjak, *Z. Krist.*, 82, 325 (1932)

20. E. J. W. Verwey and E. L. Heilmann, *J. Chem. Phys.*, 15, 174 (1947)

21. F. C. Romeijn, *Philips Res. Rep.*, 8, 304 (1953)

22. F. Bertaut, *Compt. Rend.*, 230, 213 (1950)

23. J. T. Richardson, *J. Appl. Phys.*, 35, 664 (1964)

24. S. Greenwald, S. J. Pickart and F. H. Grannis, *J. Chem. Phys.*, 22, 1597 (1954)

25. H. Schmalzried, *Z. Physik. Chem.*, 28, 203 (1961)

26. R. K. Datta and R. Roy, *J. Am. Ceram. Soc.*, 50 578 (1967)

27. J. T. Richardson and W. O. Milligan, *J. Phys. Chem.*,

60, 1223 (1956)

28. J. T. Richardson and L. W. Vernon, *J. Phys. Chem.*, 62, 1153 (1958)

29. K. P. Sinha and A. P. B. Sinha, *J. Phys. Chem.*, 61, 758 (1957)

30. P. L. Edwards, *Phys. Rev.*, 116, 294 (1959)

31. R. Stahl-Brada and W. Low, *Phys. Rev.*, 116, 561 (1959)

32. E. Brun, S. Hafner, P. Hartmann and F. Laves, *Naturwissenschaften*, 47, 277 (1960)

33. H. Schmalzried, *Naturwissenschaften*, 47, 466 (1960)

34. R. J. Datta and R. Roy, *Nature*, 191, 169 (1961)

35. R. J. Datta and R. Roy in "The Encyclopedia of X-rays and Gamma Rays", p. 1018, G. L. Clark, Editor, Reinhold Publishing Corp., New York (1963)

36. R. P. Cooley and J. Reed, *J. Am. Ceram. Soc.*, 55, 395 (1972)

37. N. W. Grimes, R. J. Hilleard, J. Waters and J. Yerkess, *Proc. Phys. Soc., London*, 1, 663 (1968)

38. H. Furuhashi, M. Inagaki and S. Naka, *J. Inorg. Nucl. Chem.*, 35, 3009 (1973)

39. O. Schmitz-DuMont, A. Lule and D. Reinen, *Ber. Bunsenges. Physik. Chem.*, 69, 76 (1965)

40. F. S. Stone, *Bull. Soc. Chim. Fr.*, 12, 819 (1966)

41. W. L. Roth, *J. de Physique*, 25, 507 (1964)

42. P. Cossee and A. E. van Arkel, *J. Phys. Chem. Solids*, 15, 1 (1960)

43. K. Miyatani, K. Kohn, S. Iida and H. Kamimura, *J. Phys. Soc. Japan*, 20, 471 (1965)

44. K. Miyatani, K. Kohn and H. Kamimura, *J. Phys. Soc., Japan*, 21, 464 (1966)

45. H. Kamimura, *J. Phys. Soc., Japan*, 21, 484 (1966)

46. T. Mizoguchi and M. Tanaka, *J. Phys. Soc., Japan*, 18, 1301 (1963)

47. G. A. Slack, *Phys. Rev.*, 134, A1268 (1964)

48. F. De Boer, J. H. Santen and E. J. W. Verwey, *J. Chem. Phys.*, 16, 1091 (1948)

49. F. De Boer, J. H. Santen and E. J. W. Verwey, *J. Chem. Phys.*, 18, 1032 (1950)

50. A. Miller, *J. Appl. Phys.*, 30, 245 (1959)

51. D. S. McClure, *J. Phys. Chem. Solids*, 3, 311 (1957)

52. J. D. Dunitz and L. E. Orgel, *J. Phys. Chem. Solids*, 3, 318 (1957)

53. A. Navortsky and O. J. Kleppa, *J. Inorg. Nucl. Chem.*, 29, 2701 (1967)

54. E. W. Gorter, *Philips Res. Rep.*, 9, 295 (1954)

55. G. Blasse, *Philips Res. Rep.*, 19, 1 (1964)

56. R. Lindner, *Arkiv Kemi*, 4, 381 (1952)

57. R. Lindner, *Arkiv Kemi*, 4, 385 (1952)

58. J. A. Hedvall, C. Brisi and R. Lindner, *Arkiv Kemi*, 4, 377 (1952)

59. R. Lindner, *J. Chem. Phys.*, 23, 410 (1955)

60. R. Lindner, *Z. Elecktrochem.*, 59, 967 (1955)

61. R. Lindner, *Z. Naturforsch.*, 10A, 1027 (1955)

62. R. Lindner and A. Akerstrom, *Z. Physik. Chem. (Frankfurt)*, 6, 162 (1956)

63. R. Lindner and A. Akerstrom, *Disc. Farad. Soc.*, 23, 133 (1957)

64. R. Lindner and A. Akerstrom, *Z. Physik. Chem. (Frankfurt)*, 18, 303 (1958)

65. C. Wagner, *Z. Physik. Chem.*, B34, 309 (1936)

66. I. N. Belokurova and D. V. Ignatov, *Sov. J. At. Energy*, 4, 399 (1958)

67. R. Sun, *J. Chem. Phys.*, 28, 290 (1958)

68. A. Morkel and H. Schmalzried, *Z. Physik. Chem.*, 32, 76 (1962)

69. H. Schmalzried in "Progress in Solid-State Chemistry", Vol. 2, p. 265, H. Reiss, Editor, Pergamon Press, Oxford (1965)

70. J. W. Halloran and H. K. Bowen, *J. Am. Ceram. Soc.*, 63, 58 (1980)

71. G. Yamaguchi, M. Nakano and M. Tosaki, *Bull. Chem. Soc., Japan*, 42, 2801 (1969)

72. A. E. Paladino and W. D. Kingery, *J. Chem. Phys.*, 37, 957 (1962)

73. W. J. Moore, Y. Ebisuzaki and J. A. Sluss, *J. Phys. Chem.*, 62, 1438 (1958)

74. M. O'Keeffe and W. J. Moore, *J. Phys. Chem.*, 65, 1438 (1961)

75. R. Haul and D. Just, *J. Appl. Phys., Suppl.*, 33, 487 (1962)

76. R. Haul and G. Dumbgen, *J. Phys. Chem. Solids*, 26, 1 (1965)

77. L. A. Simpson and R. E. Carter, *J. Am. Ceram. Soc.*, 49, 139 (1966)

78. W. D. Kingery, D. C. Hill and R. P. Nelson, *J. Am. Ceram. Soc.*, *43*, 473 (1960)

79. H. M. O'Bryan, Jr. and F. V. DiMarcello, *J. Am. Ceram. Soc.*, 53, 413 (1970)

80. Y. Oishi and W. D. Kingery, *J. Chem. Phys.*, 33, 480 (1960)

81. D. J. Reed and B. J. Wuensch, *J. Am. Ceram. Soc.*, 63, 88 (1980)

82. J. A. Hedvall and L. Leffler, *Z. Anorg. Allgem. Chem.*, 234, 235 (1937)

83. K. Hauffe and K. Pschera, *Z. Anorg. Chem.*, 262, 147 (1950)

84. W. A. Fischer and A. Hoffmann, *Naturwissenschaften*, 41, 162 (1954)

85. A. Hoffmann and W. A. Fischer, *Z. Physik. Chem. (N. F.)*, 7, 80 (1956)

86. H. Schmalzried, *Z. Physik. Chem.*, 33, 111 (1962)

87. C. I. Helgesson, *Trans. Chalmers Univ. Technol., Gothenburg*, 298, 8 (1964)

88. C. Greskovich, *J. Am. Ceram. Soc.*, 53, 498 (1970)

89. A. D. Pelton, H. Schmalzried and C. D. Greskovich, *Ber. Bunsenges. Physik. Chem.*, 76, 543 (1972)

90. J. Hlavac in "Reactivity of Solids", p. 129, J. De Boer, Editor, Elsevier, Amsterdam (1961)

91. V. S. Stubican and R. Roy, *J. Phys. Chem. Solids*, 26, 1293 (1965)

92. R. E. Carter, *J. Am. Ceram. Soc.*, 44, 116 (1961)

93. L. Navias, *J. Am. Ceram. Soc.*, 44, 434 (1961)

94. L. Navias, *J. Am. Ceram. Soc.*, 45, 544 (1962)

95. L. Navias, *J. Am. Ceram. Soc.*, 46, 152 (1963)

96. R. C.Rossi and R. M. Fulrath, *J. Am. Ceram. Soc.*, 46, 145 (1963)

97. J. J. Comer, M. C. Tombs and J. F. Fitzgerald, *J. Am. Ceram. Soc.*, 49, 237 (1966)

98. D. L. Branson, *J. Am. Ceram. Soc.*, 48, 591 (1965)

99. Y. Iida and K. Shimada, *Nagoya Kogyo Gijutsu Shikenjo*, 8, 23 (1959)

100. Y. Iida, K. Shimada and S. Ozaki, *Nagoya Kogyo Gijutsu Shikenjo*, 8, 829 (1959)

101. Y. Iida, K. Shimada and S. Ozaki, *Nagoya Kogyo Gijutsu Shikenjo*, 9, 18 (1960)

102. H. Schmalzried and W. Rogalla, *Naturwissenschaften*, 50, 593 (1963)

103. F. S. Pettit, E. H. Randklev and E. J. Felten, *J. Am. Ceram. Soc.*, 49, 199 (1966)

104. J. Macak and B. Koutsky, *Collect. Czech. Chem. Commun.*, 38, 2561 (1973)

105. K. Kohn, *Waseda Daigaku Rikogaku Kenkyusho Hokoku*, 65, 49 (1974)

106. W. J. Minford and V. S. Stubican, *J. Am. Ceram. Soc.*, 57, 363 (1974)

107. H. G. Sockel and H. Schmalzried in "Materials Science Research", Vol. 3, p. 61, H. Palmour, Editor, Plenum Press, New York (1966)

108. F. S. Stone and R. J. D. Tilley in "Reactivity of Solids", p. 583, G. M. Schwab, Editor, Elsevier, Amsterdam (1965)

109. A. S. Tumarev, L. A. Panyushin and A. V. Tuts, *Izv. Vysshikh. Uchebn. Zavedenii, Chernaya Met.*, 6, 26 (1963)

110. V. P. Ivanov and L. V. Koroleva, *Russ. J. Phys. Chem.*, 50, 383 (1976)

111. L. G. Simonova , V. A. Dzis'ko, M. S. Borisova, L. G. Karakchiev and I. P. Olenkova, *Kinetics and Catalysis*, 14, 1380 (1973)

112. G. Rienacker, H. H. Plagemann and H. Latka, *Acta Chim. Acad. Sci. Hung.*, 18, 45 (1959)

113. A. M. Gavrish, E. I. Zoz, T. A. Ansimova, N. V. Pitak and L. I. Karyakin, *Izv. Akad. Nauk SSSR, Neorg. Mater.*, 8, 1175 (1972)

114. N. W. Grimes, *Phil. Mag.*, 25, 67 (1972)

115. F. S. Stone and R. J. D. Tilley in "Reactivity of Solids", Vol. 7, p. 262, M. W. Roberts and F. S. Stone, Editors, Chapman and Hall, London (1972)

116. M. T. Shim and W. J. Moore, *J. Chem. Phys.*, 26, 802 (1957)

117. P. Lacombe, *Science of Ceramics*, 5, 111 (1970)

118. R. Fricke and G. Weitbrecht, *Z. Elektochem.*, 48, 87 (1942)

119. B. G. Lebedev, *Izv. Akad. SSSR, Otd. Tekhn. Nauk, Met. i Toplivo*, 6, 7 (1962)

120. I. A. Novokhatskii and L. M. Lenev, *Izv. Akad. Nauk SSSR, Met. i Gorn. Delo*, 6, 47 (1963)

121. T. N. Rezukhina, V. A. Levitskii and P. Ozhegov, *Zh. Fiz. Khimii*, 37, 687 (1963)

122. L. M. Lenev and I. A. Novokhatskii, *Russ. J. Inorg. Chem.*, 10, 1307 (1965)

123. I. A. Novokhatskii and L. M. Lenev, *Izv. Vysshikh. Uchebn. Zavedenii, Tsvetn. Met.*, 8, 68 (1965)

124. L. M. Lenev and I. A. Novokhatskii, *Izv. Akad. Nauk SSSR, Metally*, 3, 73 (1966)

125. H. Schmalzried, *Z. Physik. Chem.*, 25, 178 (1960)

126. J. D. Tretjakow and H. Schmalzried, *Ber. Bunsenges. Physik. Chem.*, 69, 396 (1965)

127. T. N. Rezukhina, V. A. Levitskii and P. Ozhegov, *Russ. J. Phys. Chem.*, 37, 358 (1963)

128. V. A. Levitskii and T. N. Rezukhina, *Izv. Akad. Nauk Neorg. Materialy*, 2, 145 (1966)

129. V. A. Levitskii, T. N. Rezukhina and V. G. Dneprova, *Sov. Electrochem.*, 1, 833 (1965)

130. K. K. Kelley, *U. S. Bur. Mines Bull. No. 477*, (1950)

131. K. K. Kelley, *U. S. Bur. Mines Bull. No. 476*, (1949)

132. K. K. Kelley, *U. S. Bur. Mines R. I. No. 5059*, (1954)

133. O. Kubaschewski, E. L. Evans and C. B. Alcock, "Metallurgical Thermochemistry", Pergamon Press, London (1967)

134. A. Navrotsky and O. J. Kleppa, *J. Inorg. Nucl. Chem.*, 30, 479 (1968)

135. K. T. Jacob and C. B. Alcock, *J. Am. Ceram. Soc.*, 58, 192 (1975)

136. K. T. Jacob, Private Communication

137. E. Aukrust and A. Muan, *J. Am. Ceram. Soc.*, 46, 358 (1963)

138. O. Kubaschewski, *National Physical Laboratory DCS Report No. 7* (1970)

139. W. J. Jander and W. Stamm, *Z. Anorg. Allgem. Chem.*, 199, 165 (1931)

140. D. J. M. Bevan , J. P. Shelton and J. S. Anderson, *J. Chem. Soc., London*, 1729 (1948)

141. T. E. Bradburn and G. R. Rigby, *Trans. Brit. Ceram. Soc.*, 52, 417 (1953)

142. I. V. Nicolescu, A. Popescu, A. Ionescu and L. Barbat, *Revue Rom. Chem.*, 11, 357 (1966)

143. Yu. A. Tkach and V. G. Samoilenko, *Ukrain. Khimi. Zh.*, 36, 965 (1970)

144. B. Snider, University of Alberta (1978), Unpublished Results

145. J. A. Coath and D. F. Dailly, *Proc. Brit. Ceram. Soc.*, 23, 42 (1972)

146. R. A. Weeks and E. Sonder, *J. Am. Ceram. Soc.*, 63, 92 (1980)

147. R. Chaplin, P. R. Chapman and R. H. Griffin, *Nature*, 172, 77 (1953)

148. P. B. Weisz, C. D. Prater and K. D. Rittenhouse, *J. Chem. Phys.*, 21, 2236 (1953)

149. H. Schmalzried, *Ber. Bunsenges. Physik. Chem.*, 67, 93 (1963)

150. A. R. Hippel, "Dielectrics and Waves", John Wiley and Sons, New York (1954)

151. H. Schmalzried, *Z. Elektrochem.*, 66, 572 (1962)

152. F. A. Kroger, "The Chemistry of Imperfect Crystal", North Holland, Amsterdam (1974)

153. P. Kofstad, "Nonstoichiometry, Diffusion and Electrical Conductivity in Binary Metal Oxides", Wiley-Interscience, New York (1972)

154. R. J. Brooks in "Electrical Conductivity in Ceramics and Glass", p. 179, N. M. Tallan, Editor, Marcel Dekker, New York (1974)

155. T. H. Etsell and S. N. Flengas, *Chem. Rev.*, 70, 339 (1970)

156. W. L. Worrell, *J. Am. Ceram. Soc.*, 53, 425 (1974)

157. J. H. Kennedy in "Topics in Applied Physics (Solid Electrolytes)", Vol. 21, p. 105, S. Geller, Editor, Springer-Verlag, Berlin (1977)

158. R. A. Rapp and D. A. Shores in "Physico-Chemical Measurements in Metals Research Part 2", p. 123, R. A. Rapp, Editor, Interscience, New York (1970)

159. M. H. Hebb, *J. Chem. Phys.*, **20**, 185 (1952)

160. C. Wagner, *Z. Elektrochem.*, **60**, 4 (1956)

161. C. Wagner, *Z. Elektrochem.*, **63**, 1027 (1959)

162. C. Wagner in "Proc. Intern. Comm. Electrochem. Therm. Kinetics (CITCE), 7th Meeting, Lindau", Buttersworth Scientific Publ., London (1955)

163. B. Ilschner, *J. Chem. Phys.*, **28**, 1109 (1958)

164. D. O. Raleigh, *J. Phys. Chem. Solids*, **26**, 329 (1965)

165. J. B. Wagner and C. Wagner, *J. Chem. Phys.*, **26**, 1597 (1957)

166. J. B. Wagner and C. Wagner, *J. Electrochem. Soc.*, **104**, 509 (1957)

167. A. Morkel and H. Schmalzried, *J. Chem. Phys.*, **36**, 3101 (1962)

168. J. W. Patterson, E. C. Bogren and R. A. Rapp, *J. Electrochem. Soc.*, **114**, 752 (1967)

169. D. O. Raleigh in "Progress in Solid State Chemistry", Vol. 3, p. 83, Pergamon Press, Oxford (1967)

170. L. Heyne in "Mass Transport in Oxides", p. 149, J. B. Watchman and A. O. Franklin, Editors, NBS Spec. Publ. 296 (1968)

171. C. Wagner in "Advances in Electrochemistry and Electrochemical Engineering", Vol. 4, p. 1, Interscience, New York (1966)

172. H. S. Rossotti , "Chemical Applications of Potentiometry", Van Nostrand, London (1969)

173. W. A. Fischer and A. Hoffmann, *Arch. Eisenhuttenw.*, 26, 43 (1955)

174. N. M. Greenwood, "Ionic Crystals, Lattice Defects and Nonstoichiometry", Butterworths, London (1970)

175. "Crystal Data - Determinative Tables", Vol. 2, J. D. H. Donway and H. M. Ondik, Editors, National Bureau of Standards, 3rd Edition (1973)

176. B. Phillips, J. J. Hutta and I. Warshaw, *J. Am. Ceram. Soc.*, 46, 579 (1963)

177. T. H. Etsell and S. N. Flengas, *Met. Trans.*, 3, 27 (1972)

178. G. G. Charette and S. N. Flengas, *J. Electrochem. Soc.*, 115, 796 (1968)

179. S. P. Mitoff, *J. Chem. Phys.*, 35, 882 (1961)

180. H. G. Sockel and H. Schmalzried, *Ber. Bunsenges. Physik. Chem.*, 72, 745 (1968)

181. Y. P. Tretyakov and R. A. Rapp, *Trans. AIME*, 245, 1235 (1969)

182. W. C. Tripp and N. M. Tallan, *J. Am. Ceram. Soc.*, 53, 531 (1970)

183. G. Zintl, *Z. Physik. Chem. (N. F.)*, 48, 340 (1966)

184. G. I. Finch and K. P. Sinha, *Proc. R. Soc., London*, 239, 145 (1957)

185. W. J. Lackey in "Materials Science Research", Vol. 5, p. 489, W. W. Kriegel and H. Palmour, Editors, Plenum Press, New York (1971)

186. H. P. R. Frederikse and W. R. Hosler in "Materials Science Research", Vol. 9, p. 233, A. R. Cooper and A. H. Heuer, Editors, Plenum Press, New York (1975)

187. T. Matsumura, *Can. J. Phys.*, **44**, 1685 (1968)

188. J. A. Champion, *Proc. Brit. Ceram. Soc.*, **10**, 51 (1968)

189. S. Dasgupta and J. Hart, *J. Appl. Phys.*, **16**, 725 (1965)

190. K. Kitazawa and R. L. Coble, *J. Am. Ceram.Soc.*, **57**, 245 (1974)

191. R. J. Brook, J. Yee and F. A. Kroger, *J. Am. Ceram. Soc.*, **54**, 444 (1971)

192. H. H. von Baumbach and C. Wagner, *Z. Physik. Chem. (Leipzig)*, **B24**, 59 (1934)

193. R. Uno, *J. Phys. Soc.,Japan*, **22**, 1502 (1967)

194. M. Verwey, M. Haaijman, F. Romeijn and M. Van Ousterkont, *Philips Res. Rep.*, **5**, 173 (1950)

195. R. R. Heikes and W. D. Johnston, *J. Chem. Phys.*, **26**, 582 (1957)

196. I. Bransky and N. M. Tallan, *J. Chem. Phys.*, **49**, 1243 (1968)

197. S. Pizzini and R. Morlotti, *J. Electrochem. Soc.*, **114**, 1179 (1967)

198. G. H. Meier and R. A. Rapp, *Z. Physik. Chem. (N. F.)*, **74**, 168 (1971)

199. R. D. Shannon and C. T. Drewitt, *Acta Cryst.*, **B25**, 925 (1969)

200. C. M. Osburn and R. W. Vest, *J. Phys. Chem. Solids*, **32**, 1331 (1971)

201. S. Pizzini and G. Bianchi, *La Chimica e L'Industria*, **54**, 224 (1972)

202. M. L. Volpe and J. Reddy, *J. Chem. Phys.*, **53**, 1117 (1970)

203. F. A. Cotton and G. Wilkinson, "Advanced Inorganic Chemistry", Interscience, New York, 3rd Edition (1972)

204. R. E. Carter and F. D. Richardson, *Trans. AIME*, **200**, 1244 (1954)

205. B. Fisher and D. S. Tannhauser, *J. Chem. Phys.*, **44**, 1663 (1966)

206. N. G. Eror and J. B. Wagner, Jr., *J. Phys. Chem. Solids*, **29**, 1597 (1968)

207. C. Greskovich and H. Schmalzried, *J. Phys. Chem. Solids*, **31**, 639 (1970)

208. C. E. Birchenall in "Mass Transport In Oxides", J. B. Watchman and A. D. Franklin, Editors, National Bureau of Standards Special Publication 296, Washington, D.C. (1968)

209. J. Dixon, L. LaGrange, U. Merten, C. Miller and J. Porter, *J. Electrochem. Soc.*, **110**, 276 (1963)

210. A. Kumar, D. Rajdev and D. L. Douglas, *J. Am. Ceram. Soc.*, **55**, 439 (1972)

211. N. M. Tallan and R. W. Vest, *J. Am. Ceram. Soc.*, **49**, 401 (1966)

212. N. S. Choudhury and J. W. Patterson, *J. Am. Ceram. Soc.*, 57, 90 (1974)

213. D. W. Peters, L. F. Feinstein and C. Peltzer, *J. Chem. Phys.*, 42, 2345 (1964)

214. J. P. Loup and A. M. Anthony, *Rev. Hautes Temp. Refract.*, 1, 15 (1964)

215. R. N. Blumenthal and M. A. Seitz in "Electrical Conductivity in Ceramics and Glass", Part A, p. 35, N. M. Tallan, Editor, Marcel Dekker, New York (1974)

216. A. J. Moulson and P. Popper, *Proc. Brit. Ceram. Soc.*, 10, 41 (1968)

217. O. T. Ozkan and A. J. Moulson, *Brit. J. Appl. Phys.*, 3, 983 (1970)

218. B. V. Dutt, J. P. Hurrell and F. A. Kroger, *J. Am. Ceram. Soc.*, 58, 420 (1975)

219. B. V. Dutt and F. A. Kroger, *J. Am. Ceram. Soc.*, 58, 474 (1975)

220. M. W. Davies and F. D. Richardson, *Trans. Farad. Soc.*, 55, 604 (1959)

221. A. Z. Hed and D. S. Tannhauser, *J. Electrochem. Soc.*, 114, 314 (1967)

222. A. Z. Hed and D. S. Tannhauser, *J. Chem. Phys.*, 47, 2090 (1967)

223. M. O. O'Keeffe and M. Valigi, *J. Phys. Chem. Solids*, 31, 947 (1970)

224. J. B. Price and J. B. Wagner, Jr., *J. Electrochem. Soc.*, 117, 242 (1970)

225. C. Greskovich and V. S. Stubican, *J. Phys. Chem.*

Solids, **30**, 909 (1969)

226. W. P. Whitney and V. S. Stubican, *J. Am. Ceram. Soc.*, **54**, 349 (1971)

227. W. P. Whitney and V. S. Stubican, *J. Phys. Chem. Solids*, **32**, 305 (1971)

228. D. W. Strickler and W. G. Carlson, *J. Am. Ceram. Soc.*, **47**, 112 (1964)

229. B. C. H. Steele and C. B. Alcock, *Trans. AIME*, **233**, 1359 (1965)